DOT/FAA/AR-99/19

Office of Aviation Research
Washington, D.C. 20591

Engine Debris Penetration Testing

November 1999

Final Report

This document is available to the U.S. public through the National Technical Information Service (NTIS), Springfield, Virginia 22161.

U.S. Department of Transportation
Federal Aviation Administration

NOTICE

This document is disseminated under the sponsorship of the U.S. Department of Transportation in the interest of information exchange. The United States Government assumes no liability for the contents or use thereof. The United States Government does not endorse products or manufacturers. Trade or manufacturer's names appear herein solely because they are considered essential to the objective of this report. This document does not constitute FAA certification policy. Consult your local FAA aircraft certification office as to its use.

This report is available at the Federal Aviation Administration William J. Hughes Technical Center's Full-Text Technical Reports page: www.tc.faa.gov/its/act141/reportpage.html in Adobe Acrobat portable document format (PDF).

Technical Report Documentation Page

1. Report No.	2. Government Accession No.	3. Recipient's Catalog No.
DOT/FAA/AR-99/19		

4. Title and Subtitle	5. Report Date
ENGINE DEBRIS PENETRATION TESTING	November 1999
	6. Performing Organization Code
7. Author(s)	8. Performing Organization Report No.
Joseph Manchor and Charles Frankenberger	
9. Performing Organization Name and Address	10. Work Unit No. (TRAIS)
Naval Air Warfare Center, Weapons Division Code 418300D, Bldg. 91073 China Lake, CA 93555-6001	11. Contract or Grant No. DTFA03-95-X-90019
12. Sponsoring Agency Name and Address	13. Type of Report and Period Covered
U.S. Department of Transportation Federal Aviation Administration Office of Aviation Research Washington, DC 20591	Final Report
	14. Sponsoring Agency Code ANM-100, ANE-100

15. Supplementary Notes

The Federal Aviation Administration William J. Hughes Technical Center contracting representative was William Emmerling.

16. Abstract

The damaging effects from an uncontained aircraft turbine engine failure can be catastrophic. As a result, the Federal Aviation Administration has commissioned a program to mitigate the damaging effects of such an event. The Uncontained Engine Failure Mitigation Program will involve both industry and government to determine possible engineering solutions to this problem.

As part of this program, the Naval Air Warfare Center Weapons Division (NAWCWPNS) has been tasked to evaluate ballistic damage analysis tools and techniques which are currently in use by the defense community. The intent is to determine their applicability in predicting the damaging effects from an uncontained engine failure. This report documents testing which was conducted in the evaluation of penetration equations under the circumstances present during engine failure events.

17. Key Words	18. Distribution Statement
Engine debris, Penetration, Uncontainment, Fan debris, Air gun	This document is available to the public through the National Technical Information Service (NTIS), Springfield, Virginia 22161.

19. Security Classif. (of this report)	20. Security Classif. (of this page)	21. No. of Pages	22. Price
Unclassified	Unclassified	167	

Form DOT F1700.7 (8-72) Reproduction of completed page authorized

TABLE OF CONTENTS

		Page
EXECUTIVE SUMMARY		vii
1.	INTRODUCTION	1
1.1	Background and Overview	1
1.2	The JTCG/ME Penetration Equations	1
2.	TEST OBJECTIVES	2
3.	APPROACH	2
3.1	Test Overview	2
3.2	Test Sequence	4
3.2.1	Test Series #1	4
3.2.2	Test Series #2	6
3.2.3	Test Series #3 Through 7	7
3.2.4	Test Series #8	7
3.2.5	Test Series #9	7
4.	DATA ANALYSIS	7
4.1	Velocity Calculation	7
4.2	Orientation	8
4.2.1	Presented Area	8
4.2.2	Pitch, Yaw, and Roll	10
5.	RESULTS	12
5.1	Data Presentation	12
5.1.1	Data Tabulation	12
5.1.2	Velocity Comparisons	13
5.1.3	Prediction Accuracy	13
5.1.4	Median Comparison	13
5.2	Limitations of the Penetration Equations	14
5.2.1	Ballistic Perforation Mode	14
5.2.2	Petaling	15
5.2.3	Plugging	15

5.2.4 Ballistic Perforation Mode and Fragment Orientation 17
5.2.5 Comparison of Perforation Mode to Penetration Efficiency 18
5.2.6 Perforation Mode and Prediction Accuracy 18
5.2.7 Perimeter of Shear 19
5.2.8 Presented Area Accuracy 22
5.2.9 Target Material and Structural Characteristics 24
5.2.10 Rotational Versus Linear Kinetic Energy 27

5.3 Discussion of Results 29

5.3.1 Prediction Accuracy (All Test Series) 29
5.3.2 Prediction Accuracy by Fragment Type 30
5.3.3 Prediction Accuracy by Prediction Model 31

6. SUMMARY 32

7. CONCLUSIONS AND RECOMMENDATIONS 33

8. REFERENCES 34

APPENDICES

A—Derivation of the JTCG/ME Penetration Equations
B—Compilation of Test Results
C—Target Impact Photographs
D—Detailed Test Plan

LIST OF FIGURES

Figure		Page
1	Test Site Setup With MIKES Gun	3
2	Rubber Sabot	3
3	Sabot Catcher	4
4	Test Series Fragment Comparison	5
5	Calculation of Fragment Presented Area	9
6	Three-Dimensional Fragment and Orientation Unit Vectors	11
7	Pitch, Yaw, and Roll	11
8	Example Pointed and Blunt Penetrators	14
9	Observed Perforation Modes	15
10	Petaling (Single Sided)	16
11	Petaling (Multisided)	16
12	Plugging	17
13	Plugging and Petaling	17
14	Fragment Orientation Angle	17
15	Perimeter Comparison	20
16	Perimeter Ratio (Rectangle and Square of Equivalent Presented Area)	21
17	Prediction Accuracy Versus Area Ratio	21
18	Test Series 2, Residual Velocity Curves Orientation Comparison	22
19	Test Series 5 and 7, Residual Velocity Curves Orientation Comparison	23
20	Effects of Presented Area Inaccuracies	23
21	Cowling Exterior	25
22	Cowling Interior	25
23	Test Series 8 Prediction Comparison	25
24	Test Series 8 Predictions (Skin Impacts Only)	26
25	Plugging Failure, Shot 60 Front (a) and Back (b)	26
26	Plugging Failure, Shot 67 Front (a) and Back (b)	27
27	Test Series 5 and 7, Kinetic Energy Graphical Comparison	29
28	Prediction Accuracy Distribution	29
29	Prediction Accuracy by Fragment Type	30
30	Prediction Accuracy by Prediction Model	31

LIST OF TABLES

Table		Page
1	Test Series 5 and 7, Kinetic Energy Tabular Comparison	28
2	Prediction Accuracy by Prediction Model	32

EXECUTIVE SUMMARY

The damaging effects from an uncontained aircraft turbine engine failure can be catastrophic. As a result, the Federal Aviation Administration (FAA) has commissioned a program to mitigate the damaging effects of such an event. The Uncontained Engine Debris Mitigation Program will involve both industry and government to determine possible engineering solutions to this problem.

As part of this program, the Naval Air Warfare Center Weapons Division (NAWCWPNS) has been tasked to evaluate ballistic damage analysis tools and techniques that are currently in use by the defense community. The intent is to determine their applicability in predicting the damaging effects from an uncontained engine failure. This report documents testing that was conducted and the evaluation of several empirical penetration equations under the circumstances present during engine failure events.

The data generated under this effort showed that variations in the velocity, orientation, and shape of the debris results in differing failure modes of the targets. When plugging failures of the targets occur, the results of the defense equations are quite good. When petaling failures occur the prediction accuracy was degraded. This resulted in the development of an FAA Energy Equation through numerical curvefitting of the test data for 2024 T3 aluminum targets.

Additional testing is planned to evaluate the penetration equations performance with real aircraft structure and varying obliquity angles at impact under phase II testing.

1. INTRODUCTION.

1.1 BACKGROUND AND OVERVIEW.

An uncontained engine failure precipitated the loss of control of a DC-10 at cruise altitude over the Midwestern United States in 1989. The aircraft crashed while attempting to land at Sioux City Airport. The accident investigation revealed that multiple fragments from the engine failure damaged all of the redundant flight control systems resulting in a loss of the hydraulic systems. The aircrew maintained a modicum of control by varying the power level on the remaining wing mounted engines saving many lives.

The National Transportation Safety Board (NTSB) produced several recommendations as a result of that accident and this effort continues to support the Federal Aviation Administration's (FAA) response to those recommendations which are intended to develop revised certification requirements to minimize potential for catastrophic failures from multiple fragments during an uncontained engine failure. This effort is being performed under the advice of the Aviation Rulemaking Advisory Committee for Power Plant Installation and Harmonization Working Group with industry and government to develop analytical methods to evaluate the problem and mitigate the consequences.

As part of this program, the Naval Air Warfare Center Weapons Division (NAWCWPNS) has been tasked to evaluate ballistic damage analysis tools and techniques which are currently in use by the defense community. The intent is to determine their applicability in predicting the damaging effects from an uncontained engine failure. This report documents testing which was conducted in the evaluation of these equations

1.2 THE JTCG/ME PENETRATION EQUATIONS.

Among the analysis tools currently in use are the Joint Technical Coordinating Group for Munitions Effectiveness (JTCG/ME) penetration equations [1]. These equations were originally developed to predict the penetration and residual velocity of ballistic weapon projectiles upon impact with various materials. Of particular interest are the ballistic prediction equations which were developed for warhead fragments, as these fragments are closest in geometric description to jet engine blade fragments. The JTCG/ME penetration equations are listed as follows. Derivation of these equations is covered in appendix A.

$$V_r = \frac{\sqrt{V^2 - V_{50}^2}}{1.0 + \frac{\rho A_p t}{W \cos\theta}} \qquad \text{The Residual Velocity Equation} \qquad (1)$$

$$V_{50} = C_{bf}\left(\frac{\rho f t A_p}{W}\right)^{bf} \sec^h\theta \left(\frac{\rho f t A_p}{W_o}\right)^f \qquad \text{The Ballistic Limit Equation} \qquad (2)$$

Variables: V = debris initial velocity
V_{50} = debris ballistic limit velocity (Penetration occurs 50% of the time.)
V_r = debris residual velocity
ρ_f = debris specific weight (debris weight/volume)
ρ = plate specific weight (plate weight/volume)
t = plate thickness
A_p = debris presented area along direction of travel
θ = debris obliquity angle at impact
W = debris weight
W_o = 100 grains

Empirical Constants: C_{bf}, b_f, h, f

The penetration equations have been incorporated into a computer model as one possible analysis tool for aircraft designers. The Uncontained Debris Model (UDM) focuses on blade fragment debris as this type of debris is most likely to result from an uncontained engine event. According to extensive investigation, including the development of an extensive uncontained failure database, these are the most likely particles which would result in multiple damage sites to an aircraft. The debris model identifies the debris type by component (fan blade, turbine blade, compressor blade) and defines the most likely size, mass, and velocity for each debris fragment.

2. TEST OBJECTIVES.

The objective of these tests was to collect fragment penetration data to validate and/or refine the penetration equations used to develop the Uncontained Debris Model. Testing was conducted using simulated and actual engine debris fragments against various thicknesses of aluminum plates and aircraft skin structures.

3. APPROACH.

3.1 TEST OVERVIEW.

The data required for validation of the model would be penetration data resulting from the impact of engine blade fragments against representative aircraft fuselage material. This data would include the impact and residual velocities of the fragments, along with the impact orientation of each fragment with respect to the target.

To achieve the collection of this data, it would be necessary to propel representative engine blade fragments at velocities representative of an uncontained engine event (approximately 200-800 ft/s). It was decided to utilize the Missile Impact Kinetic Energy Simulator (MIKES) airgun to propel the engine blade fragments.

The MIKES gun is a recent addition to the NAWCWPNS Weapons Survivability Laboratory (WSL). Although originally developed as a means to propel man portable missiles, its large barrel diameter (6.07") would be capable of accommodating the larger representative fan blade

fragments. Figure 1 illustrates the test site setup. Specifics of this setup are outlined in the detailed test plan included in appendix D.

FIGURE 1. TEST SITE SETUP WITH MIKES GUN

The fragments were propelled from the gun by means of a sabot. At the end of the gun barrel, a sabot stopper was placed to stop the sabot but allow the fragment to continue travel unimpeded. The original design as outlined in the test plan for the sabot and sabot stopper proved impractical. The sabot would shatter within the stopper allowing sabot fragments to travel along with the engine fragment.

Alternative designs for the sabot and stopper were developed which utilized a rubber sabot along with an energy absorbing sabot stopper. Details of these designs are illustrated in figures 2 and 3. The new designs were successful in stopping the sabot and allowing unimpeded travel of the engine fragment. The rubber sabot additionally proved durable, allowing its partial reuse for successive shots.

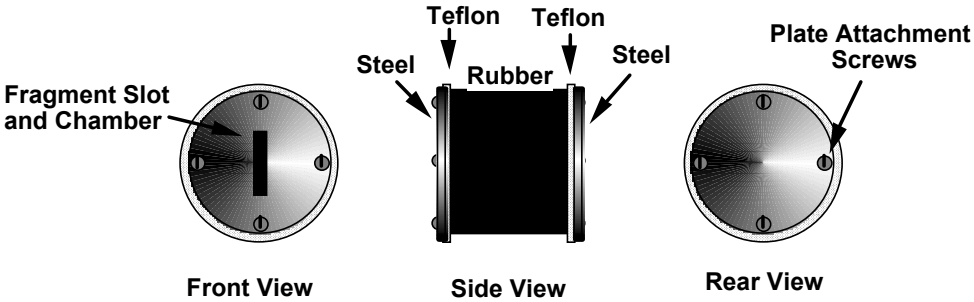

FIGURE 2. RUBBER SABOT

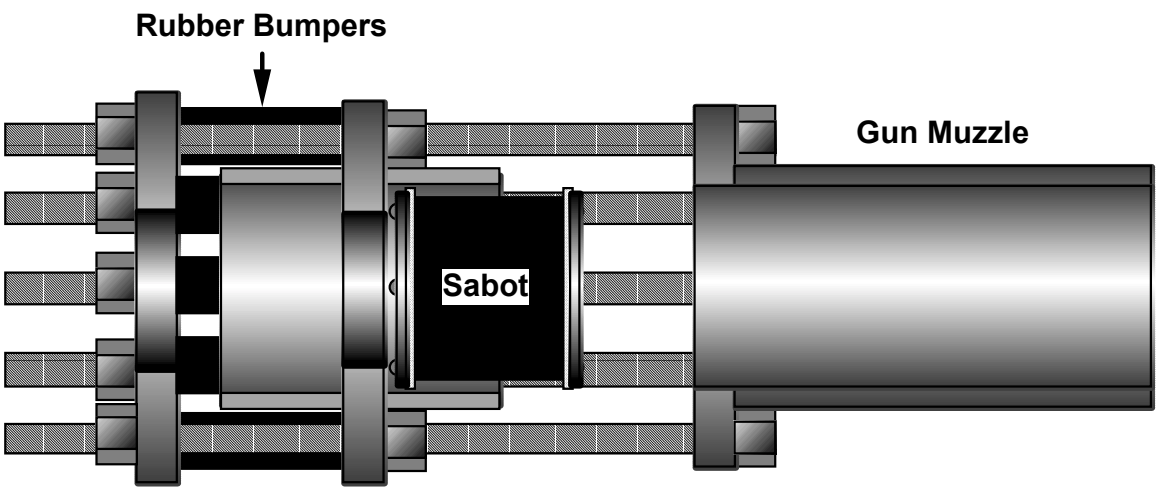

FIGURE 3. SABOT CATCHER

3.2 TEST SEQUENCE.

The test matrix outlined in the test plan called for nine different test series to be conducted. These series propelled various types and sizes of engine blade fragments at current and proposed fuselage materials. A total of eighty-four shots were conducted during this testing. Six of these shots failed to produce data, mainly due to target misses. For those shots which were successful, impact and residual velocities of the fragments were measured through the use of high-speed film and breakpapers. Impact orientation of the fragment was also determined from high-speed film views within two perpendicular planes.

Fragments utilized included engine fan, turbine, and compressor blade fragments. Figure 4 illustrates the various fragments utilized in this testing. An additional fragment was utilized which was similar to that used during the 1997 SRI International Advanced Armor Technology impact experiments [2]. All fragments were solid titanium with the exception of the turbine blade fragments which were composed of steel.

3.2.1 Test Series #1.

This test series verified the effectiveness of the sabots in achieving end on and tumbled impacts with the target. The accuracy of fragment velocity calculations were also verified by comparison of breakpaper computations with high-speed camera visual calculations. Finally, proper operation of all test systems were verified during these tests.

During the conduct of this series, it immediately became apparent that achieving impact orientations as specified for each test series would be difficult. The engine blade fragments tumbled severely soon after leaving the muzzle of the gun. It was determined from high-speed camera footage that this was primarily due to the airfoil shape of these fragments. High-speed travel through the air created a large lift vector which was off-center from the fragment's center of gravity. This moment resulted in the fragment's tumbling.

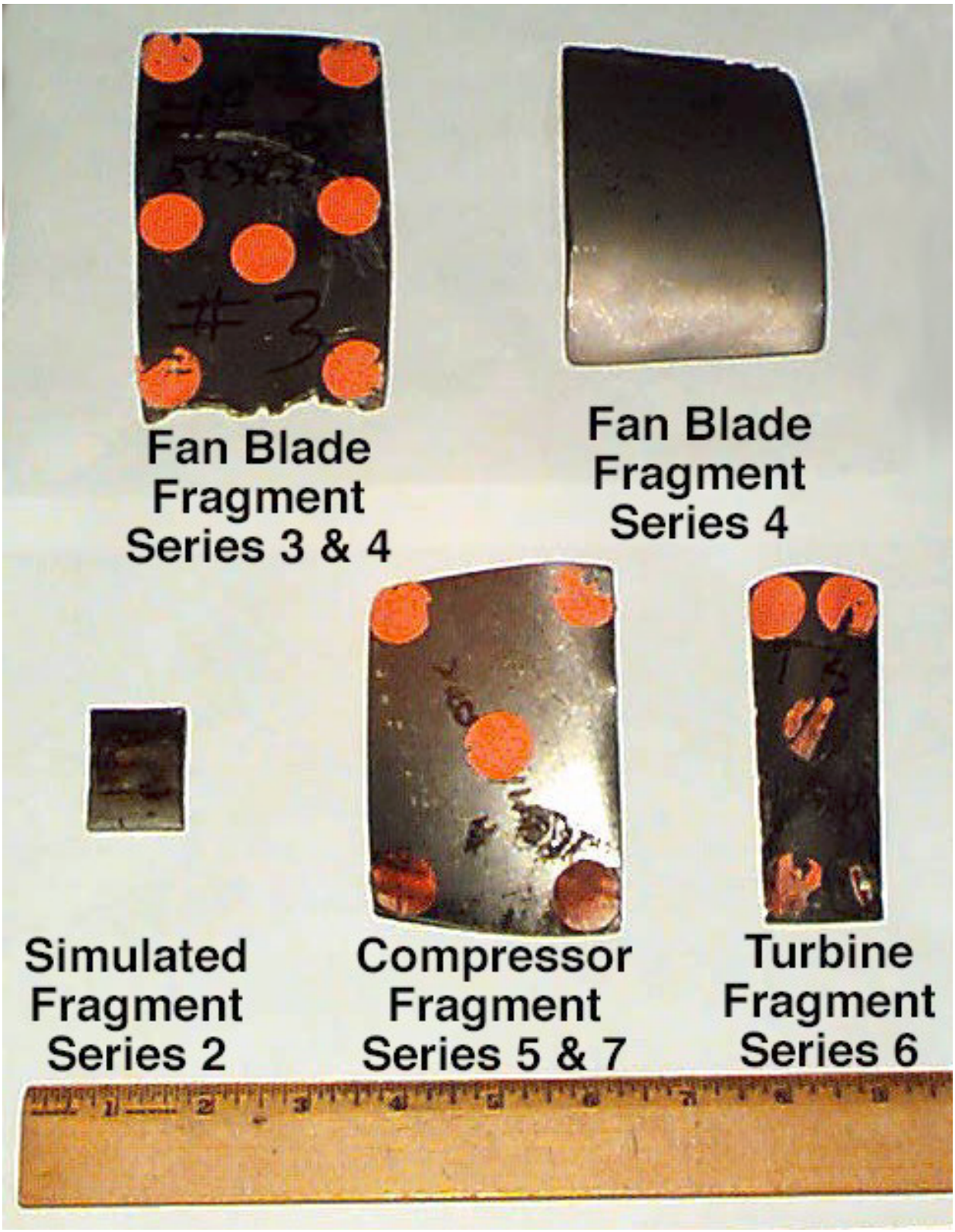

FIGURE 4. TEST SERIES FRAGMENT COMPARISON

As this tumbling would also likely occur during an engine burst event, it was decided to proceed with a change to the test matrix. All fragments would be propelled at an initial end-on orientation within the sabot. Fragment tumbling and the resulting impact orientation would be observed and measured from the high-speed camera footage. Analysis of the penetration equation's prediction effectiveness would be based on each fragment's orientation at the moment of impact.

The series also verified the effectiveness of the velocity measurement methods proposed in the test plan. It was noted that fragment tumble often created a deflection of the fragment along the intended shotline. Penetration of the fragment through the target created additional deflections. As such, the fragments sometimes missed the target breakpaper. This breakpaper was also easily damaged by debris in the gun's air blast prior to fragment penetration. Additionally, the residual velocity breakpapers placed well behind the target were rarely impacted due to postimpact deflection of the fragments. For shots which did achieve proper breakpaper operation, breakpaper velocity calculations were compared with velocity calculations from the high-speed film footage. Both were in close agreement.

Due to the difficulties encountered with use of the breakpapers, it was decided to utilize the target breakpaper as a means to quickly verify that the desired impact velocity range was achieved for each test shot. As a cost saving measure, the residual velocity breakpapers were not utilized for subsequent tests. It was also decided that the main source of velocity data for these tests would be the high-speed camera footage due to its close agreement with the breakpapers.

3.2.2 Test Series #2.

Test series #2 fired simulated blade fragments similar to those utilized during the SRI International Advanced Armor Technology impact experiments. The dimensions of these rectangular titanium fragments were 1.4" length × 1.0" width × 0.25" thickness. Each fragment weighed approximately 25 grams. The impact target was 0.05" 2024-T3 aluminum target plates. This test series provided baseline impact resistance data for 2024-T3 aluminum. The series also allowed comparison with the accumulated data from the SRI experiments. A total of eleven shots were conducted for this test series. However, only five of these tests provided useful data.

Various difficulties were encountered during this test series which degraded the acquisition of data. These included three firings which missed the target at the 10-foot standoff distance prescribed in the test plan. As a result, the target was moved to a new standoff of 5 feet.

One firing was conducted with overexposed high-speed film. Also the small simulated fragment was indiscernible in the high-speed coverage of two additional test firings. This was due to the fragment's speed and orientation with respect to the camera for these firings. As a result, fragment velocities and impact orientation were not accurately determined for these shots. As the model predictions are highly dependent on these values, these three firings did not provide useful data.

3.2.3 Test Series #3 Through 7.

These test series impacted actual engine blade fragments against both 0.05" and 0.07" 2024-T3 aluminum target plates. Characteristics of these fragments (dimensions, material, weight, and impact velocity/orientation) were those which were most likely to be experienced during an engine burst. Test series 3 and 4 utilized representative titanium fan blade fragments against 0.05" and 0.07" thickness 2024 T3 aluminum targets respectively. Test series 5 and 7 examined titanium compressor blade impacts while test series 6 utilized steel turbine blade fragments. Test series 5, 6, and 7 all utilized 0.05" 2024 T3 aluminum as targets for the fragments.

3.2.4 Test Series #8.

This test series examined the reaction of engine fan blade impacts against an actual engine cowling. The cowlings were composed of 0.05" 7075 T6 aluminum. Comparison was made with the data accumulated from the previously conducted tests. This comparison would determine consistency of the data between the use of new sheet metal targets and aged engine cowling material.

3.2.5 Test Series #9.

This final test series was to examine fragment impacts against Kevlar fabric target material. Due to difficulty in acquiring a sufficient quantity of Kevlar material, Zylon material was substituted in its place. A total of twelve test shots were conducted against the Zylon targets using each of the represented fragments. The data from these tests will be included in a separate report from SRI International.

4. DATA ANALYSIS.

To evaluate the prediction accuracy of the JTCG/ME Penetration equations, it would be necessary to accurately determine the velocity of the fragment at impact along with the fragment's postimpact residual velocity. Additionally, the presented area of the fragment at impact would need to be determined as input into the penetration equations. High-speed film camera coverage of each impact was utilized to record this data.

A high-speed film record of each shot was acquired through the use of two high-speed film cameras. These cameras were placed to provide views of the impact in two perpendicular planes. These views included perpendicular side and top views of the target.

4.1 VELOCITY CALCULATION.

Through the use of a film motion analyzer, it is possible to accurately determine the film's frame rate at the moment of impact. The analyzer also has movable crosshairs and provides Cartesian coordinate readouts for the center of the crosshairs. Film frames can be incrementally stepped and viewed.

To determine fragment velocities, the analyzer was utilized to determine the distance traveled by the fragment along with the number of film frames required to traverse this distance. The velocity could then be calculated by the equation:

$$\text{Velocity} = \text{Camera Frame Rate} \times \text{Distance Traveled}/\#\text{ of Frames}$$

The frame rate for the high-speed cameras were preset to 2,000 frames per second for all events. As the film cannot instantaneously accelerate to this frame rate, there was some error between the desired frame rate and the actual film frame rate at the moment of the event. As an aid in determining the actual film frame rate, timing markers are placed on the film by the camera at 1-millisecond intervals. The actual camera frame rate is determined by counting both the number of frames and timing markers near the moment of the event. The frame rate is then calculated by dividing the number of frames by the number of 1-ms timing markers.

The distance traveled by the fragment during the event is determined through the use of the analyzer's crosshairs. It is first necessary to determine a scaling factor which equates the analyzer's crosshair coordinate readout with the actual distances viewed on the film. This is accomplished by equating the readout to visual reference distances viewed on the film. For this purpose, scaled gridboards with one-foot reference stripes were placed beside and below the target.

As most of the fragments tumbled during the test, the crosshairs are placed on a visual estimate of the fragment center of gravity. A Cartesian reading is taken of the fragment a few frames prior to impact. A second reading is taken one frame prior to impact. The traversed distance is then calculated by multiplying the scaling factor by the difference of the first and second reading.

4.2 ORIENTATION.

4.2.1 Presented Area.

The presented area of the fragment to the target is a critical input value to the penetration equations. An accurate determination of this value is necessary to confidently evaluate the predictions provided by the equations. The film motion analyzer was also utilized to determine this value.

The high-speed cameras were placed to provide two views of the fragment in two perpendicular planes. These views included a side view and a top view of the fragment in the vicinity of the target. The film frame utilized in calculating the presented area for each test was the immediate frame just prior to fragment impact.

These two views allowed calculation of the fragment presented area in the third plane of the target. This was accomplished by assuming that the fragment was rectangular in shape. Cartesian coordinates for the four corners of the fragment were read from the film analyzer. These coordinates were then converted into width and length vectors for the fragment. The presented area of the fragment in all three (top, side, and frontal) planes could then be calculated by the cross product of these two vectors.

As the top view had inherent parallax errors due to its close proximity to the target, determination of the length and width vectors utilizing visual scaling factors would have incurred additional errors. Instead, vector angles were used to calculate the width and length vectors as described in figure 5.

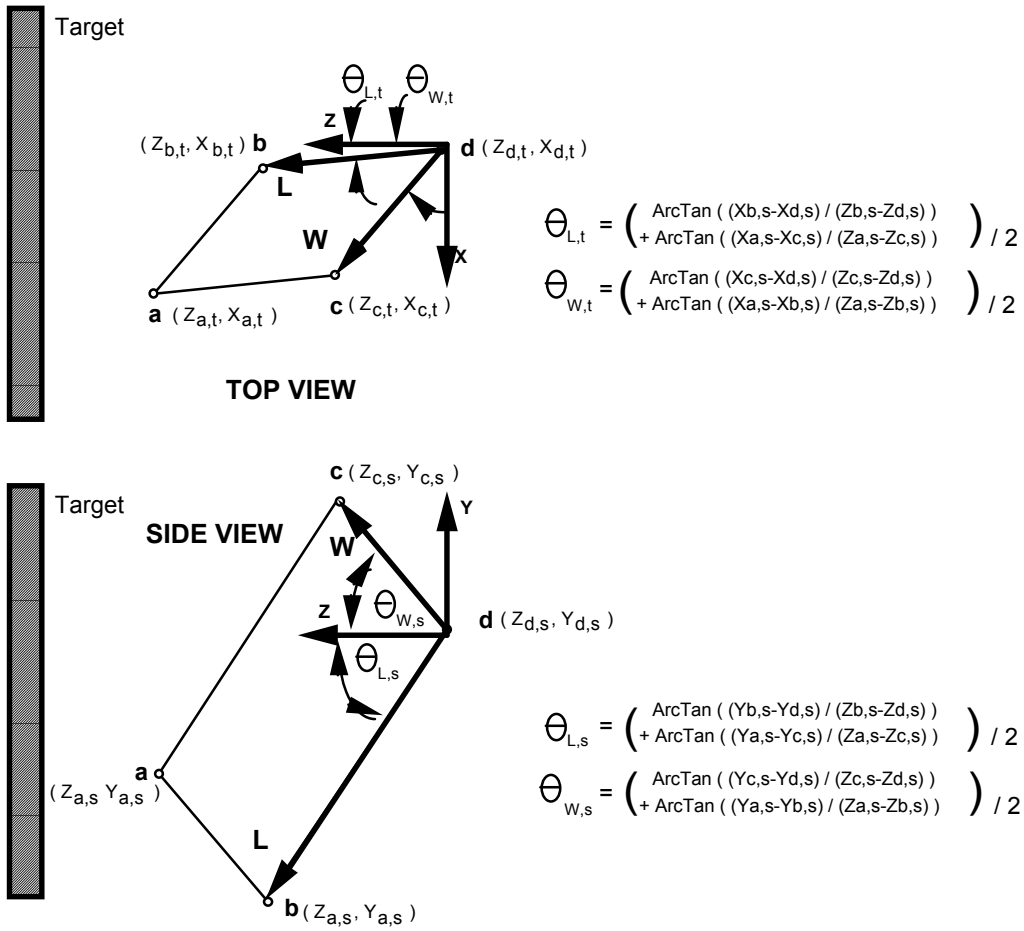

Length Vector: $\mathbf{L} = \text{Length}\ (\sin\ \theta_{L,t}\ \mathbf{i} + \sin\ \theta_{L,s}\ \mathbf{j} + \sin\ \theta_{L,s}\ \mathbf{k})$

Width Vector: $\mathbf{W} = \text{Width}\ (\sin\ \theta_{W,t}\ \mathbf{i} + \sin\ \theta_{W,s}\ \mathbf{j} + \sin\ \theta_{W,s}\ \mathbf{k})$

Area Vector: $\mathbf{A} = \mathbf{L}\ \mathbf{X}$ (Cross) $\mathbf{W}$

Presented Area: $Ap = \mathbf{k}$ component of Area Vector $\mathbf{A}$

or

$Ap = \text{Length}\ X\ \text{Width}\ (\sin\ \theta_{L,t} \sin\ \theta_{W,s} - \sin\ \theta_{L,s} \sin\ \theta_{W,t})$

FIGURE 5. CALCULATION OF FRAGMENT PRESENTED AREA

It should be noted that the calculated value of presented area may be negative, depending on the fragment's orientation at impact. If negative, the absolute value of this term is utilized as input to the penetration equations.

Figure 5 illustrates the calculation of the presented area based on the fragment's side dimensions. The edges of the fragment's perimeter may also contribute to presented area, especially at near edge-on impacts. Calculation of the edge's contributions to presented area is a bit more involved than displayed in figure 5. These areas may be calculated by assuming that the rectangle is of a specified thickness. A thickness vector **T** may be calculated by assuming perpendicularity to the length and width vectors **L** and **W**. As a definition of perpendicularity, the dot product of **L** and **T**, and **W** and **T** will be zero. By applying this assumption with much math (which is not included here), the resulting thickness vector may be calculated by the following relations:

$$\beta = \left(\frac{W_k}{W_i} - \frac{L_k}{L_i}\right) \Big/ \left(\frac{L_j}{L_i} - \frac{W_j}{W_i}\right)$$

$$T_k = \text{thickness} \Big/ \sqrt{1 + \beta^2 + \left(\beta \frac{L_j}{L_i} + \frac{L_k}{L_i}\right)^2}$$

$$T_j = \beta \times T_k$$

$$T_i = -\left(T_j \times L_j + T_k \times L_k\right) \Big/ L_i$$

$$\mathbf{T} = T_i\,\mathbf{i} + T_j\,\mathbf{j} + T_k\,\mathbf{k}$$

Where the above subscripts **i**, **j**, and **k** denote the corresponding components of the specified vector. With the above relations for the components of the thickness vector, the perimeter's contributions to presented area will be the absolute sum of the **k** components of the cross products of **L** and **T** and **W** and **T**.

4.2.2 Pitch, Yaw, and Roll.

A three-dimensional description of the fragment's orientation at impact has been included with the results. Although this description is not needed for the penetration equations, it may expand the utility of this data to other modeling efforts under this program.

A pitch, yaw, and roll orientation description was chosen. This orientation was chosen as it is a standard input parameter for other empirical models which may be of potential use to this program [3]. Figure 6 illustrates a three-dimensional fragment in space prior to experiencing a rotation. The rectangular fragment may be defined in terms of single length, width, and thickness vectors (**L**, **W**, and **T**). To ease description and calculation of the fragment's impact orientation, unit vectors (**Lu** = **L**/Length**, Wu** = **W**/Width**,** and **Tu** = **T**/Thickness) will be used to describe the transformed axes of the length, width, and thickness vectors.

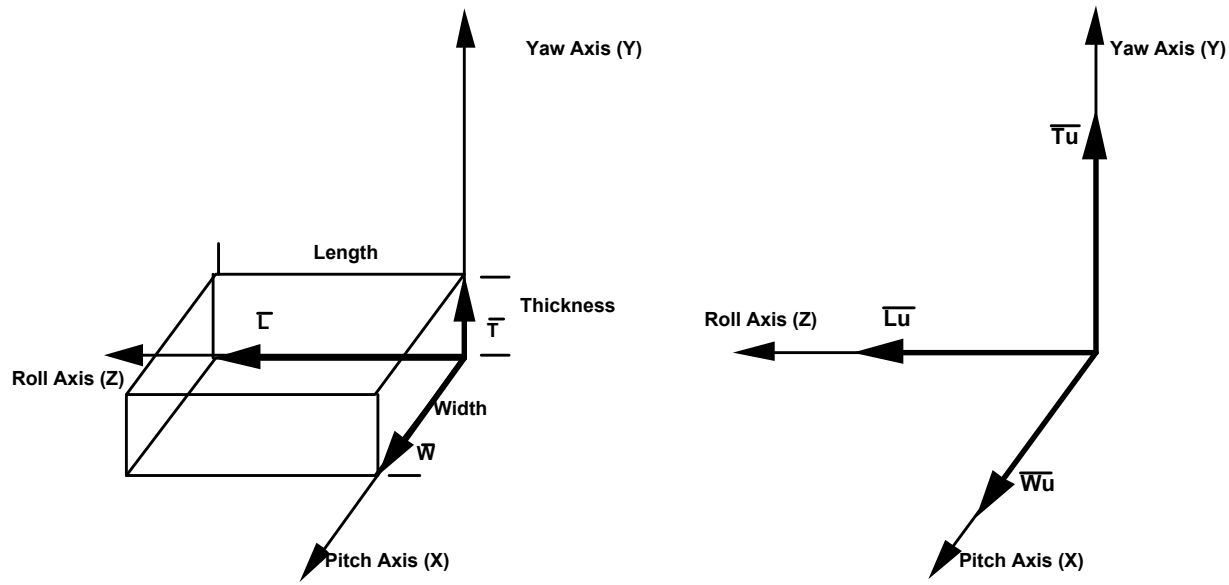

FIGURE 6. THREE-DIMENSIONAL FRAGMENT AND ORIENTATION UNIT VECTORS

The fragment experiences three separate and sequential rotations about each axis as illustrated in figure 7. Upon completion of these rotations, a description of the fragment orientation may be defined by the angular displacement of each of these axis rotations (i.e., pitch, yaw, and roll).

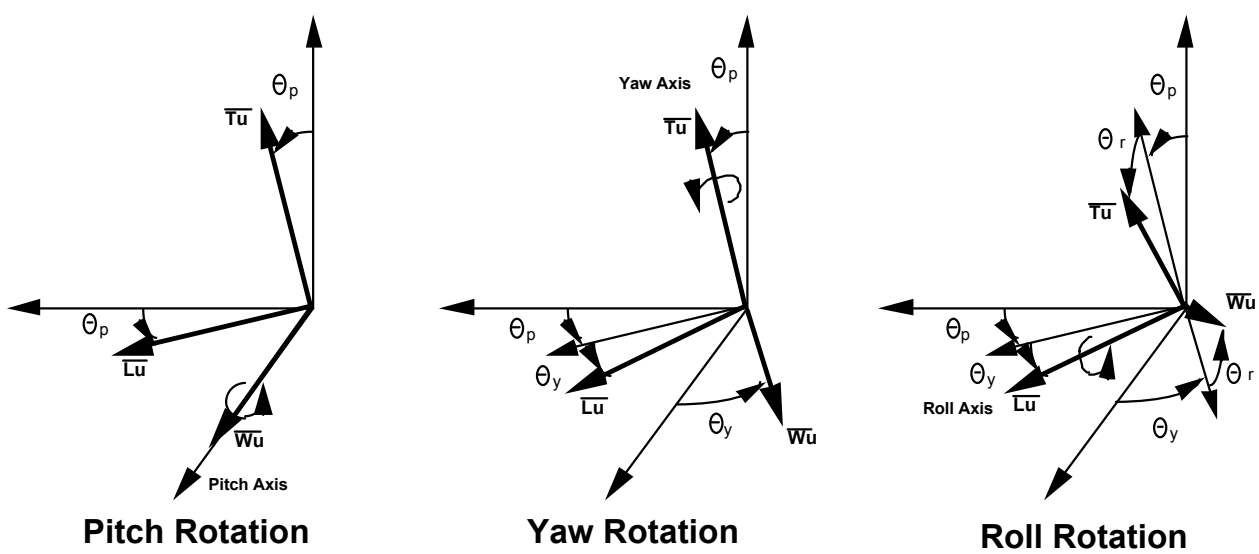

FIGURE 7. PITCH, YAW, AND ROLL

The first rotation experienced is a pitch rotation about the width unit vector axis. As shown in figure 7, the **Wu** axis does not move during this rotation, but the **Lu** and **Tu** axes are translated an equivalent radial pitch distance. It should be noted that all the rotations displayed in figure 7 are positive rotations by the right-hand rule method. For the defined pitch axis, a downward pitch angle is positive.

The second rotation is a yaw rotation about the translated **Tu** axis. The **Lu** and **Wu** axes are rotated an equivalent radial yaw distance while the **Tu** axis does not move. The final rotation is a roll rotation about the twice translated **Lu** axis. The **Lu** axis does not move during this rotation while the **Tu** and **Wu** axes are rotated an equivalent radial roll distance.

It is reemphasized that the three rotations described above must be conducted in the specified sequence (first pitch, then yaw, finally roll). Any other combination of rotations may result in a different final orientation of the axes. The final orientation of the **Wu**, **Tu**, and **Lu** axes to their original orthogonal **i**, **j**, and **k** orientation may be described by the following matrix [3]:

Note: S and C denote sin and cos. Pitch, yaw, and roll are denoted by p, y, and r.

$$\begin{vmatrix} Lu \\ Wu \\ Tu \end{vmatrix} = \begin{vmatrix} Sy & -SpCy & CpCy \\ CyCr & CpSr+SpSyCr & SpSr-CpSyCr \\ -CySr & CpCr-SpSySr & SpCr+CpSySr \end{vmatrix} \begin{vmatrix} i \\ j \\ k \end{vmatrix}$$

Or by expansion of this matrix:

Lu = sin (yaw) **i** -sin (pitch) cos (yaw) **j** + cos (pitch) cos (yaw) **k**

Wu = cos (yaw) cos (roll) **i** + [cos (pitch) sin (roll) + sin (pitch) sin (yaw) cos (roll)] **j** + [sin (pitch) sin (roll) - cos (pitch) sin (yaw) cos (roll)] **k**

Tu = -cos (yaw) sin (roll) **i** + [cos (pitch) cos (roll) - sin (pitch) s (yaw) sin (roll)] **j** + [sin (pitch) cos (roll) + cos (pitch) sin (yaw) sin (roll)] **k**

The above relations provide ample definition of the orientation of a rectangular fragment based on its length, width, and thickness vectors. This orientation is defined through application of three angular translations as denoted by pitch, yaw, and roll.

5. RESULTS.

5.1 DATA PRESENTATION.

The data and results from each test series is presented in appendix B in both tabular and graphic format. These include a tabulation of the test data and predictions along with graphical comparisons of velocity predictions, prediction accuracy, and median comparison.

5.1.1 Data Tabulation.

The data for each test series is presented in tabulated form. Column # 1 of each data table lists the reference shot number. Columns # 2 and 3 lists each fragment's weight and dimensions. Columns # 4 and 5 lists the fragment's impact orientation and presented area. Column # 6 and 8 presents the fragment's impact and residual velocity as measured from the high-speed film. Columns # 7 and 9 present the fragment's residual velocity and ballistic limit velocity as predicted by the penetration equations. These predictions were based upon the target and the

fragment's characteristics and impact conditions. Finally, column # 10 presents the residual velocity prediction accuracy of the penetration equations.

5.1.2 Velocity Comparisons.

For each test series, a direct comparison of the predicted to the actual residual velocities is presented graphically in columnar format. The graphs also include impact velocities for each comparison as an aid in visually interpreting the magnitude of prediction error.

5.1.3 Prediction Accuracy.

A second graph presenting the prediction accuracy of the penetration equations is included for each test series. The relation utilized is as follows:

$$\text{Prediction Accuracy} = 1 - (V_r - V_{r,UDM})/V_I$$

The relation measures the difference between the predicted and actual residual velocity with respect to the fragment's impact velocity. In this manner, the magnitude of the difference between the predicted and actual residual velocities may be kept in perspective to the original impact velocity. An accuracy value close to 1 represents an accurate prediction. Accuracy values greater than 1 represent residual velocity predictions which are greater than the actual residual velocity. Also, accuracy values less than 1 represent residual velocity predictions which are less than the actual residual velocity.

The range of prediction accuracy varies from zero to 2. A prediction accuracy of zero would represent a prediction of nonpenetration while in actuality the residual velocity equals the impact velocity. An accuracy of 2 would represent the opposite extreme, with a predicted residual velocity equal to the impact velocity, while the actual residual velocity equates to zero.

5.1.4 Median Comparison.

Residual velocity vs. impact velocity prediction plots are presented for each test series. The actual residual velocity data points have also been plotted for comparison with the prediction plots. The fragmentation characteristics utilized in the predictions were the average fragment weight and dimensions for each test series.

Each graph includes plots for the possible orientation extremes of the fragment. These include plots for both a completely flat and an edge-on impact. An additional plot is included which represents fragment impacts occurring at the median presented area. The value for this median area was calculated from penetrating fragments only.

The median presented area was chosen as this would allow a means for direct comparison with the data points. As such, 50% of the data points that display residual velocity (i.e., penetrating fragments) would be expected to be above the median prediction line. The other 50% would be expected to be below.

5.2 LIMITATIONS OF THE PENETRATION EQUATIONS.

There are many factors which may account for the limitations in prediction accuracies of the penetration equations. A discussion follows which outlines factors which were of the most significance to the accuracy of the equations. Additional factors covered include those which may intuitively appear to be of significance but through further analysis were eliminated from consideration.

5.2.1 Ballistic Perforation Mode.

The ballistic limit velocity (V_{50}) is an important input variable for the residual velocity equation. An error for this value may result in significant error in the predicted value for residual velocity. The value for V_{50} is calculated through the use of the empirically derived ballistic limit equation.

The ballistic limit equation assumes that the fragment's presented area is the only influential fragment shape factor affecting perforation. It can be easily understood that this may be an inadequate assumption. As an example, consider the two penetrators of figure 8. They both are impacting a target at the same presented area. They are of the same mass and material, but they differ in impact shape. One is pointed while the other is blunt. The ballistic limit equation would predict an equivalent ballistic limit for each impact. However, we would intuitively expect these values to be different.

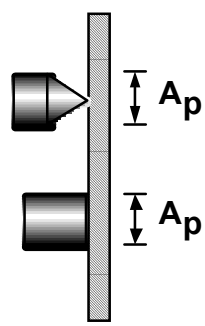

FIGURE 8. EXAMPLE POINTED AND BLUNT PENETRATORS

The data points which were used in Project Thor [4] to develop the empirical constants for the ballistic limit equation were accumulated through the use of compact fragment simulating projectiles (FSP) [5]. The geometry of these FSP were cubes and cylinders with length to diameter ratios close to one [6]. A relatively blunt impact was thus assured regardless of the orientation of the FSP to the target. As such, it may be assumed that plugging was the predominant perforation mode observed during the development of the ballistic limit equation. However, very few of the test shots outlined in this report resulted in a completely sheared plug which separated from the target. Figure 9 outlines the two predominant perforation modes observed during these tests. These were petaling and plugging.

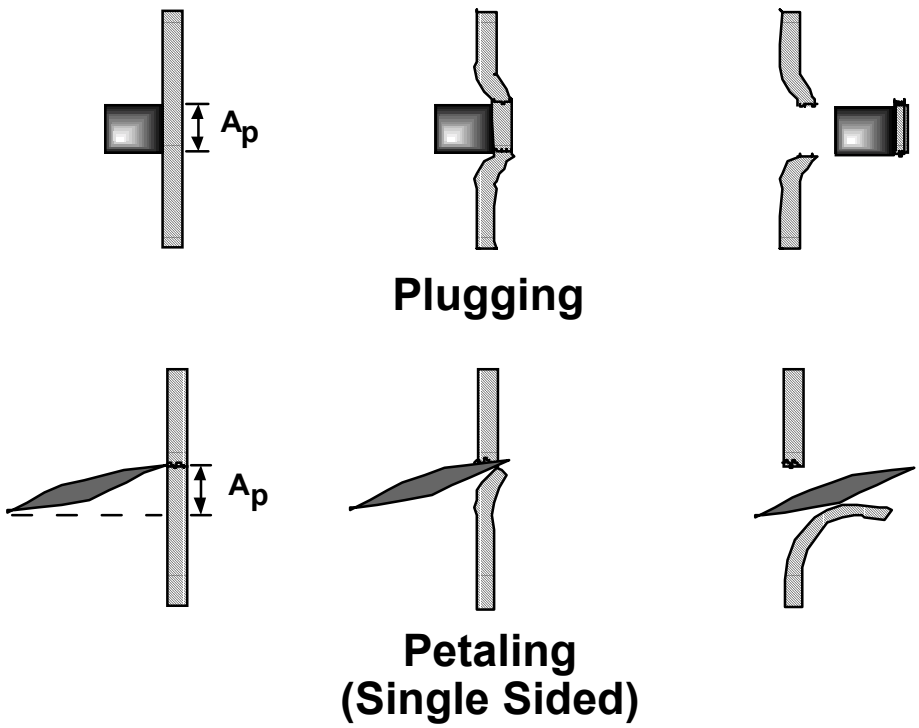

FIGURE 9. OBSERVED PERFORATION MODES

5.2.2 Petaling.

In petaling perforation, a sharp-edged fragment creates an intense shear stress over a small region of the target. This results in an initial breech of the target material near the impact area. This material remains attached to the plate but accelerates outward incurring an initial velocity and thus kinetic energy from the penetrator impact. As the material is pushed outward, it continues its acceleration (and kinetic energy rise) but swings away from the path of the penetrator, allowing relatively easy passage of the fragment. However, postimpact collision with the material can occur and may result in a deflection of the fragment from its original trajectory.

As the plate material remains partially attached to the plate, additional shearing of the target may occur as the material decelerates and dissipates its kinetic energy. Dissipation of the kinetic energy also occurs through deformation, resulting in a curved surface which resembles a flower petal (i.e., petaling). For thin target plate material, the damage to the target from shearing may be similar to that of tearing paper. The resultant perforation hole may be much larger than the original impact presented area. It is important to stress that the majority of these deformations occur after the passage of the fragment. As such, they have little influence on the fragment.

5.2.3 Plugging.

Plugging occurs primarily for blunt edged penetrator impacts. For thin, ductile target materials, the target may bulge or dish out around the perimeter of the penetrator's impact surface. Eventually, shearing stresses become so great along this perimeter that failure of the plate material occurs there. This newly formed "plug" of plate material remains in the path of the

projectile. It is thus accelerated forward, resulting in further deceleration of the fragment. These accelerations are completed when the fragment and plug eventually reach an equivalent residual velocity.

Figures 10 and 11 provide excellent examples of petaling. Both figures are target rear views of impact damage. Figure 10 resulted from the impact of a fan blade fragment. Although the fan blade fragment was relatively large, the resulting hole and "petal" is much larger than the presented area and the actual size of the fragment. Figure 11 resulted from a turbine blade impact and illustrates that more than one petal may form.

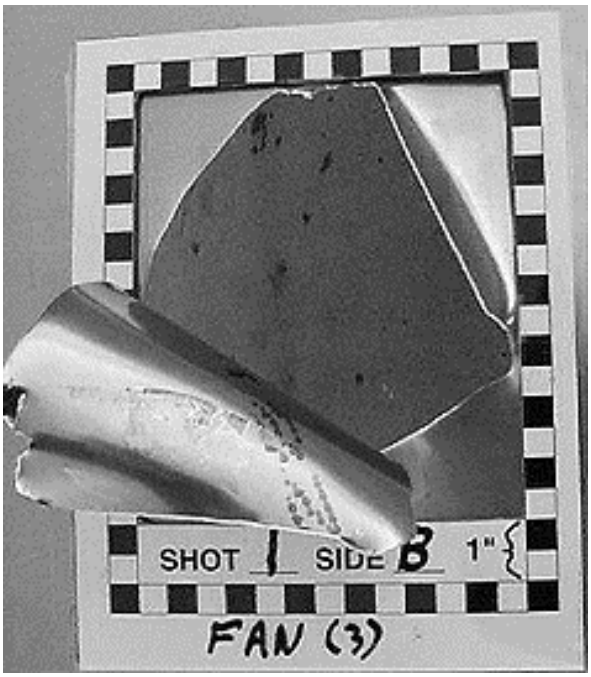

FIGURE 10. PETALING (SINGLE SIDED)

FIGURE 11. PETALING (MULTISIDED)

Figure 12 resulted from impact of a simulated blade fragment from test series 2. A plug of metal has been completely sheared from the target. The area which was sheared is approximately equal to that of the presented area of the fragment. As this fragment impacted relatively flat, the entire outline of the hole is approximately equal to that of the fragment's side. Additionally, note the dishing out of the target surface near the edges of the hole.

Finally, figure 13 has been included to emphasize that a combination of the discussed perforation modes may occur. The figure provides illustration of plugging and petaling. The perforation first started as plugging. Note the dishing out of the plate material, along with the nice outline of the fragment near the top edges of the hole. However, a portion of this plug remained affixed to the target after penetration. As a result, a petal has formed. The imprint of the entire fragment's side can be clearly seen on the edge of this "petal." Additionally, the resulting damage hole is noted as being much larger than that of the fragment's imprint.

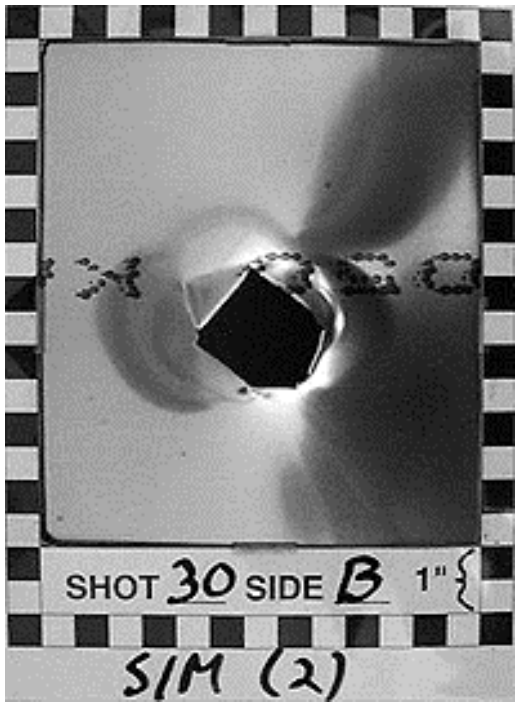

FIGURE 12. PLUGGING

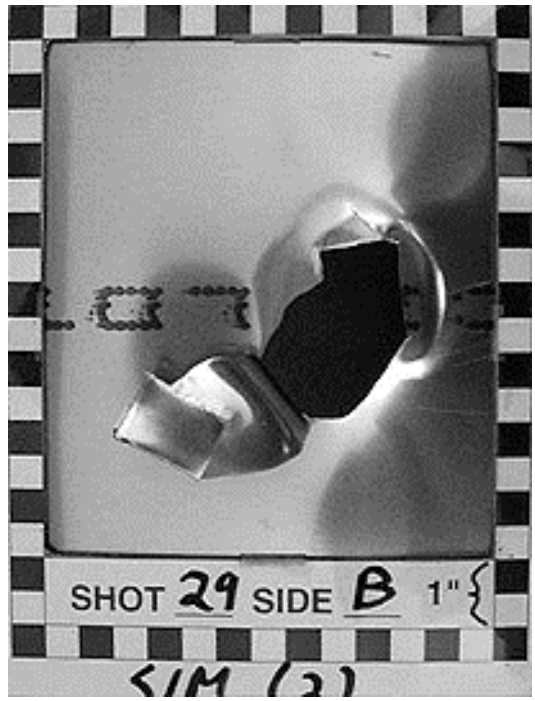

FIGURE 13. PLUGGING AND PETALING

5.2.4 Ballistic Perforation Mode and Fragment Orientation.

At the representative velocities of an uncontained engine blade fragment, the main factors which would determine the type of ballistic perforation mode encountered are the geometry and orientation of the fragment. Figure 14 illustrates three fragments at various orientation angles. Note that orientation angle is defined as the angle between the perpendicular of the fragment's trajectory to the plane of the fragment.

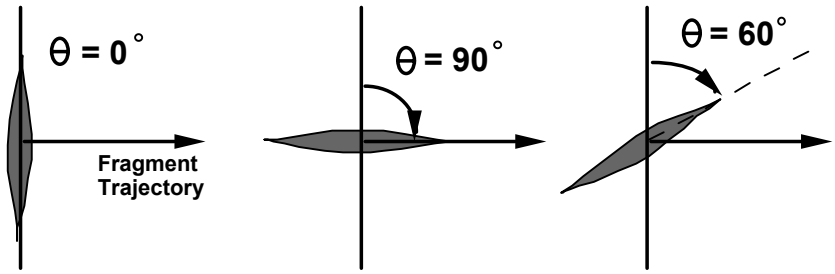

FIGURE 14. FRAGMENT ORIENTATION ANGLE

In general, plugging perforation occurs mainly for blunt projectile impacts. For the sharp-edged engine blade fragments, this would occur only for fragment orientation angles close to zero degrees. At orientation angles close to 90 degrees, we would expect multisided petaling as the target shears along both sides of the sharp-edged fragment. At orientation angles between 0° and 90°, we would expect single-sided petaling. There are some exceptions, such as impacts occurring along the flat edges of the simulated fragment.

Through analysis of the test data, it was determined that the mean fragment presented area of all tests was approximately 50% of a fragment's maximum side area. This equates to a mean orientation angle of 60 degrees. Thus we would expect that single-sided petaling would be the predominant perforation mode encountered during testing. This is confirmed by examination of the target photographs of appendix C.

5.2.5 Comparison of Perforation Mode to Penetration Efficiency.

The penetration efficiency, or ease of penetration for each of the two predominant perforation modes, may vary with respect to each other [5]. For a specified fragment, the variance in these efficiencies is mainly dependent on the thickness and material properties of the target material. The following discussion assumes a relatively thin and ductile target material, such as aircraft aluminum.

Consider again the fragments of figure 9. Each are of the same mass and material. Additionally, they each project the same presented area to the target. However, they differ in shape, and orientation with respect to the target. They may also differ in impact velocity such that penetration of their respected target is assured.

The fragment which resulted in petaling passed through the target with much more ease than the plugging fragment. This is due to the shear concentrations which formed at the interface of the petal with the target. Also, as the petal continued formation, the plate material moved away from the direction of the fragment's path. This effect is especially pronounced for single sided petaling. Additionally, the energy intensive dishing deformation observed during plugging is absent in petaling. In general, it may be stated that for aircraft aluminum targets, petaling is a more efficient (less energy absorbing) perforation mode than plugging.

The V_{50} values for petaling and plugging may be ranked with the least efficient having the highest ballistic limit value. As such, for a specified fragment at a specified impact orientation, it may be assumed that

$$V_{50,\text{Plugging}} > V_{50,\text{Petaling}}$$

5.2.6 Perforation Mode and Prediction Accuracy.

Recall that the ballistic limit equation provides an empirical estimate for V_{50}. The penetration data which was utilized to develop this equation was mainly based on the plugging type of perforation mode. Therefore, it may be assumed that for the input conditions utilized by this equation, it may provide a fair estimate of V_{50} should plugging occur. Now consider the residual velocity equation

$$V_r = \frac{\sqrt{V^2 - V_{50}^2}}{1.0 + \dfrac{\rho A_p t}{W \cos\theta}} \qquad \textit{The Residual Velocity Equation}$$

If plugging is predominant, the equation should provide a good estimate of residual velocity as the input value for V_{50} should be reasonably accurate. But what if petaling is the predominant perforation mode? As previously discussed, the ballistic limit velocity for petaling would be expected to be lower than for plugging (and as such, lower than that predicted by the ballistic limit equation). Thus by the residual velocity equation, should petaling be the observed perforation mode, we would expect the actual residual velocity to be greater than predicted

as $V_{50,Predicted} \cong V_{50,Plugging}$, then $V_{50,Petaling} < V_{50,Predicted}$

therefore $(V^2 - V^2_{50,Petaling}) > (V^2 - V^2_{50,Predicted})$, or $V_{r,Petaling} > V_{r,Predicted}$

This can be confirmed by comparing the prediction accuracy of each test shot with its respective photograph in appendix C. We note in these photographs a predominance of petaling damage for shots with actual $V_r >>$ predicted V_r.

Another causative factor may be that plugging is a major assumption which was utilized in the derivation of the residual velocity equation. It is assumed that at impact, a plug of the target material is sheared from the target. The plug is also assumed to be equal in shape and area to that of the presented area of the fragment. After formation, the plug is assumed to depart the target at the same velocity as the residual velocity of the fragment.

Another assumption utilized in the derivation is that after penetration the fragment continues to travel along its original trajectory. This assumption is important for portions of the derivation dealing with the conservation of momentum. In reality, deflection of the fragment from its original trajectory is possible. As these deflections are not accounted for, prediction inaccuracies may be expected.

5.2.7 Perimeter of Shear.

The empirical constants of the ballistic limit equation were developed under the assumption that presented area was the main fragment shape factor affecting perforation. However, assuming that plugging perforation is the predominant failure mode, the actual shearing and failure of the target occurs at the perimeter of the perforation plug. As such, it is suggested that the ballistic limit may also have some dependence on the perimeter of the presented area.

The fragments utilized in the development of the empirical constants were cubic and cylindrical in shape. The presented area and perimeter of the presented area for these shapes do not change drastically with the orientation of these fragments. However, engine blade fragments are in general relatively thin rectangles. As such, both the presented area and the perimeter of the presented area may vary greatly with orientation of these fragments.

Consider the three fragments and presented areas of figure 15. All three presented areas are equivalent. Also, all three fragments are of the same mass and material. They only differ in the shape of presented area as rectangles of decreasing width to length ratios.

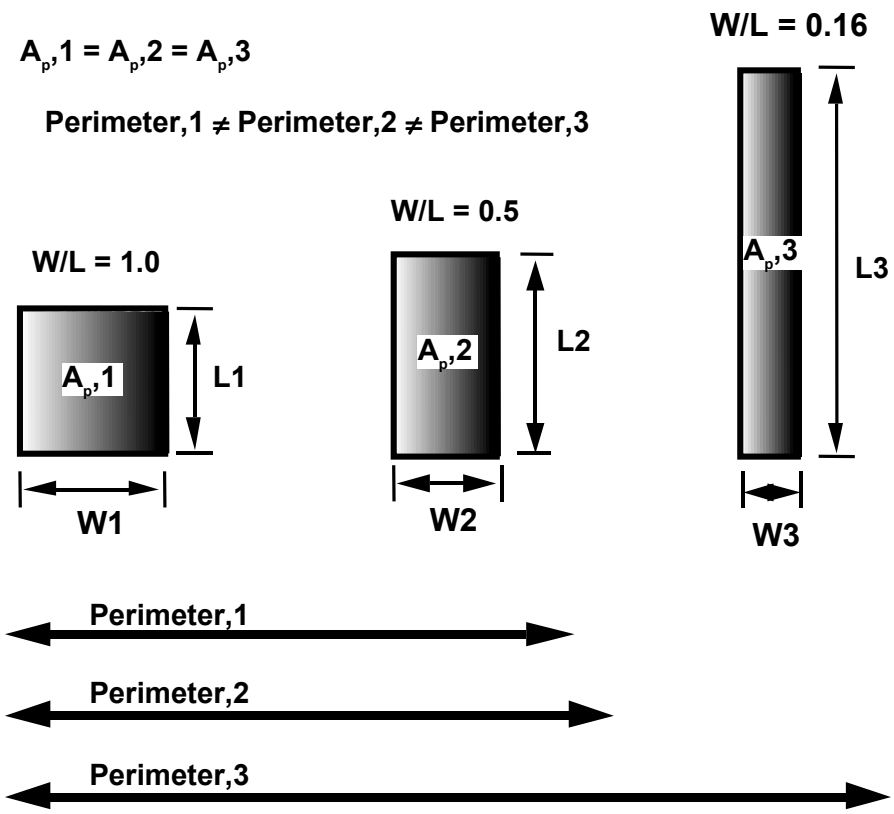

FIGURE 15. PERIMETER COMPARISON

For a given target, the ballistic limit equation would predict the same V_{50} value for all three fragments, as their weights and presented areas are equivalent. But for each fragment, consider the actual length of shear damage which would occur by plugging perforation. We would expect the extent of this damage to be proportional to the energy expended by perforation. If this shearing occurs at the perimeter of the presented area (as defined by plugging), then the expended energy should also be proportional to these perimeters.

Figure 16 compares the perimeter of a rectangle to the perimeter of a square of equivalent presented area. The plot illustrates how the perimeter of the rectangle increases with respect to the square as the rectangles width to length ratio decreases. Note that for width to length ratios above 0.6, the perimeter of the square and rectangle are approximately equal. But for width to length ratio values below 0.4, the rectangle's perimeter becomes significantly greater than the square's perimeter. Figure 17 is included as supportive evidence that the perimeter ratio does have an effect on the accuracy of the predictions.

As displayed in figure 17, individual test prediction accuracies have been plotted against the ratio of each fragment's presented area to its maximum side area. This ratio is approximately equal to the presented area's rectangular width to length ratio for fragments with side width to length ratios of greater than 0.6 (all except the turbine blades). The side area of fragments in this range approximates that of a square.

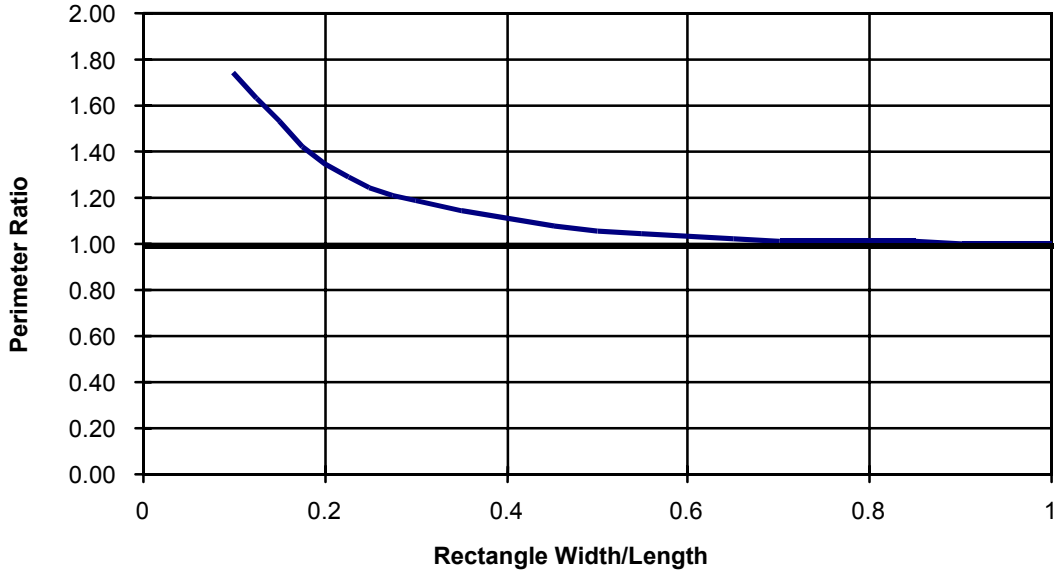

FIGURE 16. PERIMETER RATIO (RECTANGLE AND SQUARE OF EQUIVALENT PRESENTED AREA)

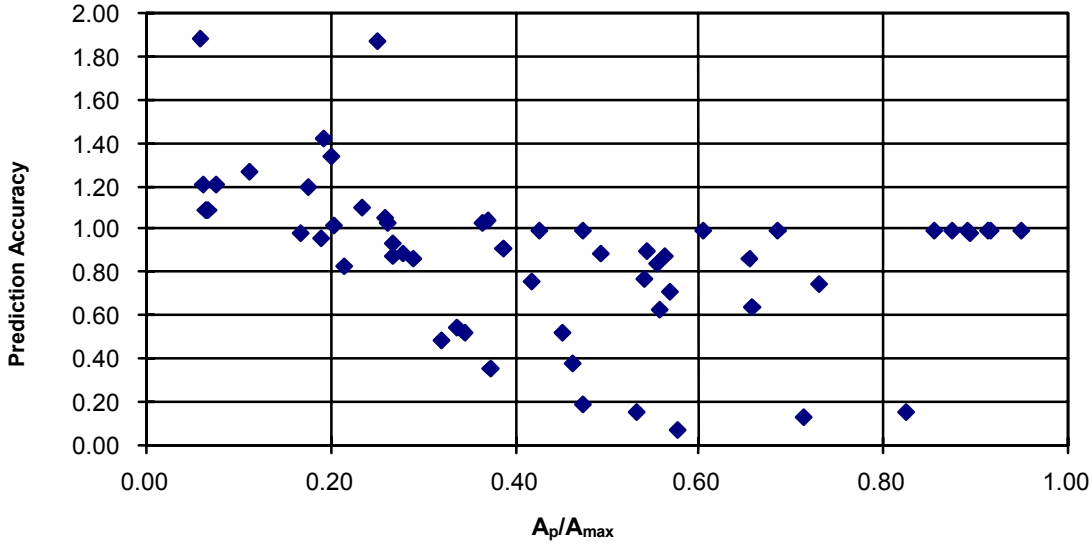

FIGURE 17. PREDICTION ACCURACY VERSUS AREA RATIO

Note in figure 17 the predominance of underpredictions (with accuracies less than one) at ratios greater than 0.6. In this range, the perimeter of the roughly square presented area is in agreement with the penetration equation's coefficients. The majority of underpredictions noted in this range are as a result of petaling. However, note that as the ratio falls below 0.4, prediction accuracies approach one. This is not that the penetration equations become more accurate in this range, but

rather that the effects of petaling are being masked by increasing overprediction errors caused by the increasing perimeter of the presented area. Eventually as the ratio falls even lower, the predictions all become overpredictions as the perimeter effect becomes pronounced at near edge-on impacts.

5.2.8 Presented Area Accuracy.

Presented area of the fragment to the target is an important dependent variable in both the residual velocity and ballistic limit equations. The accuracy of this input variable is essential when impact conditions are close to the ballistic limit. Presented area accuracy is also critical when the ratio of the fragment's maximum to minimum possible presented area is large (i.e., a large, thin, flat fragment). This may be seen in figures 18 and 19 for the simulated fragment and compressor blade respectively.

The presented area ratio for the simulated fragment is relatively small (approximately 5.6). In figure 18, the bandwidth (or distance) between edge-on and flat impact predictions is also relatively small. However, for the compressor blade the presented area ratio is much larger (approximately 28.6) than for the simulated fragment. As such, in figure 19 the bandwidth between edge-on and flat impact predictions is also much larger. Due to this large bandwidth, ballistic predictions for the compressor blade are much more sensitive to presented area input accuracy than for the simulated fragment.

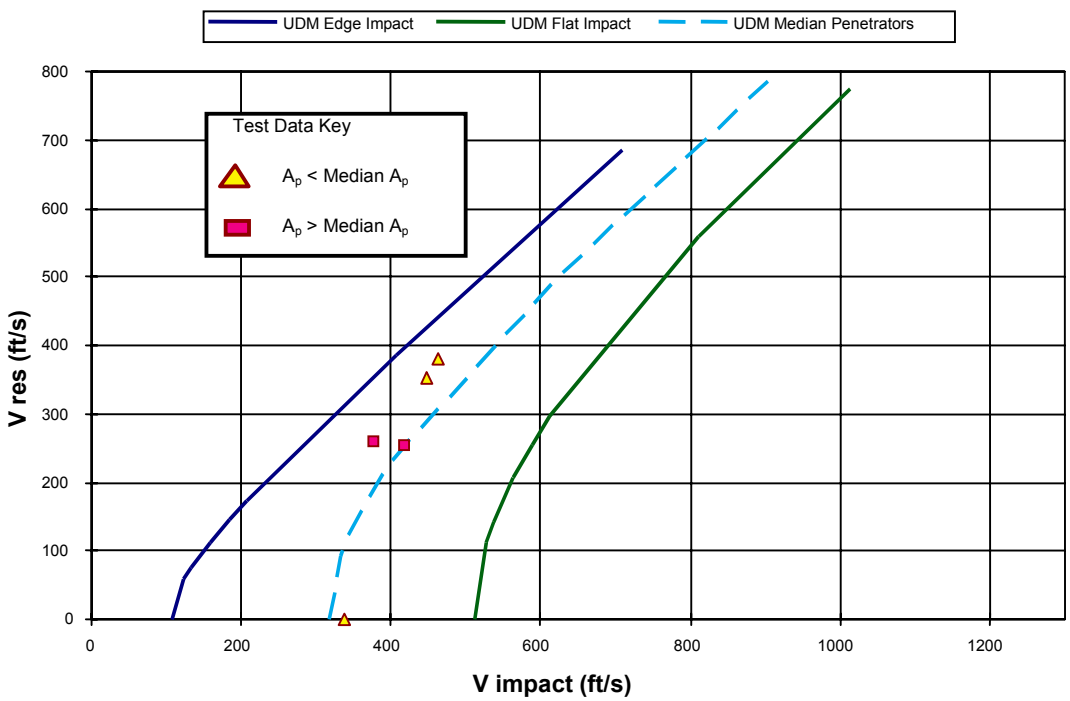

FIGURE 18. TEST SERIES 2, RESIDUAL VELOCITY CURVES ORIENTATION COMPARISON

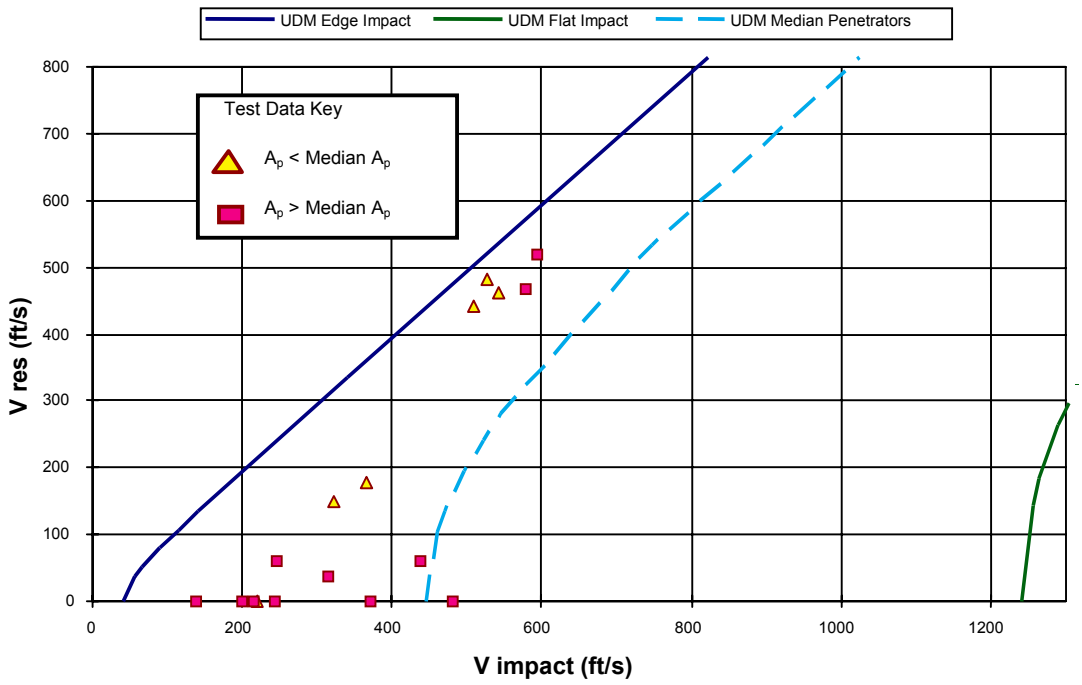

FIGURE 19. TEST SERIES 5 AND 7, RESIDUAL VELOCITY CURVES ORIENTATION COMPARISON

Figure 20 (from test series 2) illustrates the importance of presented area input accuracy for impact conditions which are close to the ballistic limit. In this figure, the presented area is varied by a relatively small amount of ± 10%. In shots 14, 31, and 32, the predictions are only minorly affected by this variation.

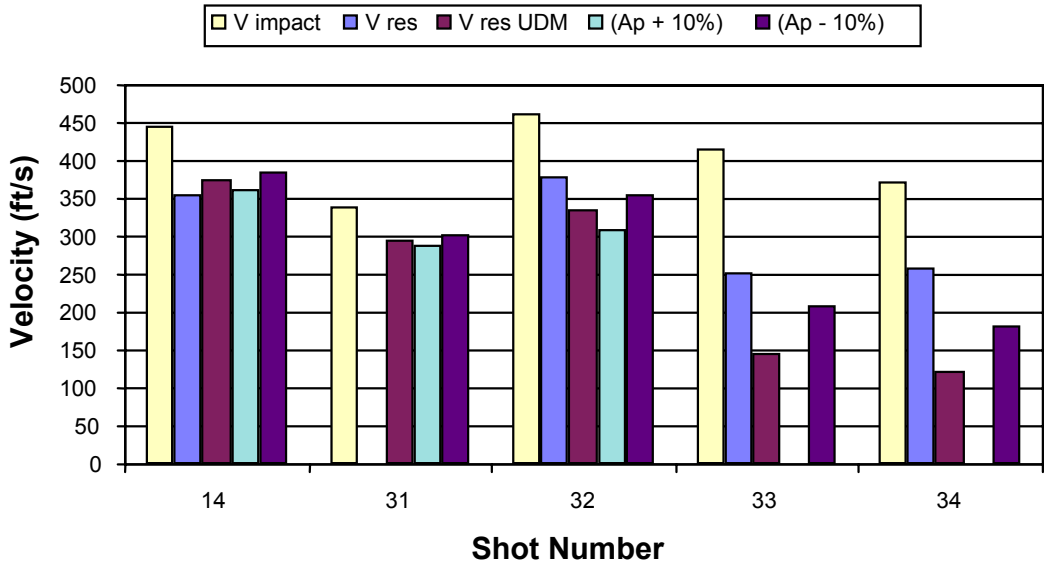

FIGURE 20. EFFECTS OF PRESENTED AREA INACCURACIES

The variations resulted in dramatic prediction differences for shots 33 and 34. An increase in presented area resulted in predictions of nonpenetration for both shots (or residual velocity = 0, as denoted by the absence of the respective bar plot). As such, we would expect these impacts to be relatively close to their ballistic limit. This is confirmed by comparing the impact velocities of these shots to their predicted ballistic limits. For shot 33, the impact velocity was 416 fps with a predicted ballistic limit of 384 fps. The impact velocity of shot 34 was 375 fps with a predicted ballistic limit of 350 fps.

As discussed, presented area must be accurately inputted to the penetration equations to assure accurate predictions. Unfortunately, the presented area must be calculated from visual high-speed film inputs which are measured during the dynamic event of impact. There are numerous factors which affect the accuracy of these calculations. This includes poor visibility of the fragment at impact. Additionally, the fragment's orientation (and thus presented area) is measured one frame prior to impact to negate the possibility of measuring orientation inaccuracies from impact induced rotation. However, if the fragment is tumbling, some rotation of the fragment will occur between film frames, resulting in further presented area inaccuracies. Finally, the fragments were assumed to be rectangular in shape to ease calculation of the presented area. In reality, the fragments are somewhat differently shaped, owing to their airfoil characteristics. The compressor blades are a notable example, with an aerodynamic twist of approximately 30 degrees along their length.

5.2.9 Target Material and Structural Characteristics.

It is assumed that new metal targets were utilized in the development of the empirical constants utilized by the ballistic limit equation. Additionally, the way these targets were supported during these tests is unknown. Both of these may be important factors in the development of these constants.

New 2024 T3 aluminum targets were utilized during test series 2 through 7. For most of these tests, the fragment impact points were distant from the target support structure. For these test series, predictions of the residual velocity were noted to be relatively close to that of the actual measured residual velocity. The notable exception to this were the results from test series number 8 which impacted the actual aluminum aircraft structure.

Test series 8 utilized P-3 Orion aircraft engine cowlings as impact targets (see figures 21 and 22). These cowlings are shaped and supported in numerous spots by aircraft stringers. Additionally, during their normal lifetime, the cowlings are expected to have been exposed to many cyclic extremes in atmospheric temperature and pressure.

Figure 23 illustrates the velocity comparisons for test series 8. Of interest is the stringer impacts which occurred for approximately half of the test impacts. It should be noted that the intended impact points were midway between the stringers for each shot. Fragment tumbling resulted in apparently random trajectory deflections causing the stringer impacts.

FIGURE 21. COWLING EXTERIOR

FIGURE 22. COWLING INTERIOR

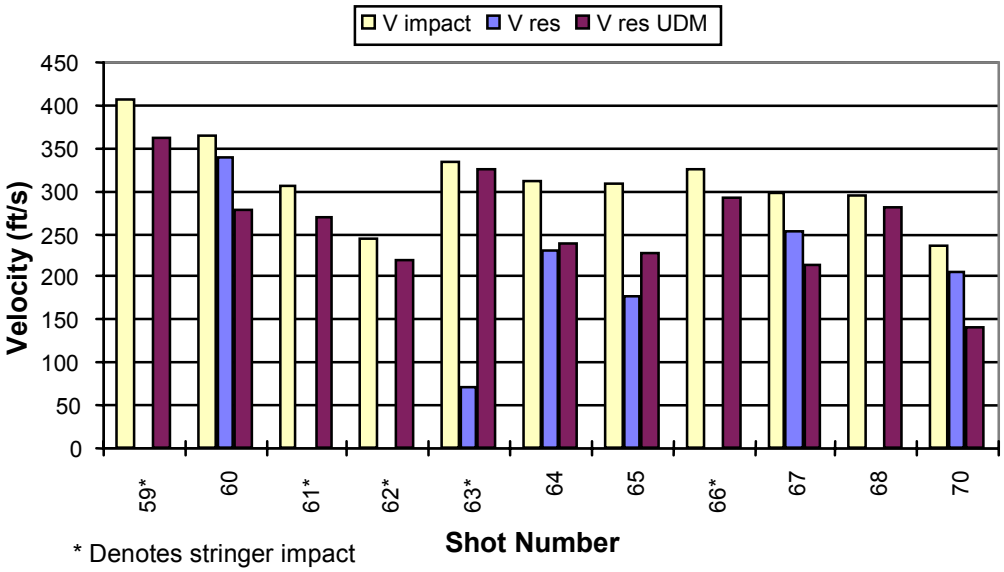

FIGURE 23. TEST SERIES 8 PREDICTION COMPARISON

Due to the randomness of the trajectory deflections, it may be possible to predict the occurrence of these impacts. This could be achieved by randomly plotting (on a computer) the previously mentioned mean presented area (50% of the maximum side area) within the area bounding the stringers. Instances where the presented area overlaps a stinger would be counted and compared with the total number of plots to arrive at a probability of stringer impact.

The residual velocities for tests which resulted in stringer impacts are, as intuitively expected, much lower than predicted. As such, it may be concluded that stringer placement density does provide some mitigation of uncontained engine failure.

Figure 24 illustrates velocity predictions for cowling tests which resulted in non-stringer impacts. Of interest is the large underprediction of residual velocity for shots 60 and 67. As seen in the impact photographs of figures 25 and 26, these shots did result in actual plugging failure. We would expect the predictions for these tests to be relatively accurate.

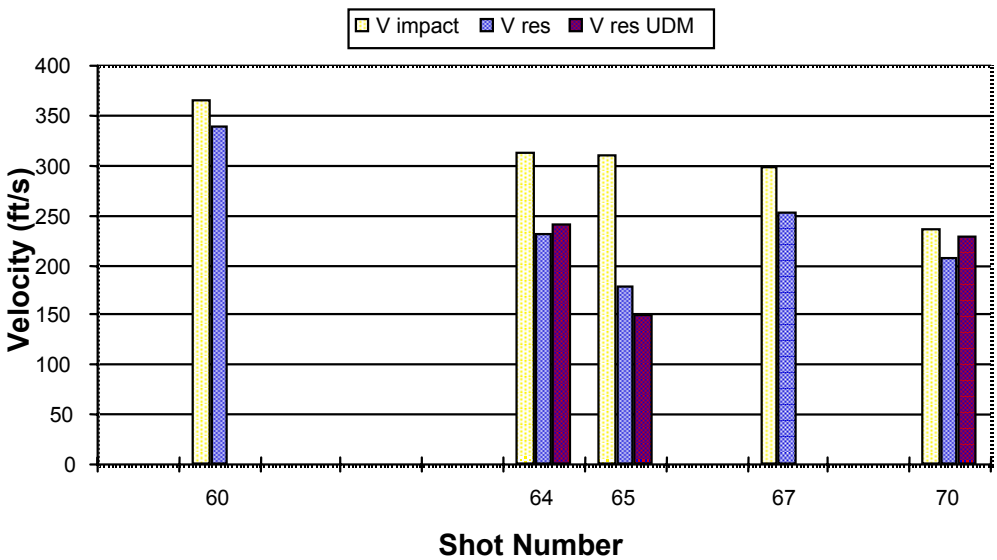

FIGURE 24. TEST SERIES 8 PREDICTIONS (SKIN IMPACTS ONLY)

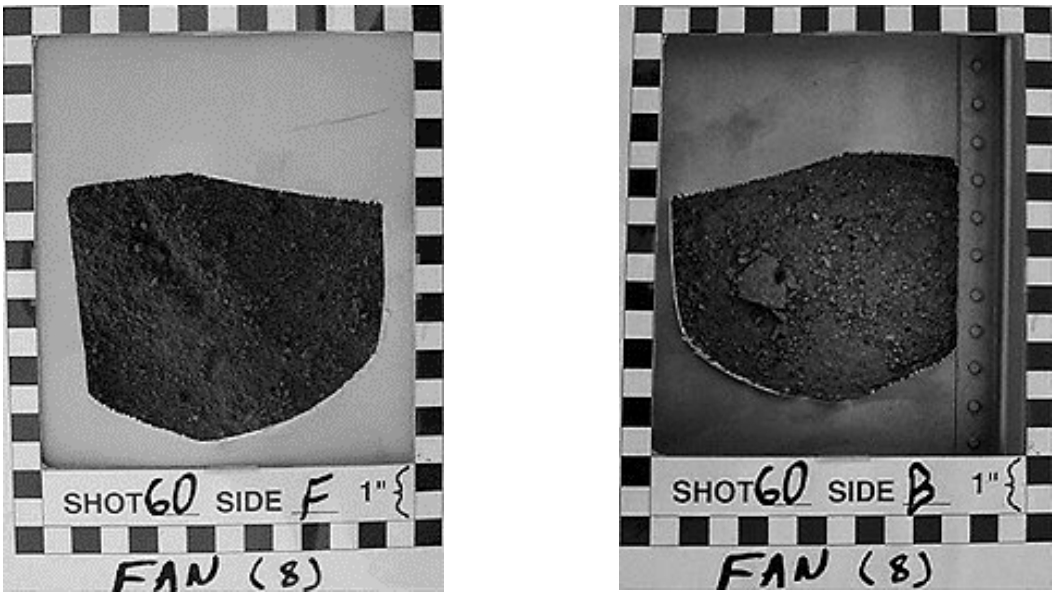

(a) (b)

FIGURES 25. PLUGGING FAILURE, SHOT 60 FRONT (a) AND BACK (b)

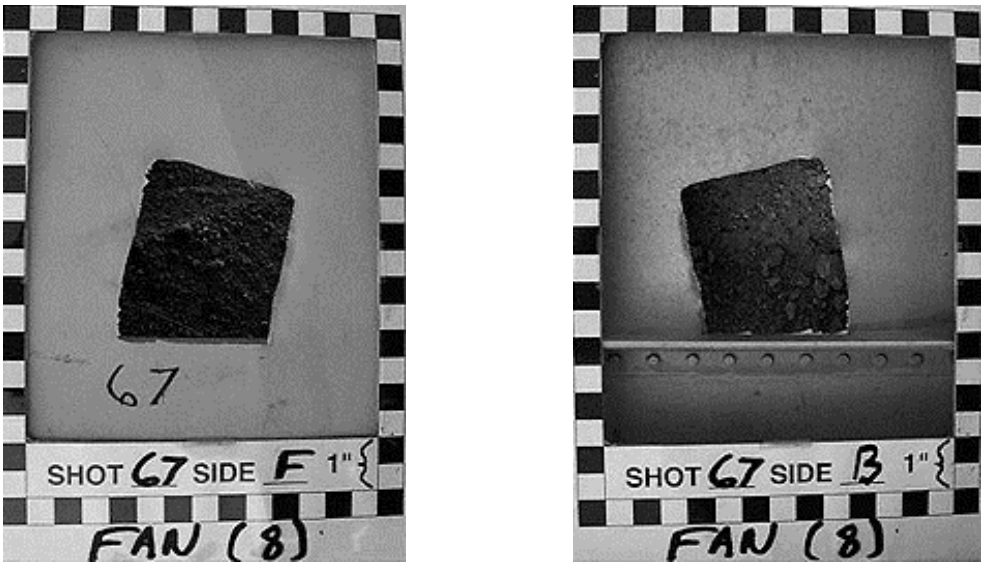

(a) (b)

FIGURES 26. PLUGGING FAILURE, SHOT 67 FRONT (a) AND BACK (b)

Explanation of these results are difficult. One causative factor may be due to the unavailability of penetration equation coefficients for the material that the cowlings were composed of (7075 T6 Aluminum). Coefficients for 2024 T3 aluminum were used instead. Although 7075 is of increased strength than 2024, it is also more brittle. As such, it may be more susceptible to impact failures.

Another explanation may attribute these results to changes in the material characteristics of the cowlings which were incurred during their normal lifetime of service. Environmental extremes which these cowlings experienced may have resulted in a tempering of the aluminum, making the metal more susceptible to impact.

Another explanation may be that in addition to temperature extremes, these cowlings were exposed to high degrees of humidity in a salt laden atmosphere. The P-3 is utilized as a maritime patrol aircraft and normally flies missions at very low altitudes over the ocean for extended durations. Corrosion of the metal from numerous exposures to the sea air may have weakened the ballistic resistance of these targets.

Finally, all of the impacts occurred very close to or on top of an aircraft stringer. This is due to the high placement density of stringers on this structure. It is clear that those fragments which impacted a stringer would probably have a lower residual velocity than predicted. However, it is unclear as to how the stringers may contribute to impacts which occur very near, but not on top of, their placement.

5.2.10 Rotational Versus Linear Kinetic Energy.

As previously discussed, many of the fragments tumbled severely due to their aerodynamic shape. Some concern may arise that the influence of the fragment's rotational kinetic energy may

be of significance in the ballistic predictions. The most significant tumble occurred for tests which utilized the compressor blades. The aerodynamic twist of these blades induced a high rate of rotation along their longitudinal axis.

The kinetic energy (rotational and linear) may be calculated by the following relation:

$$KE_{rotational} = I\omega^2$$
$$KE_{linear} = 1/2\ mV^2$$

I = Mass moment of inertia about the rotational axis
ω = Rotational velocity (radians/s)
m = Fragment's mass
V = Impact velocity

Assuming a thin rectangular plate as the fragment, the mass moment of inertia about the fragment's longitudinal axis may be calculated as $I = 1/12\ mW^2$, where W is the fragment's width (for the compressor blades, W = 2.75 inches).

Taking care to utilize consistent units, a comparison of the rotational to kinetic energy for the compressor blade fragments is presented in table 1 and displayed graphically in figure 27. These presentations clearly illustrate that although the fragments are tumbling at a very high rotational rate, their rotational kinetic energy is negligible in comparison to their linear (or translational) kinetic energy. As such, the influence of the rotational kinetic energy is also negligible to the dynamics of impact.

TABLE 1. TEST SERIES 5 AND 7, KINETIC ENERGY TABULAR COMPARISON

Shot Number	Fragment Mass (grams)	Rotational Velocity Along Longitudinal Axis (revs/s)	Linear Impact Velocity (ft/s)	Rotational Impact Kinetic Energy (ft.lbs)	Linear Kinetic Energy (ft.lbs)
41	71.9	165	539	23	716
42	70.9	99	508	8	627
43	71.5	62	366	3	328
45	73.1	124	315	13	249
46	69.4	99	199	8	94
47	69.3	52	246	2	144
48	69.6	26	139	1	46
49	71.9	41	219	1	118
50	70.2	50	214	2	110
51	69.4	0	243	0	140
52	69.3	71	323	4	248
53	69.4	71	372	4	329
54	71.9	0	437	0	470
55	70.2	99	481	8	556
56	71.9	83	593	6	866
57	69.4	83	578	6	794
58	69.4	0	526	0	658

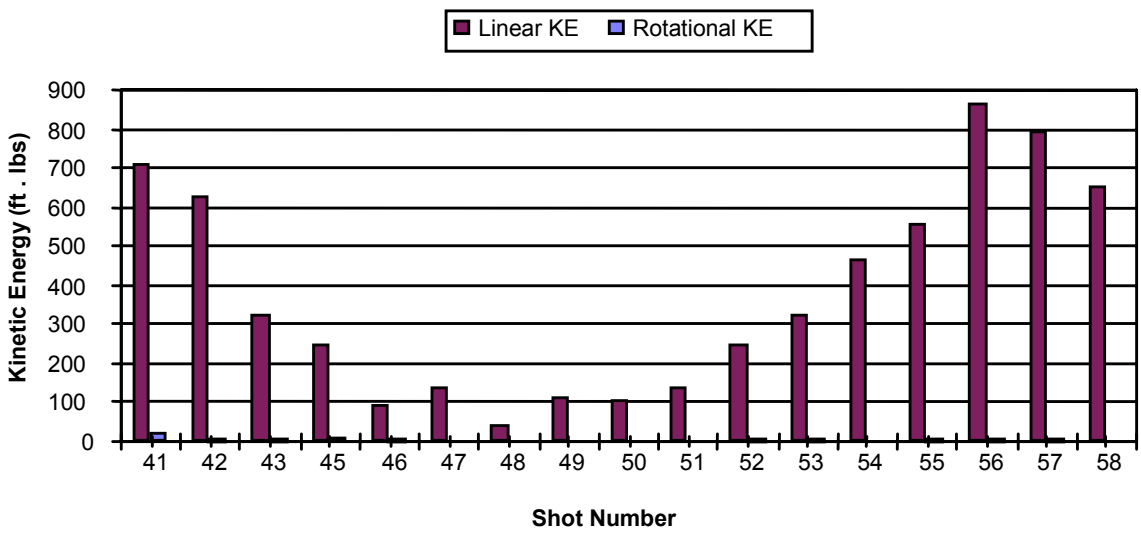

FIGURE 27. TEST SERIES 5 AND 7, KINETIC ENERGY GRAPHICAL COMPARISON

5.3 DISCUSSION OF RESULTS.

5.3.1 Prediction Accuracy (All Test Series).

Figure 28 displays the distribution histogram based on the prediction accuracies for all test series. Unintentional impacts with structural components (stringers) which occurred during test series 8 (cowling tests) are not included within the histogram. The graph displays the number of predictions which fall within each accuracy range.

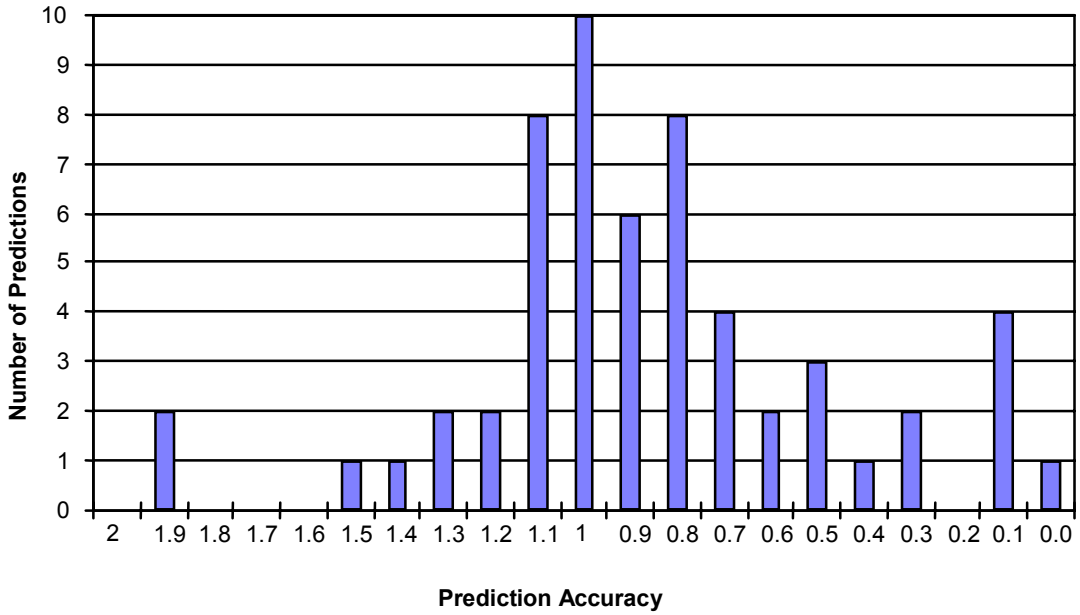

FIGURE 28. PREDICTION ACCURACY DISTRIBUTION

As seen in the graph, the majority of prediction accuracies were less than one. The arithmetic mean for all test predictions was 0.881 with a standard deviation of 0.36. (Or the average prediction fell within the range of 0.521 to 1.241). It may be concluded that for the majority of the test shots, the penetration equations had a tendency to underpredict the residual velocities of the fragments (as expected due to petaling induced errors).

5.3.2 Prediction Accuracy by Fragment Type.

Figure 29 graphically displays the mean prediction accuracy for each type of fragment tested. The standard deviation for each of these accuracies is also displayed.

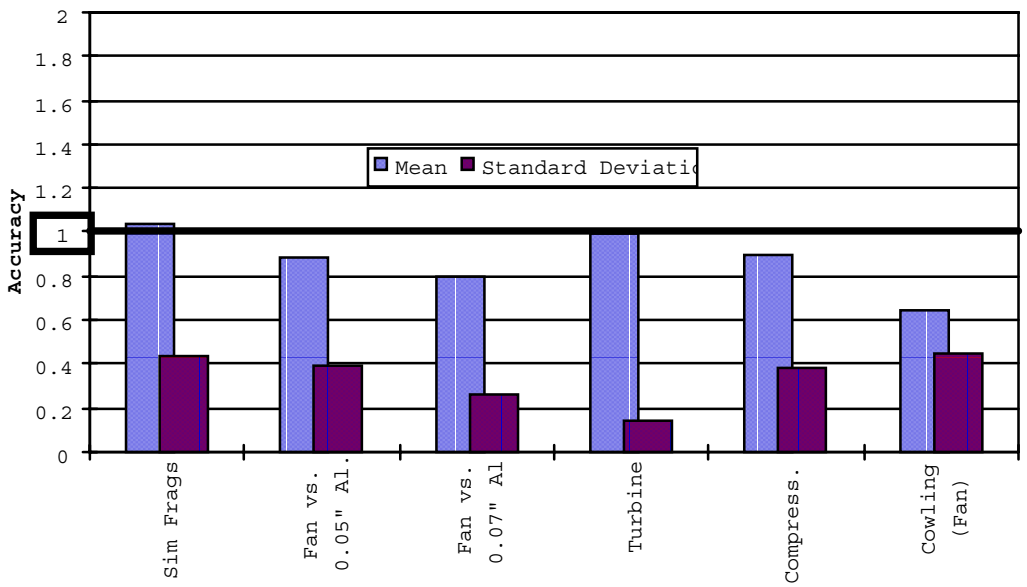

FIGURE 29. PREDICTION ACCURACY BY FRAGMENT TYPE

Note that the turbine blades provided the most accurate predictions while also maintaining the least standard deviation (Mean 0.99/Standard Deviation 0.14). This may be attributed to the highly rectangular shape of these type of fragments. Perimeter shear error may be an influential factor for these type of fragments, effectively countering target petaling induced errors.

The least accurate predictions were those calculated for the engine cowling shots with a large emphasis of underpredictions of residual velocity (Mean 0.65/Standard Deviation 0.45). It should be noted that those tests which resulted in stringer impacts were not considered in figure 29. The large error in predictions may be attributed to the type and condition of the target material. The only ballistic limit empirical constants which are available for aluminum are those for 2024 T3 aluminum. The cowlings were constructed of 7075 T6 aluminum. As such, 2024 T3 aluminum constants were utilized as a substitute. Also, the cowlings had been aged through a normal aircraft life cycle of environmental extremes. Additional degradation in material condition may have occurred due to extended open air storage near a high salt content dry lake bed (China Lake).

Predictions for the remainder of engine fragments (fan and compressor blades) were similar in accuracy and standard deviation. Mean prediction accuracies for these fragments were fair (0.80-0.90) with the predominance of underpredictions being attributed to petaling induced error. However, standard deviation values were also somewhat large for these fragments (0.26-0.39). These large deviations may be attributed to the large, but thin shape of the fragments. Variations in fragment orientation for each impact resulted in large variations in the shape of the presented area. As such, perimeter shear error varied greatly between each shot, with resultant large deviations in prediction accuracy.

5.3.3 Prediction Accuracy by Prediction Model.

Large deviations in prediction accuracy were noted for predictions of fan and compressor blade's residual velocities. Several alternative prediction models for the ballistic limit were examined to determine their benefits over the current model. These models were evaluated and compared in performance with the JTCG/ME ballistic limit equation for fragments.

There were three alternative ballistic limit models considered. These included the JTCG/ME ballistic limit equation for projectiles [1]. This equation is similar to the fragment equation, but was developed to better account for petaling effects. Other equations considered included the "FAA Energy Equation" [6]. This equation was selected for comparison due to its inclusion of perimeter shear as a dependent variable. Also, a modified form of the FAA energy equation was evaluated to determine prediction enhancements through modification of the equation's empirical constant.

A graphical comparison of the performance of these models is displayed in figure 30. The chart outlines the mean prediction accuracy of each model as a function of projectile type (fan, compressor, and turbine blades). Similarly, standard deviation (SD) is also presented for each model.

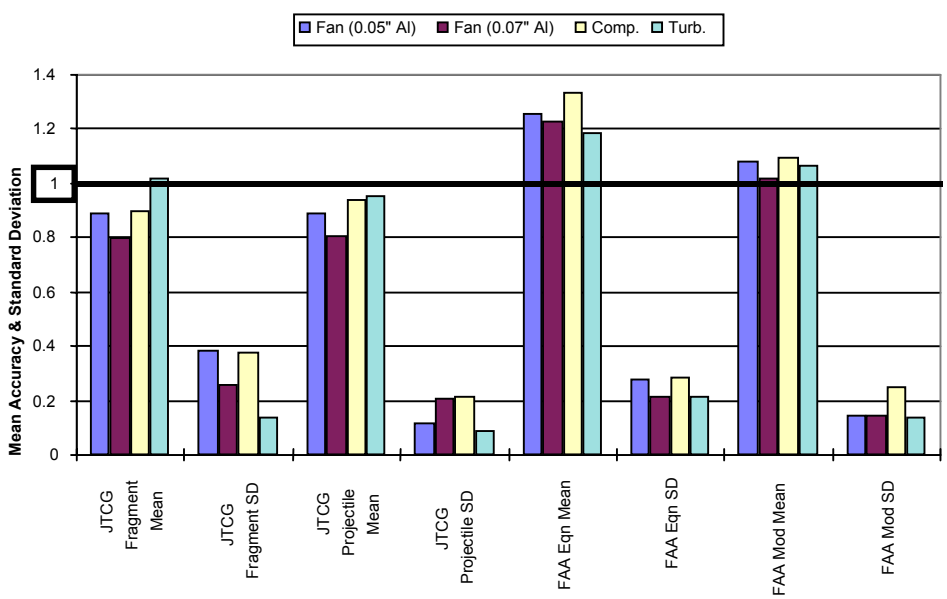

FIGURE 30. PREDICTION ACCURACY BY PREDICTION MODEL

As seen in figure 30 and below in table 2, all three of the alternative equations provide improved standard deviation of the mean prediction values. Of the three, the FAA energy equation (with modified constant) provided the most accurate predictions while maintaining the least standard deviation. Modification of the constant was achieved by numerically curvefitting the equation's empirical constant to the test data. Although the equation should provide good results for 2024 T3 aluminum, its performance is unknown should predictions for other materials be desired.

TABLE 2. PREDICTION ACCURACY BY PREDICTION MODEL

	Fan Blades (0.05" Al.)	Fan Blades (0.07" Al.)	Compressor Blades	Turbine Blades	All Test Series
JTCG Fragment	0.89/0.39	0.80/0.26	0.90/0.38	1.02/0.14	0.88/0.36
JTCG Projectile	0.89/0.12	0.81/0.21	0.94/0.22	0.96/0.09	0.87/0.27
FAA Energy Equation	1.26/0.28	1.23/0.22	1.34/0.29	1.19/0.22	1.25/0.26
FAA Energy Equation (Mod)	1.08/0.15	1.02/0.15	1.10/0.25	1.07/0.14	1.06/0.20

Of the three alternate equations, the one which is the most suitable for current use is the JTCG/ME equation for projectiles. Although the mean prediction accuracy of this equation is similar to that of the fragment equation, standard deviation is greatly reduced. This is due to better accounting for petaling effects in the equations empirical constants. Additionally, the database of empirical constants for this equation is more comprehensive with respect to common aircraft materials (including 7075 T6 aluminum and 2024 T3 aluminum).

It should be noted that the presented area is still the main dependent variable which accounts for fragment orientation within this equation. As such, error induced by perimeter shear is still present within the projectile equation.

6. SUMMARY.

The testing covered in this report was conducted to verify the effectiveness of the JTCG/ME penetration equations. In particular, the testing validated the equation's ability in predicting the residual velocity of representative jet engine blade fragments.

Limitations of the equations were identified which influence the accuracy of the predictions. It was determined that prediction accuracy was mainly dependent on the type of perforation mode incurred during each impact.

Those penetrations which resulted in plugging perforation of the target were the most accurate, as data from plugging perforations was utilized in the development of the penetration equations. However, prediction accuracy was degraded when petaling was the predominant perforation

mode. In nearly all cases, petaling perforation resulted in significant underprediction of the fragment's residual velocity.

The actual shear length along the perimeter of the presented area was suggested to be a possible influential factor for near edge-on impacts of the engine fragments. Overprediction of the fragment's residual velocity may be expected for these impacts. This is mainly due to the difference in fragment shape between the engine fragments and the fragments utilized in the development of the penetration equations.

Other limitations included unknown degradations to the target material which may occur from aging. The importance of presented area accuracy was stressed for impact conditions which are close to the ballistic limit. Finally, contribution of the fragment's rotational kinetic energy was determined to be of minor significance.

7. CONCLUSIONS AND RECOMMENDATIONS.

From the compilation of the results of all tests, the JTCG/ME penetration equations performed adequately. However, the particular prediction limitations of the ballistic limit equation for fragments must be noted. As discussed, these limitations are mainly due to petaling perforation and perimeter shear induced errors.

Of the alternative ballistic limit equations considered, the JTCG/ME ballistic limit equation for projectiles proved the most suitable for current use. This is due to the equation's better accounting for petaling induced errors, which effectively reduced the standard deviation of mean prediction accuracy. Additionally, the equation offers a more comprehensive empirical constant database of common aircraft materials.

The FAA Energy Equation (with modified constant) proved the most accurate of all the alternative ballistic limit equations. This was achieved through numerical curvefitting of the equation's empirical constant to the test data (for 2024 T3 aluminum). The equation also offers the benefit of conservative overpredictions of the residual velocity. This equation is recommended for current use with 2024 T3 aluminum only. It is also recommended that its use be expanded as test data (and thus empirical constants) become available for other common aircraft materials.

To ease analysis and evaluation of the penetration equations, all of the tests were conducted with normal impacts of the targets. It is currently unknown if oblique target impacts would provide the same results. It is thus recommended that some future testing be conducted to evaluate these equation's prediction performance in oblique impacts.

A high degree of unintentional stringer impacts occurred during engine cowling testing. This suggests that aircraft structural members (other than skin) may also play an integral part in engine debris damage mitigation. It is recommended that these structures also be included in the Uncontained Debris Model. It is also recommended that some testing be conducted to further

refine the role these structures play in damage mitigation. The penetration equations may thus be refined through this testing to enable post-stringer impact residual velocity predictions.

A metallurgical analysis should be conducted on the cowl material to determine the effect corrosion and/or aging may have had on the cowl door material properties and penetration test results. The results of this analysis could be reported in a subsequent report.

8. REFERENCES.

1. "Penetration Equations Handbook for Kinetic-Energy Penetrators (U)," Joint Technical Coordinating Group for Munitions Effectiveness (Anti-Air), 15 October 1985, 61 JTCG/ME-77-16, Revision 1.

2. Shockey et. al., "Advanced Armor Technology: Application Potential for Engine Fragment Barriers for Commercial Aircraft," SRI International, Federal Aviation Administration, Atlantic City International Airport, NJ, September 1997, DOT/FAA/AR-97/53.

3. Yatteau et. al., "Final Report Analytical Support for Patriot Program," Applied Research Associates, Raytheon Company, Tewksbury, Massachusetts, April 1994.

4. "The Resistance of Various Metallic Materials to Perforation by Steel Fragments," Ballistic Analysis Laboratory, Johns-Hopkins University, Baltimore, MD, BAL, April 1963, THOR TR No. 51, Confidential.

5. Ipson and R. Recht, "Ballistic Perforation by Fragments of Arbitrary Shape," Denver Research Institute, Naval Weapons Center, China Lake, CA, February 1997, NWC TP 5927.

6. P. Westine and L. Vargas, "Design Guide for Armoring Critical Aircraft Components to Protect From High-Explosive Projectiles," Southwest Research Institute, Air Force Wright Aeronautical Laboratories, Wright Patterson Air Force Base, OH, November 1980, AFWAL-TR-80-3123, JTCG/AS-80-T-002.

7. Gunderson, C., "Study to Improve Airframe Turbine Engine Rotor Blade Containment," TR FAA 7/77, FAA-RD-77-44.

APPENDIX A—DERIVATION OF THE JTCG/ME PENETRATION EQUATIONS

The Ballistic Limit Equation

The JTCG/ME Penetration Equations include a relationship for calculating the ballistic limit velocity (V_{50}). This relation may be written for a non-oblique impact as follows (subscript "n" denotes non-oblique, or normal impact):

$$V_{50n} = C_{bf}\left(\frac{\rho_f t A_p}{W}\right)^{b_f}\left(\frac{\rho_f t A_p}{W_0}\right)^{f} \tag{1}$$

Equation (1) is a non-dimensionalized form of the following empirical relation:

$$V_{50n} = 10^{c}\left(tA_p\right)^{\alpha}(W)^{-\beta} \tag{2}$$

Equation (2) is one of a series of ballistics relations developed by Johns Hopkins University for the Ballistics Research Laboratory under Project THOR. It is an empirical relation describing the ballistic limit velocity for warhead fragments of an unspecified shape impacting a metallic target.

Equation (2) includes three empirically derived constants α, β, and c for specified target materials. Further examination reveals there are only three dependent variables. These are target thickness (t), weight of the fragment (W), and presented area of the fragment to the target plate (Ap). An interpretation of these variables may be made such that for a specified target material, the only factors affecting the ballistic limit velocity are the thickness of the plate, the mass of the impactor, and the area of the target in which the impactor's kinetic energy is distributed.

It should be stressed that equation (2) requires the strict use of specified units for the variables. Thickness and presented area must be in units of inches and square inches, respectively. Fragment weight must be in units of grains weight (7000 grains = 1 Pound). The V_{50} output of the equation is in units of feet per second.

To reduce the possibility of incurring errors from the input of incorrect units into equation (2), equation (1) was developed in an attempt to non-dimensionalize these inputs. Equation (2) may be rewritten as:

$$V_{50n} = \left(\left(\frac{W_0}{\rho_f}\right)^{\alpha}(W_0)^{-\beta}10^{c}\right)\left(\frac{\rho_f t A_p}{W}\right)^{\beta}\left(\frac{\rho_f t A_p}{W_0}\right)^{\alpha-\beta} \tag{3}$$

The right two groupings of terms in equation (3) are dimensionless. Two new terms have been introduced to achieve these dimensionless groupings, but they have no influence (as they cancel) on the results of the equation. These terms include fragment specific density (ρf) and a specified reference weight constant (W_0 = 100 grains).

Comparison of equation (3) with equation (1) reveals that the empirical constants utilized by the JTCG/ME equation are in fact

$$b_f = \beta$$
$$f = \alpha - \beta$$
$$C_{bf} = \left(\frac{W_0}{\rho_f}\right)^{\alpha} (W_0)^{-\beta} 10^{c}$$

We note that b_f, and f are indeed constants, but that C_{bf} is in fact a variable. As W_o, α, β, and c are all constants, C_{bf} is dependent only on the fragment's specific density ρ_f.

In summary, equation (2) may be utilized with any type or material of fragment for a specified target material (as defined by empirical constants). However, the use of equation (1) requires the conversion of C_{bf} for fragments of different materials (or specific densities).

The Residual Velocity Equation

Derivation of the residual velocity equation is roughly outlined on pages 83-84 of the JTCG/ME Penetration Equations Handbook (61 JTCG/ME-77-16). However, many steps of this derivation are omitted within the handbook due to space constraints. The derivation of this equation is presented here in its entirety to illustrate the assumptions on which this equation is based. As such, it is hoped that users of this equation will more readily understand the limitations of the equation.

The derivation is achieved through the application of the conservation of energy and momentum for ballistic impact of a blunt projectile. The main assumptions utilized in this derivation are

Assumption #1: Assume that a plugging type of penetration occurs. At penetration, a plug is sheared from the target and is propelled forward with the penetrator along the penetrators original trajectory. The velocity of the plug will be at the same residual velocity as the penetrator.

Assumption #2: Assume that if penetration occurs for a given projectile at a specified impact orientation, the energy dissipated at penetration is a constant regardless of impact velocity. A value for this energy loss may be determined as being equal to the kinetic energy of the fragment at its ballistic limit (i.e., V_{50}).

Assumption #3: Assume that the plate is much greater in mass than the impacting projectile.

Assumption #4: It is assumed that penetration of the plate occurs in two distinct phases:

Phase 1: The penetrator is traveling at a specified impact velocity. It then impacts the target plate, resulting in a shearing of the plate which further results in the formation of a plug of plate material. The bounding area of this plug is equivalent to the penetrator's presented area at the moment of impact. The phase ends just as this shearing is completed. At this completion, the penetrator has been slowed to a postimpact velocity denoted as V(bar). The target plate has acquired some of the penetrator's momentum and is now

traveling at a postimpact velocity of V_t. The plug has been formed but has not yet accelerated.

Phase 2: Upon shearing of the plug from the plate, the plug and fragment undergo acceleration and deceleration respectively. The phase ends as both the plug and fragment achieve an equivalent residual velocity.

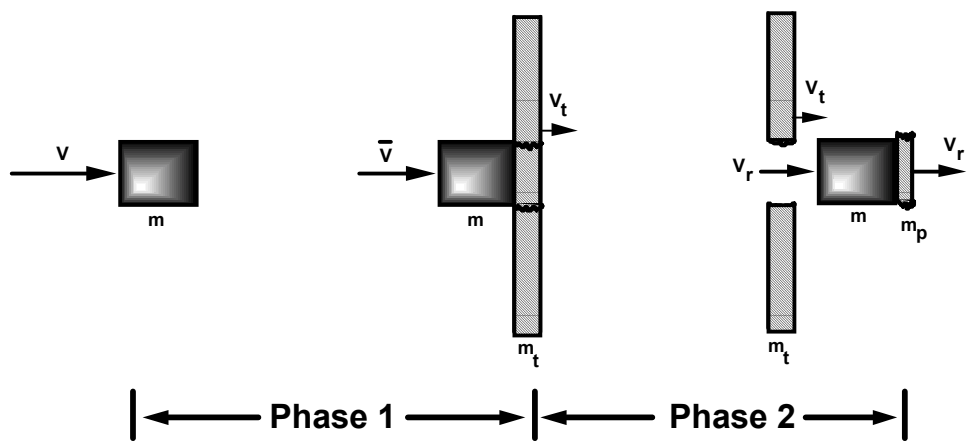

Figure A-1. Derivation of the Residual Velocity Equation

<u>Phase 1</u>.

During phase 1, the fragment is initially traveling at an impact velocity (V). It then impacts the plate resulting in momentum transfer to the plate.

By the conservation of momentum:

Fragment Impact Momentum = Fragment Post-Impact Momentum + Plate Post-Impact Momentum

$$mV = m\bar{V} + m_t V_t$$

or $$V_t = \frac{m}{m_t}\left(V - \bar{V}\right)$$

At impact, some of the fragment's kinetic energy is transferred to the plate. As such, the plate acquires some kinetic energy of its own. Also some of the fragment's kinetic energy is dissipated through deformation and shearing of the plate.

By the conservation of energy:

Fragment Impact KE = Fragment Post-Impact KE + Plate Post-Impact KE + Energy Dissipation

$$\frac{1}{2}mV^2 = \frac{1}{2}m\bar{V}^2 + \frac{1}{2}m_t V_t^2 + E_o$$

But the plate is of much greater mass than the fragment. Although the plate did acquire momentum from the impact, its acquired kinetic energy is negligible in comparison with the other terms in the energy balance. This is mainly due to the squared velocity terms in the equation. The energy equation may be rewritten as

$$\frac{1}{2}mV^2 = \frac{1}{2}m\overline{V}^2 + E_o$$

Now consider the dissipated energy term. By assumption # 2, for a given fragment and impact orientation, the energy dissipated by shear and deformation is a constant for all impacts above the ballistic limit. In effect, if the target plate fails at one velocity, impact at higher velocities will also result in failure. However, the energy dissipated by these failures is assumed to be constant. It is further assumed that this dissipated energy is equivalent to the fragment's kinetic energy at the ballistic limit. As such, the energy equation is further modified to read

$$\frac{1}{2}mV^2 = \frac{1}{2}m\overline{V}^2 + \frac{1}{2}mV_{50}^2$$

or

$$\overline{V} = \sqrt{V^2 - V_{50}^2}$$

<u>Phase 2</u>.

Phase 2 commences just after formation and release of the plug from the plate. The plug undergoes acceleration and deformation during this phase. Additionally, the fragment undergoes deceleration. The phase ends just as the plug's velocity equals the fragments velocity. The plug and fragment then continue onward at this final residual velocity.

By the conservation of momentum for phase 2:

Fragment Post-Impact Momentum = Fragment Residual Momentum + Plate Residual Momentum

$$m\overline{V} = mV_r + m_pV_r$$

But from phase 1, we know $\overline{V} = \sqrt{V^2 - V_{50}^2}$. Substituting this relation into the conservation of momentum for phase 2 yields:

$$V_r = \frac{\sqrt{V^2 - V_{50}^2}}{1 + \frac{m_p}{m}}$$

But the mass of the plug is simply the volume of the plug times its specific weight. Also the volume of the plug is equal to the area of the plug times its thickness. Note that the plug's area is also equal to the presented area of the fragment for normal impacts. However, for oblique impacts, the plug's area is equal to the fragment's presented area divided by the cosine of the

obliquity angle. Substituting into the above relation yields the final form of the residual velocity equation:

$$V_r = \frac{\sqrt{V^2 - V_{50}^2}}{1 + \frac{\rho A_p t}{W \cos\theta}}$$

It should be noted that during the acceleration of the plug and deceleration of the fragment, energy is dissipated through deformation of the plug. By the conservation of energy for phase 2:

Fragment Post-Impact KE = Fragment Residual KE + Plate Residual KE + Energy Dissipation

$$\frac{1}{2} m \overline{V}^2 = \frac{1}{2} m V_r^2 + \frac{1}{2} m_p V_r^2 + E_p$$

The energy dissipated through deformation of the plug is thus:

$$E_p = \frac{\overline{V}^2}{2\left(\frac{1}{m} + \frac{1}{m_p}\right)} \quad \text{or} \quad E_p = \frac{V^2 - V_{50}^2}{2g\left(\frac{1}{W} + \frac{1}{\rho A_p t}\right)}$$

Test Series 2: Simulated Blade Fragment vs. 0.05" Aluminum Target

Table B-1. Test Series # 2 Data Summary

Shot Number	Weight (grams)	Dimensions L × W × T (in)	Orientation Pitch/Yaw/Roll (degrees)	Presented Area (in^2)	Impact Velocity (ft/s)	UDM Ballistic Limit (ft/s)	Residual Velocity (ft/s)	UDM Residual Velocity (ft/s)	Prediction Error
14	25	1.4 × 1.0 × 0.25	0/36/14	0.52	446	209	356	376	1.05
31	25	1.4 × 1.0 × 0.25	90/45/-90	0.35	339	146	0	296	1.87
32	25	1.4 × 1.0 × 0.25	-5/-23/-65	0.76	464	294	380	336	0.90
33	25	1.4 × 1.0 × 0.25	35/-2/-1	1.02	416	384	254	147	0.74
34	25	1.4 × 1.0 × 0.25	31/-12/-8	0.92	375	350	259	125	0.64

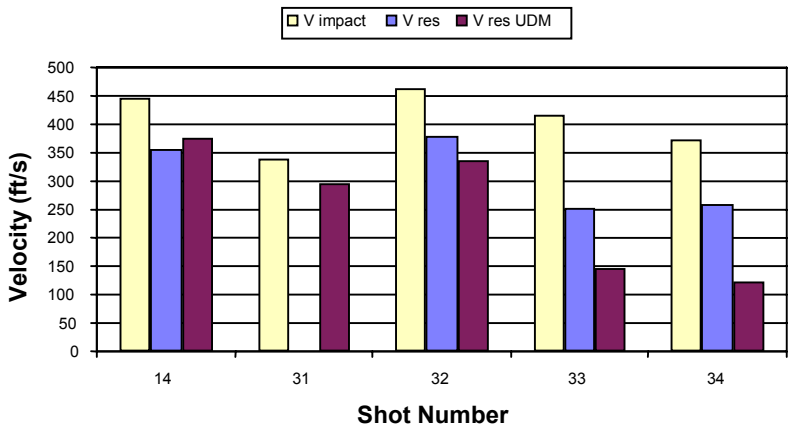

Figure B-1. Test Series 2, Impact and Residual Velocity Comparison

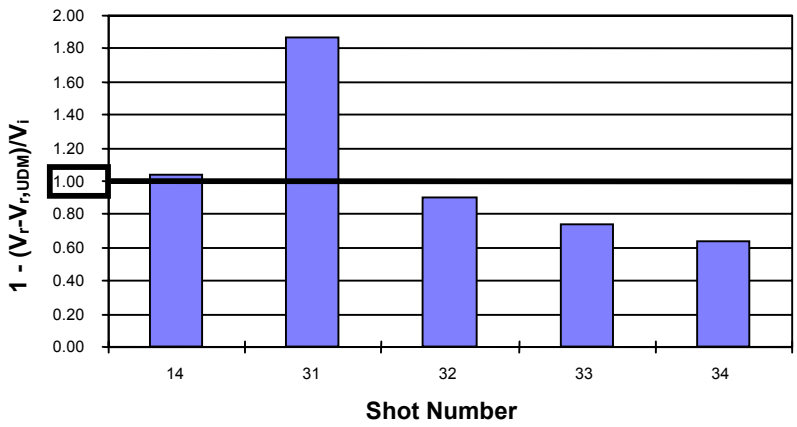

Figure B-2. Test Series 2, Prediction Accuracy

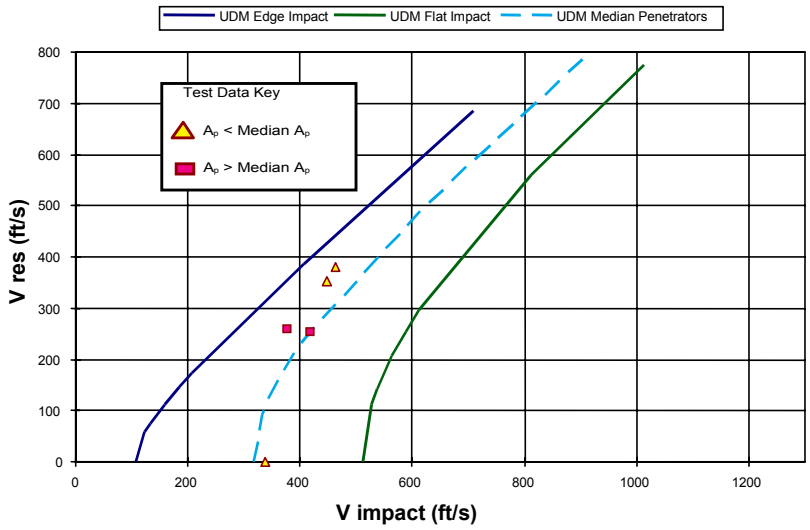

Figure B-3. Test Series 2, Impact and Residual Velocity Median Comparison

Test Series 3: Fan Blade Fragment vs. 0.05" Aluminum Target

Table B-2. Test Series # 3 Data Summary

Shot Number	Weight (grams)	Dimensions L × W × T (in)	Orientation Pitch/Yaw/Roll (degrees)	Presented Area (in^2)	Impact Velocity (ft/s)	UDM Ballistic Limit (ft/s)	Residual Velocity (ft/s)	UDM Residual Velocity (ft/s)	Prediction Error
1	162.1	4.88 × 3.06 × 0.15	-68/2/-40	12.30	483	626	408	0	0.16
3	176.9	4.25 × 3.0 × 0.17	75/0/-82	2.57	191	140	60	126	1.34
5	176.9	4.25 × 3.0 × 0.17	-7/-6/58	2.46	150	135	0	64	1.42
6	158.3	5.0 × 3.0 × 0.14	-2/-12/-56	2.85	225	171	150	141	0.96
7	151.9	5.0 × 2.81 × 0.15	41/-72/-20	12.57	241	678	4	0	0.98
8	153.4	5.0 × 3.0 × 0.14	8/6/-46	0.94	245	65	183	233	1.20
9	151.9	5.0 × 2.81 × 0.15	-59/24/-81	5.24	290	308	188	0	0.35
10	159.7	5.0 × 3.0 × 0.15	-47/11/63	4.00	321	230	233	212	0.93
17	159.7	5.0 × 3.0 × 0.15	71/17/-48	8.35	530	447	451	254	0.63
18	145.1	5.0 × 3.0 × 0.13	44/25/-84	4.35	567	272	541	466	0.87

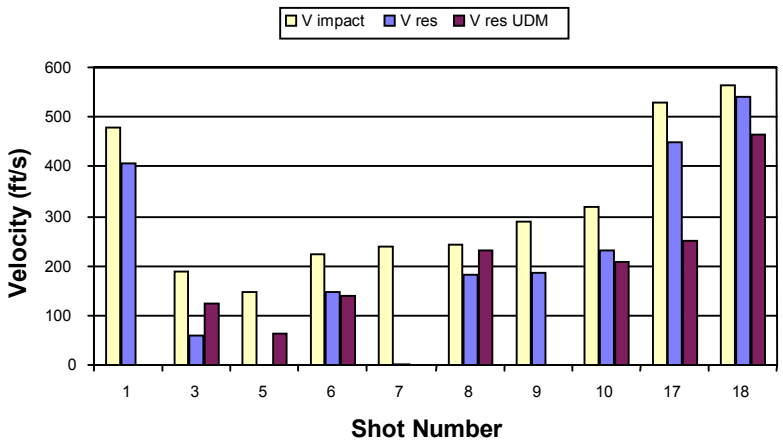

Figure B-4. Test Series 3, Impact and Residual Velocity Comparison

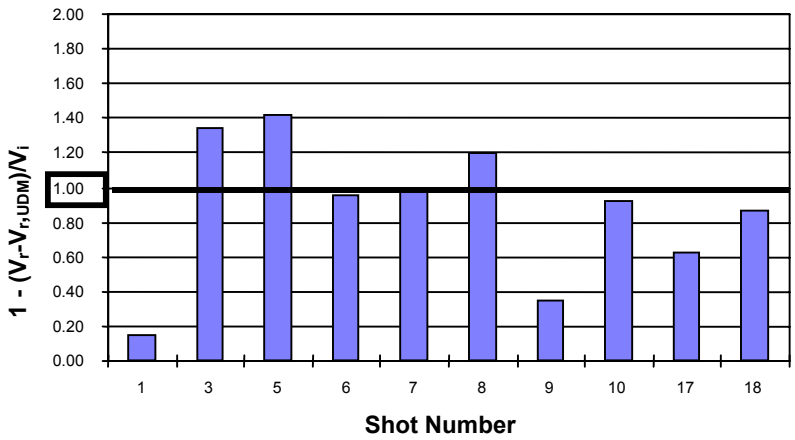

Figure B-5. Test Series 3, Prediction Accuracy

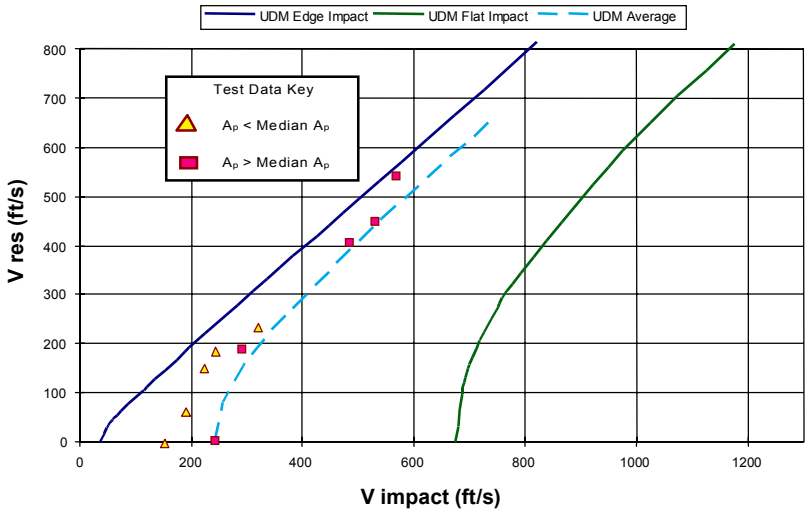

Figure B-6. Test Series 3, Impact and Residual Velocity Median Comparison

Test Series 4: Fan Blade Fragment vs. 0.071″ Aluminum Target

Table B-3. Test Series # 4 Data Summary

Shot Number	Weight (grams)	Dimensions L × W × T (in)	Orientation Pitch/Yaw/Roll (degrees)	Presented Area (in^2)	Impact Velocity (ft/s)	UDM Ballistic Limit (ft/s)	Residual Velocity (ft/s)	UDM Residual Velocity (ft/s)	Prediction Error
11	158.3	5.0 × 3.0 × 0.15	-61/0/-18	12.82	196	912	0	0	1.00
12	158.3	5.0 × 3.0 × 0.15	-51/36/45	5.17	411	402	275	79	0.52
13	151.9	5.0 × 2.8 × 0.15	-33/-26/-75	3.92	458	325	349	298	0.89
19	174.6	4.2 × 3.0 × 0.19	33/-8/-32	7.17	629	492	530	346	0.71
20	183.7	4.4 × 3.0 × 0.19	-40/46/40	2.69	484	194	414	424	1.02
21	189.5	4.2 × 3.0 × 0.21	-50/-79/-72	5.67	396	368	323	132	0.52
22	183.7	4.4 × 3.0 × 0.19	62/30/1	12.09	338	752	0	0	1.00
23	201.3	4.0 × 3.0 × 0.23	-44/85/76	7.26	210	435	0	0	1.00
26	183.7	4.4 × 3.0 × 0.19	25/-46/18	3.53	328	247	242	203	0.88
27	201.3	4.0 × 3.0 × 0.23	-13/22/-38	5.56	281	342	176	0	0.37
28	189.5	4.2 × 3.0 × 0.21	-25/-2/-49	4.02	265	270	137	0	0.48
78	158.3	5.0 × 3.0 × 0.15	-40/-50/-44	1.68	309	146	183	264	1.26

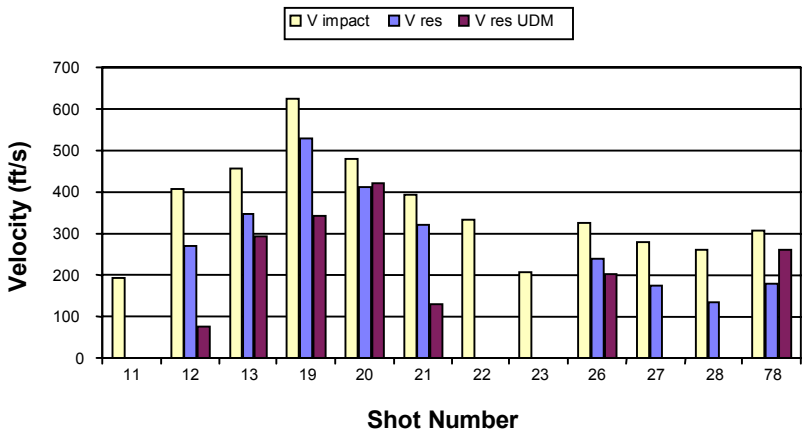

Figure B-7. Test Series 4, Impact and Residual Velocity Comparison

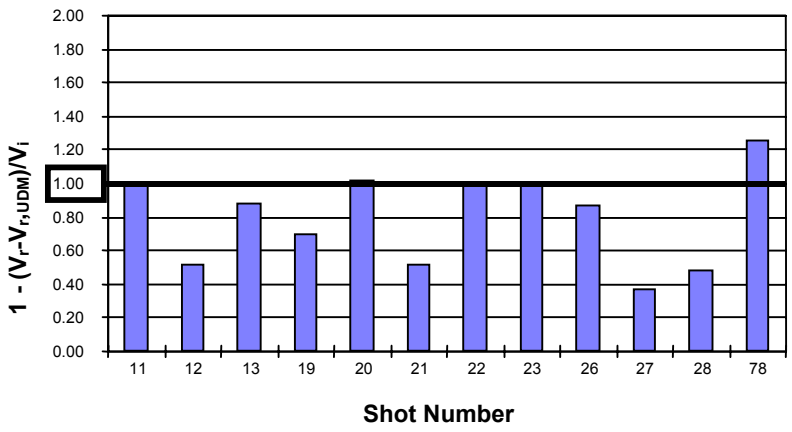

Figure B-8. Test Series 4, Prediction Accuracy

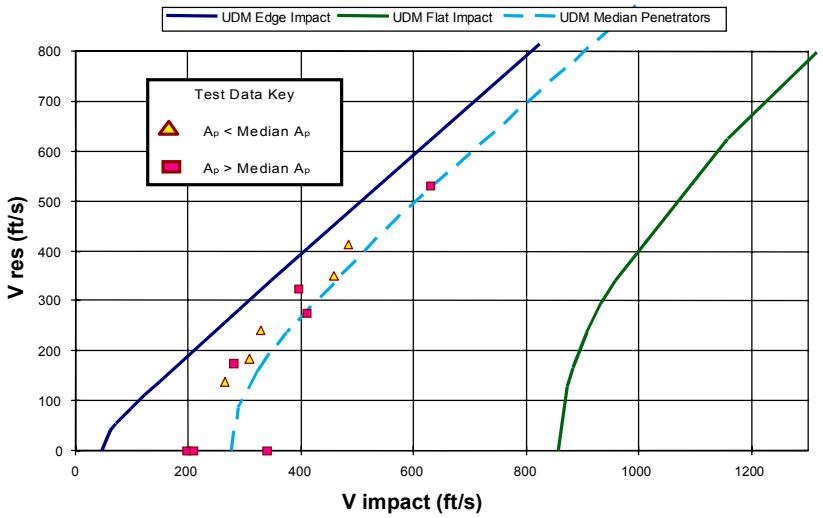

Figure B-9. Test Series 4, Impact and Residual Velocity Median Comparison

Test Series 5 and 7: Compressor Blade Fragment vs. 0.05″ Aluminum Target

Table B-4. Test Series # 5 and 7 Data Summary

Shot Number	Weight (grams)	Dimensions L × W × T (in)	Orientation Pitch/Yaw/Roll (degrees)	Presented Area (in^2)	Impact Velocity (ft/s)	UDM Ballistic Limit (ft/s)	Residual Velocity (ft/s)	UDM Residual Velocity (ft/s)	Prediction Error
41	71.9	4.0 × 2.75 × 0.09	61/-82/69	1.83	539	241	465	456	0.98
42	70.9	4.0 × 2.75 × 0.09	-2/-20/0	0.72	508	105	442	486	1.09
43	71.5	4.0 × 2.75 × 0.09	-50/20/84	1.93	366	254	179	248	1.19
45	73.1	4.0 × 2.75 × 0.09	-84/-60/-51	6.19	315	712	38	0	0.88
46	69.4	4.0 × 2.75 × 0.09	-76/8/9	10.44	199	1199	0	0	1.00
47	69.3	4.0 × 2.75 × 0.09	-44/-4/-52	4.61	246	574	59	0	0.76
48	69.6	4.0 × 2.75 × 0.09	82/21/-45	7.53	139	890	0	0	1.00
49	71.9	4.0 × 2.75 × 0.09	19/-38/31	0.64	219	93	1	194	1.88
50	70.2	4.0 × 2.75 × 0.09	-4/-29/-75	5.22	214	634	0	0	1.00
51	69.4	4.0 × 2.75 × 0.09	23/86/38	9.81	243	1133	0	0	1.00
52	69.3	4.0 × 2.75 × 0.09	-64/52/81	3.71	323	472	148	0	0.54
53	69.4	4.0 × 2.75 × 0.09	-75/63/-76	4.68	372	581	0	0	1.00
54	71.9	4.0 × 2.75 × 0.09	52/42/-18	7.21	437	830	61	0	0.86
55	70.2	4.0 × 2.75 × 0.09	70/6/27	9.61	481	1101	0	0	1.00
56	71.9	4.0 × 2.75 × 0.09	53/-7/-35	7.85	593	897	518	0	0.13
57	69.4	4.0 × 2.75 × 0.09	0/37/48	5.20	578	639	466	0	0.19
58	69.4	4.0 × 2.75 × 0.09	-67/49/-80	2.36	526	313	482	392	0.83

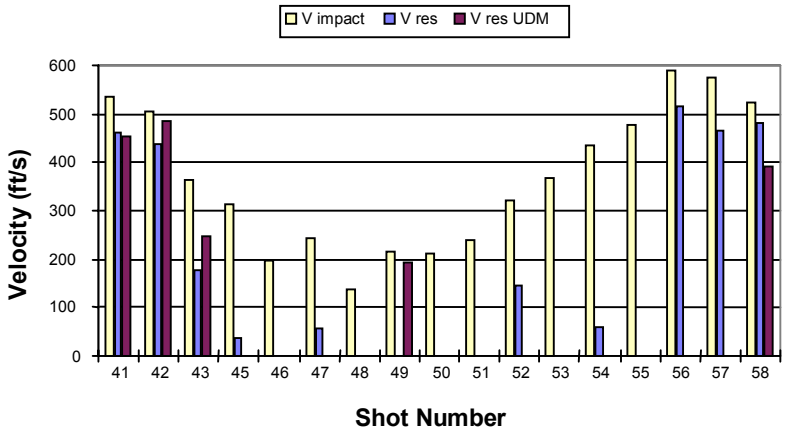

Figure B-10. Test Series 5 and 7, Impact and Residual Velocity Comparison

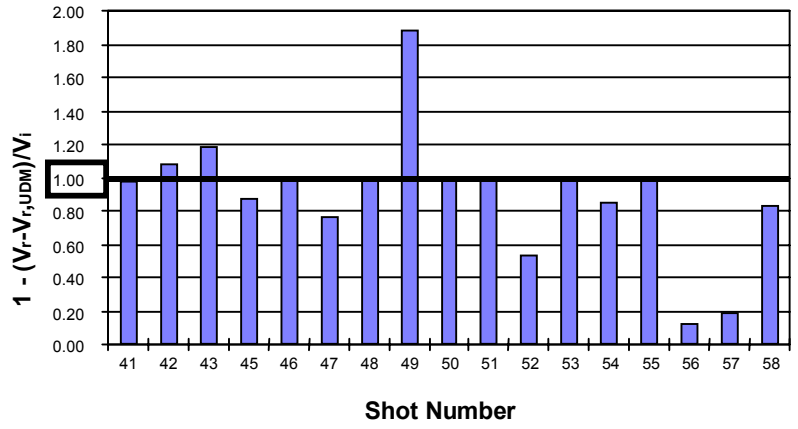

Figure B-11. Test Series 5 and 7, Prediction Accuracy

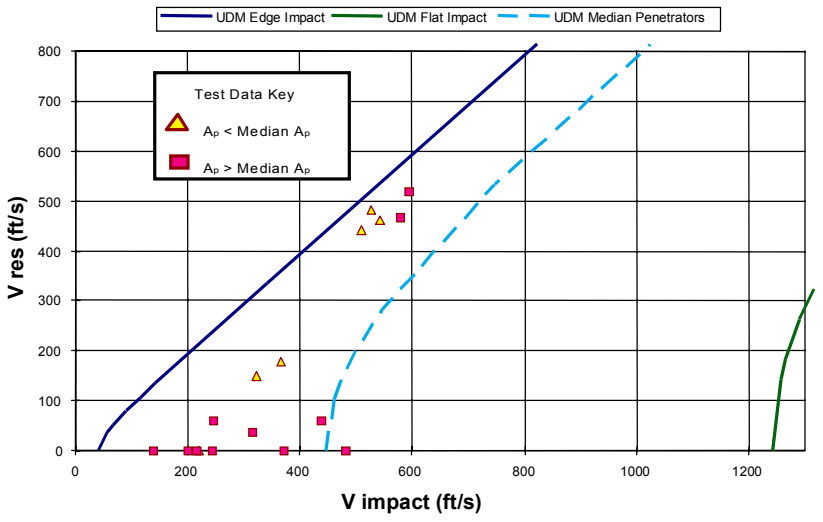

Figure B-12. Test Series 5 and 7, Impact and Residual Velocity Median Comparison

Test Series 6: Turbine Blade Fragment vs. 0.05″ Aluminum Target

Table B-5. Test Series # 6 Data Summary

Shot Number	Weight (grams)	Dimensions L × W × T (in)	Orientation Pitch/Yaw/Roll (degrees)	Presented Area (in^2)	Impact Velocity (ft/s)	UDM Ballistic Limit (ft/s)	Residual Velocity (ft/s)	UDM Residual Velocity (ft/s)	Prediction Error
35	85.6	4.0 × 1.38 × 0.12	-31/-40/-8	2.71	407	291	310	265	0.89
36	83.1	4.0 × 1.38 × 0.11	72/10/-53	2.97	367	325	243	157	0.77
37	78.4	4.0 × 1.38 × 0.11	24/-15/35	1.42	358	176	280	299	1.05
38	76.9	4.0 × 1.38 × 0.11	-68/0/16	5.02	285	562	0	0	1.00
39	77.7	4.0 × 1.38 × 0.11	17/-29/33	0.41	337	58	257	328	1.21
40	76.9	4.0 × 1.38 × 0.11	12/-22/55	1.29	319	165	230	263	1.10
44	77.3	4.0 × 1.38 × 0.11	-20/-62/-55	3.05	814	357	797	672	0.85
84	85	4.0 × 1.38 × 0.12	20/46/-47	2.00	599	223	511	528	1.03

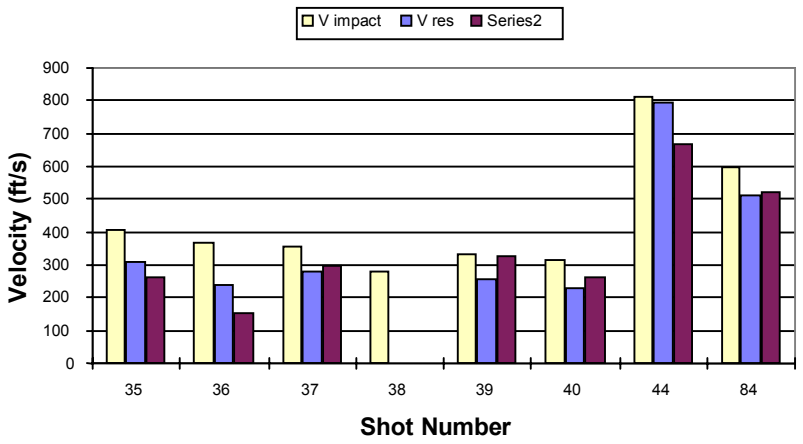

Figure B-13. Test Series 6, Impact and Residual Velocity Comparison

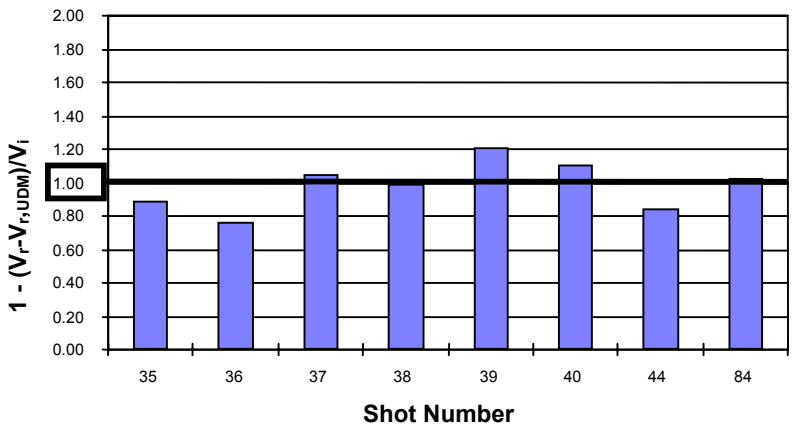

Figure B-14. Test Series 6, Prediction Accuracy

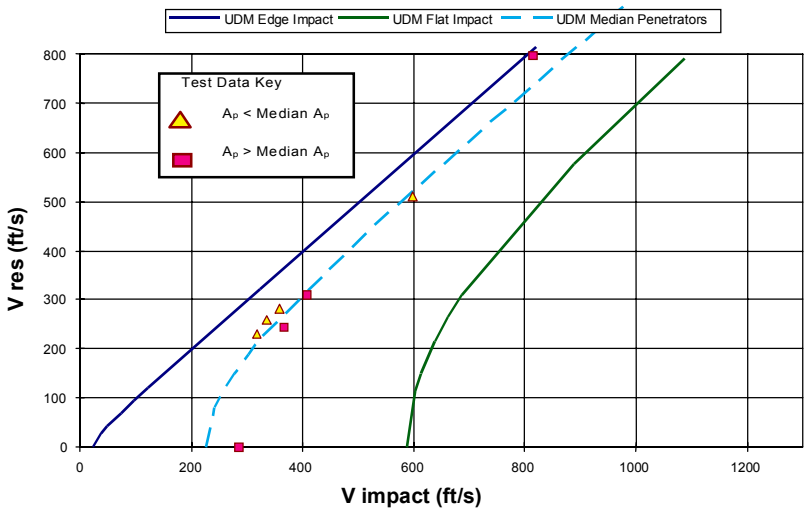

Figure B-15. Test Series 6, Impact and Residual Velocity Median Comparison

Test Series 8: Fan Blade Fragment vs. Aircraft Engine Cowling

Table B-6. Test Series # 8 Data Summary

Shot Number	Weight (grams)	Dimensions L × W × T (in)	Orientation Pitch/Yaw/Roll (degrees)	Presented Area (in^2)	Impact Velocity (ft/s)	UDM Ballistic Limit (ft/s)	Residual Velocity (ft/s)	UDM Residual Velocity (ft/s)	Prediction Error
59*	158.3	5.0 × 3.0 × 0.15	13/-53/72	10.61	407	458	0	0	N/A *
60	153.4	5.0 × 3.0 × 0.14	-26/-37/-85	8.66	367	393	341	0	0.07
61*	159.7	5.0 × 3.0 × 0.15	51/-22/0	11.92	307	504	0	0	N/A *
62*	145.1	5.0 × 3.0 × 0.13	58/-26/-17	9.21	245	437	0	0	N/A *
63*	158.3	5.0 × 3.0 × 0.15	81/19/85	2.30	335	115	74	307	N/A *
64	159.7	5.0 × 3.0 × 0.15	-79/36/-84	3.94	314	186	232	242	1.03
65	158.3	5.0 × 3.0 × 0.15	-72/-48/83	5.80	311	265	180	152	0.91
66*	152.1	4.88 × 2.88 × 0.15	44/-14/11	9.68	327	438	0	0	N/A *
67	152.1	4.88 × 2.88 × 0.15	-29/-10/12	7.48	299	347	254	0	0.15
68	152.1	4.88 × 2.88 × 0.15	87/4/75	4.42	296	216	0	193	N/A *
70	152.1	4.88 × 2.88 × 0.15	30/-35/46	0.92	238	52	208	230	1.09

* Denotes unintended impact with a structural component (stringers). Calculation of prediction accuracies have not been included due to influence of stringer impact.

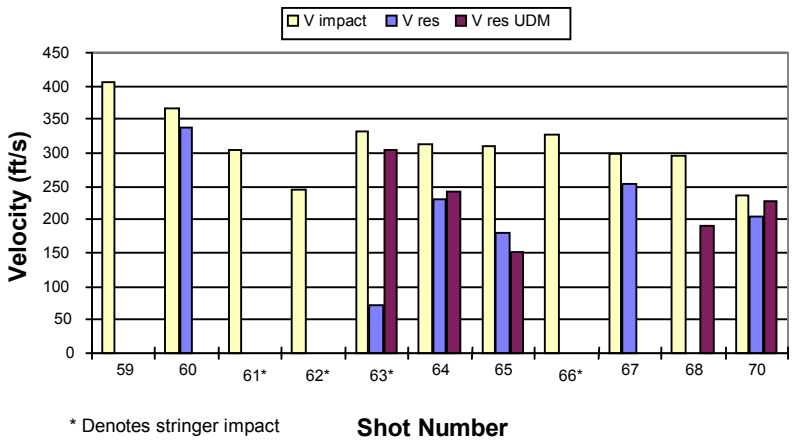

Figure B-16. Test Series 8, Impact and Residual Velocity Comparison

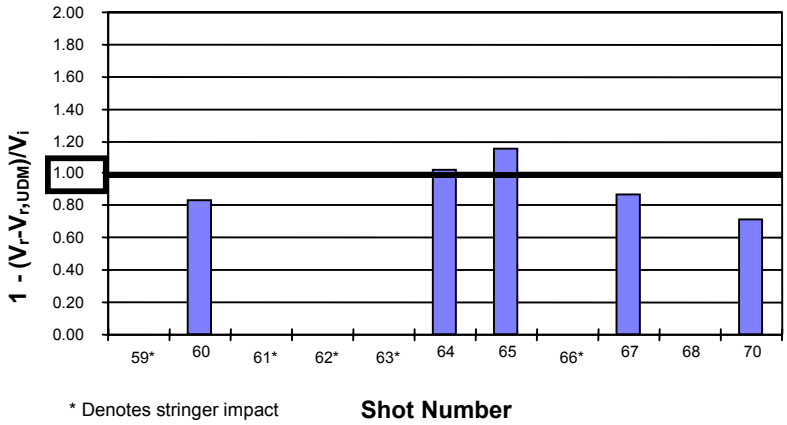

Figure B-17. Test Series 8, Prediction Accuracy

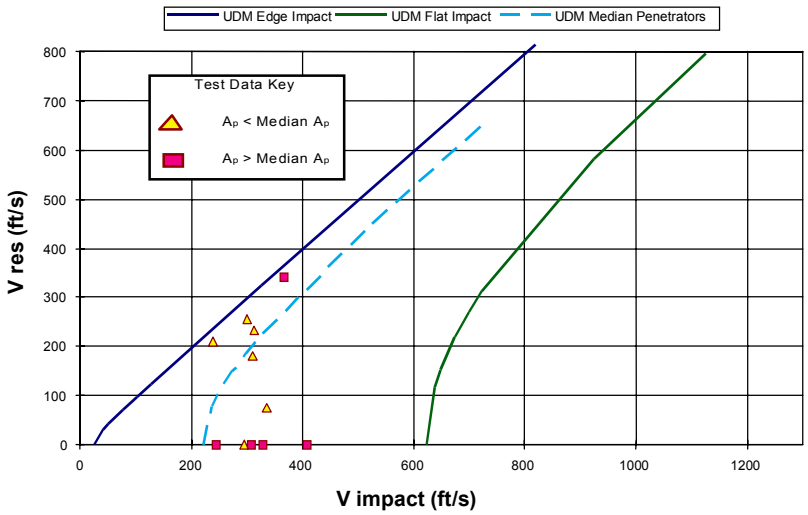

Figure B-18. Test Series 8, Impact and Residual Velocity Median Comparison

APPENDIX C—TARGET IMPACT PHOTOGRAPHS

Preface

This appendix has been included to present the test data in an easily interpreted form. The intent is to present data which may be most useful for follow-on damage prediction efforts, in particular for finite element analysis.

The data is tabulated as follows:

Target/Thickness: The material composition of the target and its thickness in inches.

Fragment/Material/Weight: The type of fragment utilized (Fan, turbine, compressor, or simulated fragment) along with its material composition and weight in grams.

Length/Width/Thickness: The length, width, and thickness of the fragment in inches. The dimensions describe an equivalent solid parallelepiped (rectangle of constant thickness) of the same material and weight as the actual test fragment. The listed dimensions for thickness are average, as most of the fragments utilized were in the shape of airfoils with varying thickness along the length of the fragment.

Pitch/Yaw/Roll: The pre-impact orientation of the fragment in terms of sequential axis rotations of pitch, yaw, and roll (degrees). For amplified discussion, please refer to the orientation discussion of the main report.

Presented Area: The pre-impact presented area of the fragment as projected along the fragment's trajectory onto the target.

Velocity Comparison (Impact/Residual/Predicted/Accuracy): The pre-impact and post-penetration residual velocity (in feet/second) of the fragment as measured by high-speed film footage. For comparison purposes, the residual velocity as predicted by use of the JTCG/ME penetration equations (for fragments) has also been included, along with this value's prediction accuracy (in comparison with the actual residual velocity).

Additional data is presented via included figures for each shot. These include:

Pre-Impact Orientation: This figure is a computer rendered illustration of the fragment and its orientation at the moment just prior to impact with the target. The fragment is centered within a three-dimensional axis describing the pre-rotation reference pitch (to the left), yaw (up), and roll (into the target) axes.

Three shadow projecting light sources have been included in the illustration. These include a light source aimed along the trajectory of the fragment and projecting a shadow of the fragment's presented area onto the target. Two additional light sources are included which project

horizontal and vertical plane shadows of the fragment, simulating pre-impact views of the fragment as seen on the high-speed camera footage.

A 1/2″ square checkerboard pattern has been utilized on the target, floor, and wall planes. This pattern has been included as a visual dimensional reference. In addition, the target perimeter has been outlined with a darkened checkerboard pattern simulating the 7.5″ × 9.5″ photographic gridboard described below and included within the actual damage photographs of each target.

Target Damage (Frontal and Rear Views): These figures are actual photographs of the post-impact damage incurred by each target. The damage has been correctly oriented and centered within a 7.5″ × 9.5″ photographic gridboard of 1/2″ checkered squares. Note that each photograph has been cropped along the edge of the gridboard. This was done to allow enlargement of each photo to emphasize the characteristics of the impact damage. As such the entire area of the target (2' × 2') is not visible within each picture. However, in nearly all test shots, the damage noted outside of the gridboard was negligible.

Test Series 2

Simulated Blade Fragment

Impacts on

0.05" 2024 T3

Aluminum

Shot 14 (Series 2)

Target / Thickness
2024 T3 Aluminum / 0.05 (in.)

Simulated Fragment Material / Weight
Titanium / 25 (grams)

Length / Width / Thickness
1.4 / 1.0 / 0.25 (in.)

Pitch / Yaw / Roll
0 / 36 / 14 (degrees)

Presented Area
0.52 sq. in

Velocity Comparison
Impact / Residual / Predicted / Accuracy
446 fps / 356 fps / 376 fps / 1.05

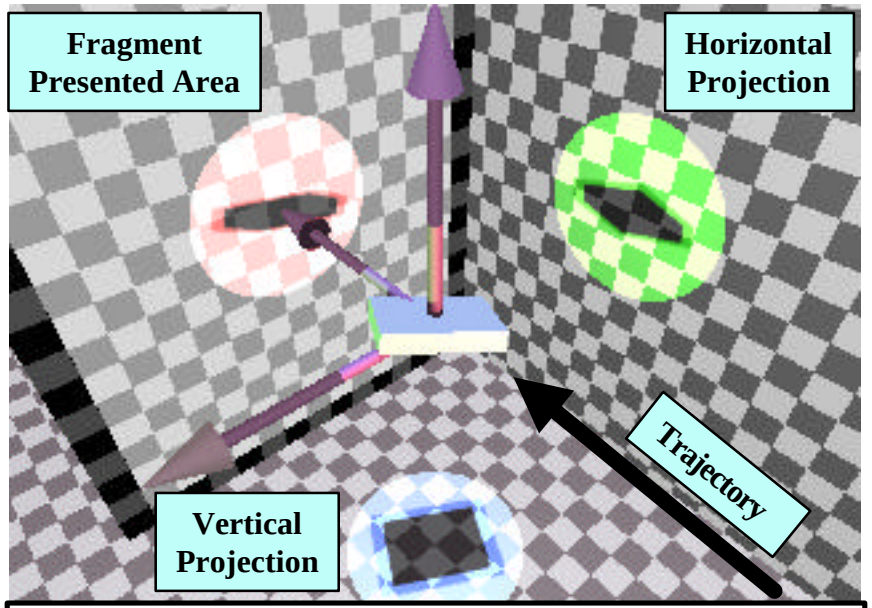

Figure C-1: Shot 2 Pre-Impact Orientation

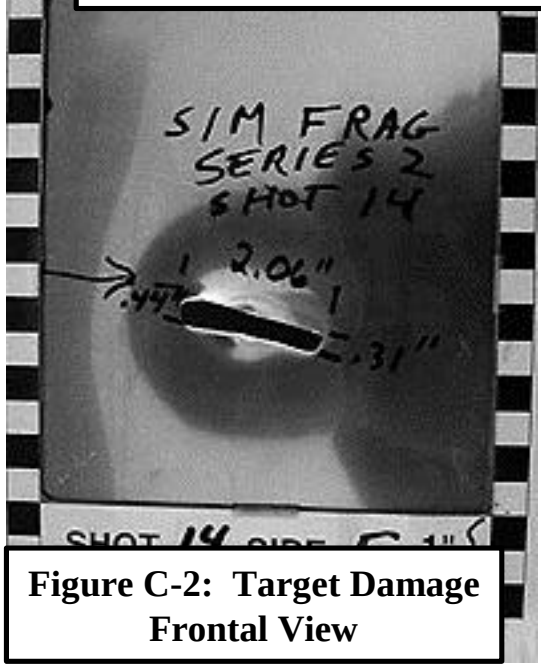

Figure C-2: Target Damage Frontal View

Figure C-3: Target Damage Rear View

Shot 31 (Series 2)

Target / Thickness
2024 T3 Aluminum / 0.05 (in.)

Simulated Fragment Material / Weight
Titanium / 25 (grams)

Length / Width / Thickness
1.4 / 1.0 / 0.25 (in.)

Pitch / Yaw / Roll
90 / 45 / -90 (degrees)

Presented Area
0.35 sq. in

Velocity Comparison
Impact / Residual / Predicted / Accuracy
339 fps / 0 fps / 296 fps / 1.87

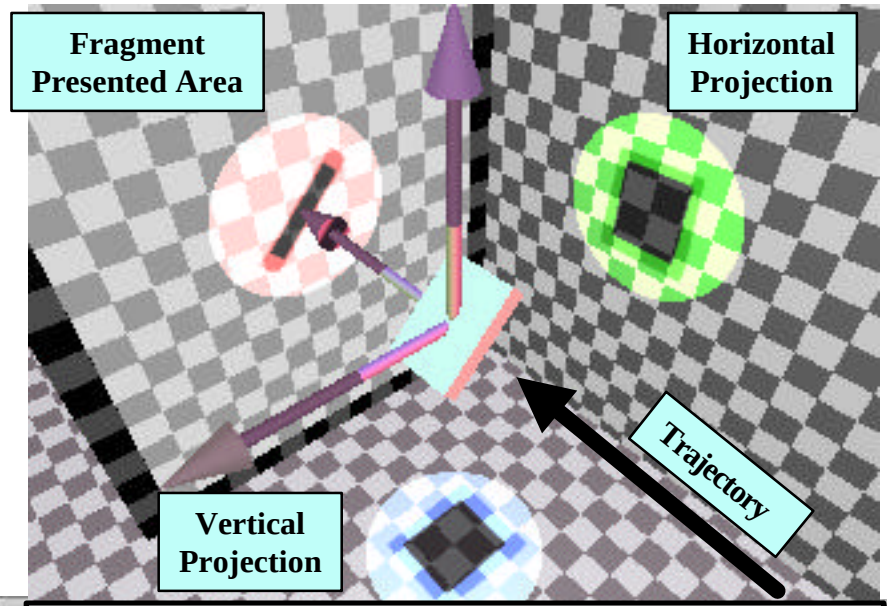

Figure C-4: Shot 31 Pre-Impact Orientation

Figure C-5: Target Damage Frontal View

Figure C-6: Target Damage Rear View

Shot 32 (Series 2)

Target / Thickness
2024 T3 Aluminum / 0.05 (in.)

Simulated Fragment Material / Weight
Titanium / 25 (grams)

Length / Width / Thickness
1.4 / 1.0 / 0.25 (in.)

Pitch / Yaw / Roll
-5 / -23 / -65 (degrees)

Presented Area
0.76 sq. in

Velocity Comparison
Impact / Residual / Predicted / Accuracy
464 fps / 380 fps / 336 fps / 0.90

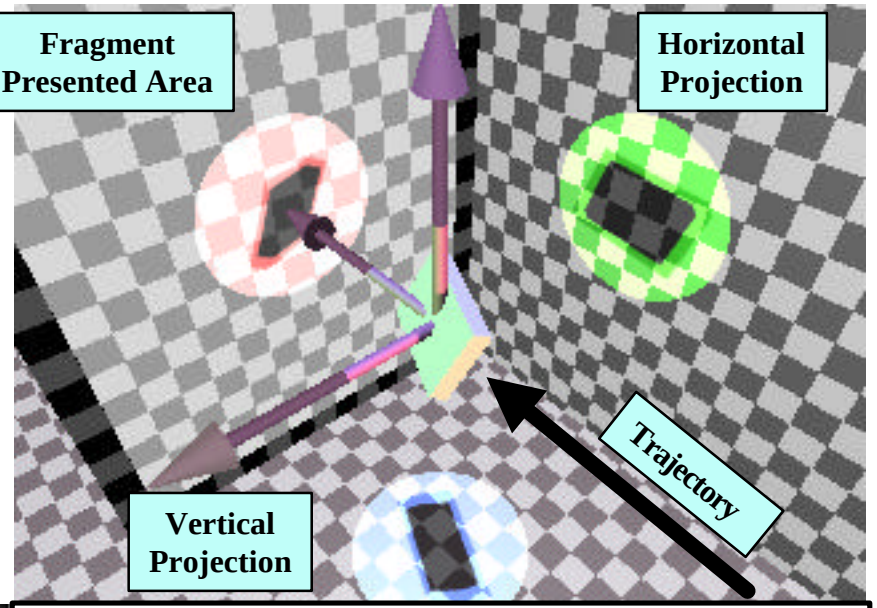

Figure C-7: Shot 32 Pre-Impact Orientation

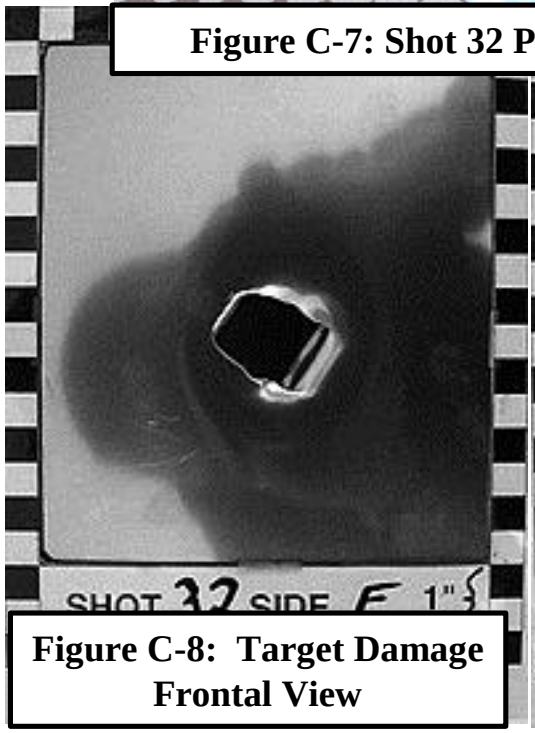

Figure C-8: Target Damage Frontal View

Figure C-9: Target Damage Rear View

Shot 33 (Series 2)

Target / Thickness
2024 T3 Aluminum / 0.05 (in.)

Simulated Fragment Material / Weight
Titanium / 25 (grams)

Length / Width / Thickness
1.4 / 1.0 / 0.25 (in.)

Pitch / Yaw / Roll
35 / -2 / -1 (degrees)

Presented Area
1.02 sq. in

Velocity Comparison
Impact / Residual / Predicted / Accuracy
416 fps / 254 fps / 147 fps / 0.74

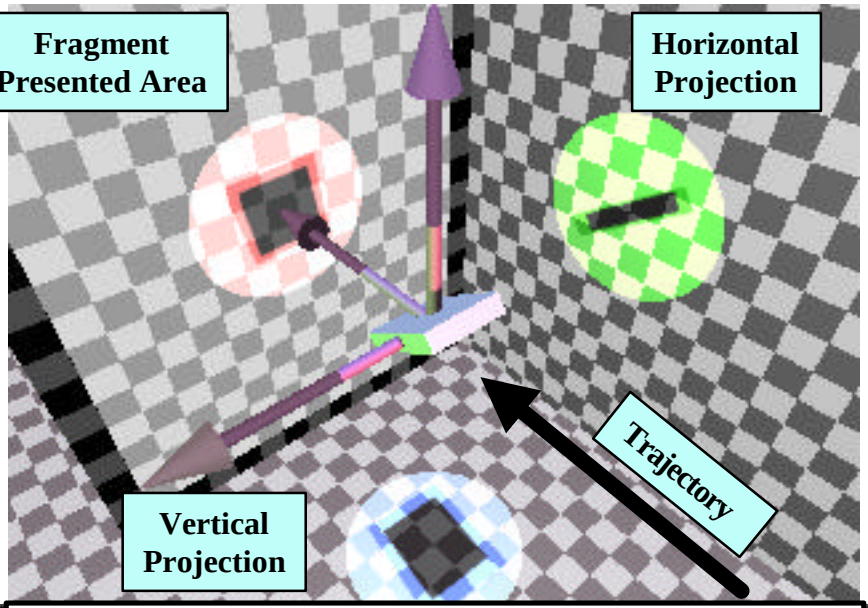

Figure C-10: Shot 33 Pre-Impact Orientation

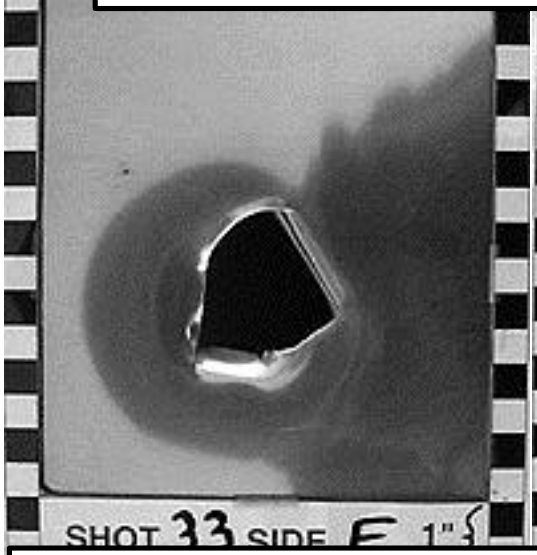

Figure C-11: Target Damage Frontal View

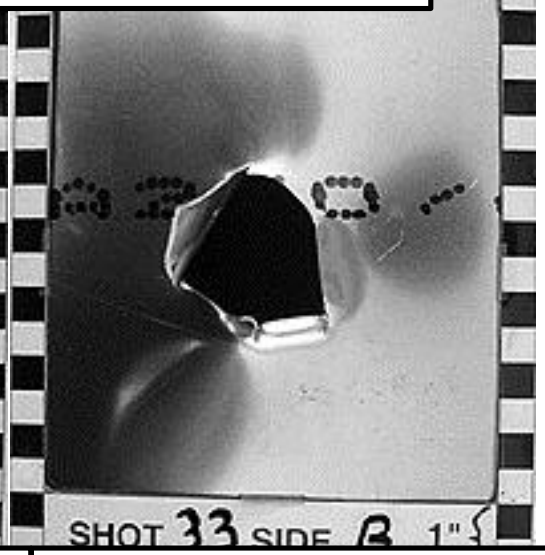

Figure C-12: Target Damage Rear View

Shot 34 (Series 2)

Target / Thickness
2024 T3 Aluminum / 0.05 (in.)

Simulated Fragment Material / Weight
Titanium / 25 (grams)

Length / Width / Thickness
1.4 / 1.0 / 0.25 (in.)

Pitch / Yaw / Roll
31 / -12 / -8 (degrees)

Presented Area
0.92 sq. in

Velocity Comparison
Impact / Residual / Predicted / Accuracy
375 fps / 259 fps / 125 fps / 0.64

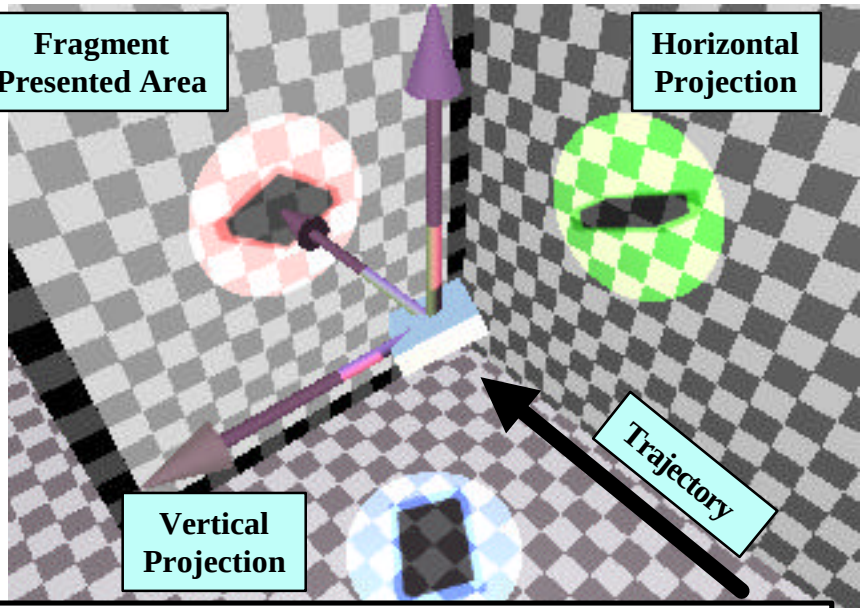

Figure C-13: Shot 34 Pre-Impact Orientation

Figure C-14: Target Damage Frontal View

Figure C-15: Target Damage Rear View

Test Series 3

Fan Blade Fragment

Impacts on

0.05" 2024 T3

Aluminum

Shot 1 (Series 3)

Target / Thickness
2024 T3 Aluminum / 0.05 (in.)

Fan Blade
Material / Weight
Titanium / 162.1 (grams)

Length / Width / Thickness
4.88 / 3.06 / 0.15 (in.)

Pitch / Yaw / Roll
-68 / 2 / -40 (degrees)

Presented Area
12.30 sq. in

Velocity Comparison
Impact / Residual / Predicted / Accuracy
483 fps / 408 fps / 0 fps / 0.16

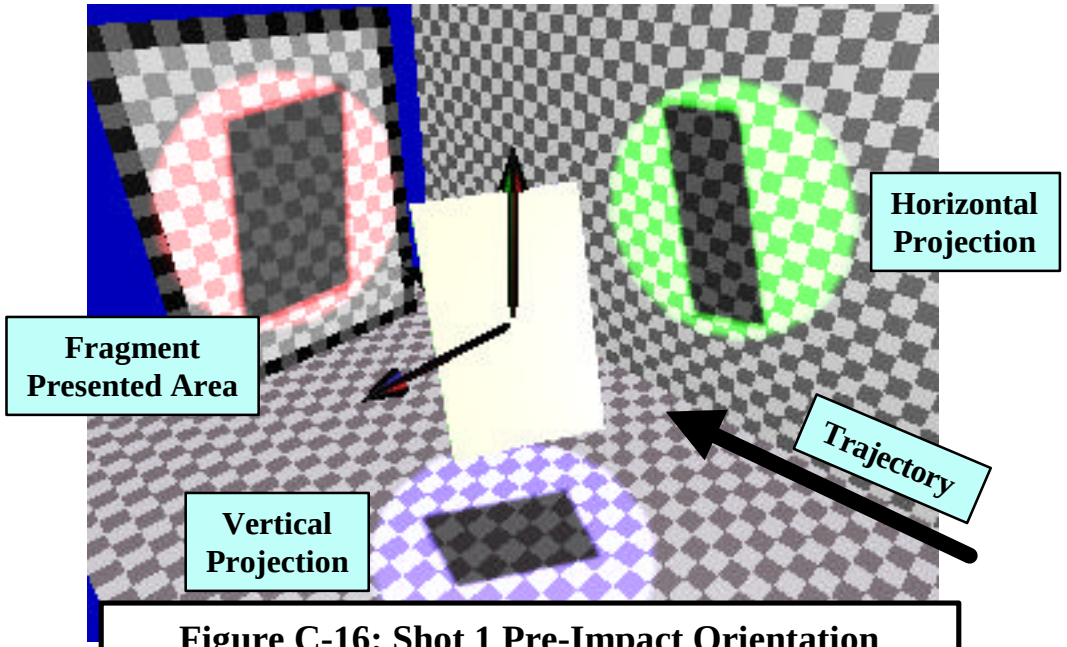

Figure C-16: Shot 1 Pre-Impact Orientation

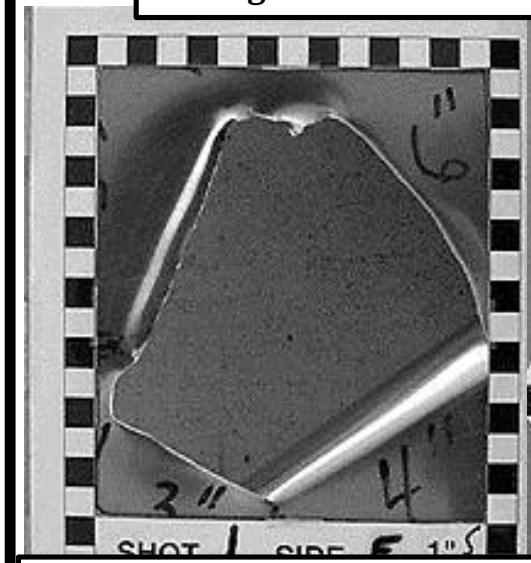

Figure C-17: Target Damage Frontal View

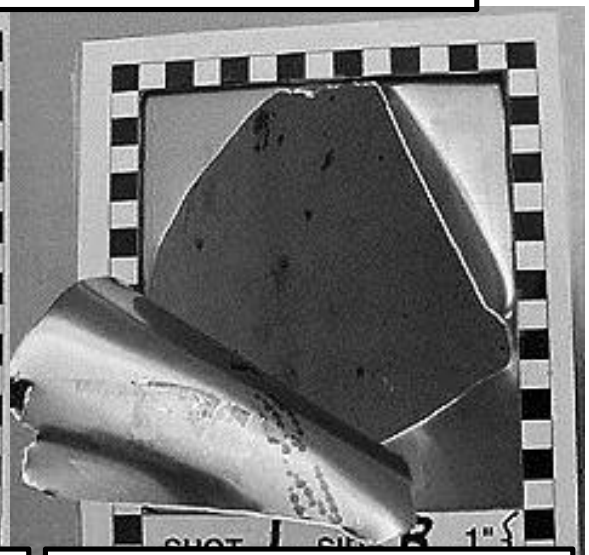

Figure C-18: Target Damage Rear View

Shot 3 (Series 3)

Target / Thickness
2024 T3 Aluminum / 0.05 (in.)

Fan Blade
Material / Weight
Titanium / 176.9 (grams)

Length / Width / Thickness
4.25 / 3.0 / 0.17 (in.)

Pitch / Yaw / Roll
75 / 0 / -82 (degrees)

Presented Area
2.57 sq. in

Velocity Comparison
Impact / Residual / Predicted / Accuracy
191 fps / 60 fps / 126 fps / 1.34

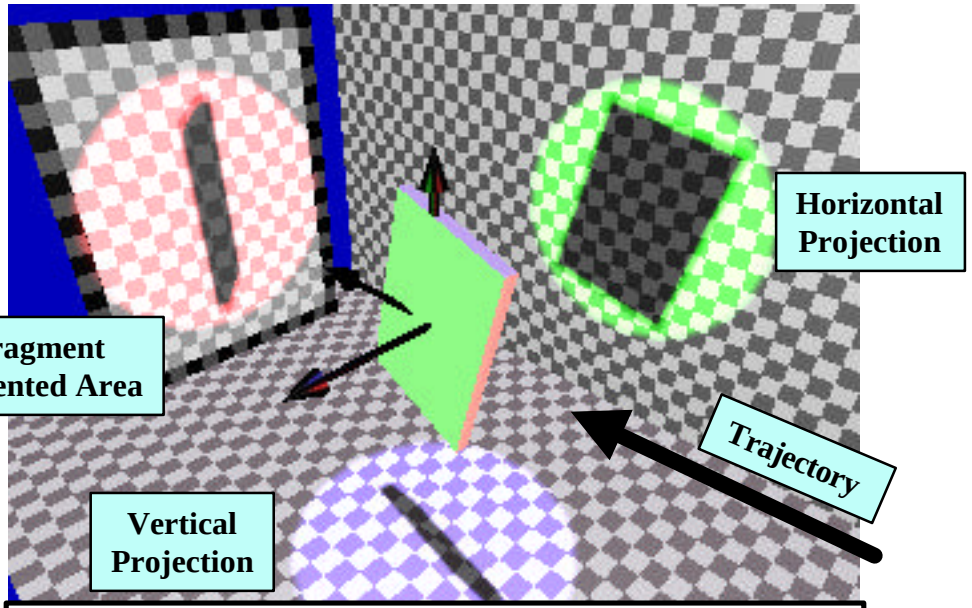

Figure C-19: Shot 3 Pre-Impact Orientation

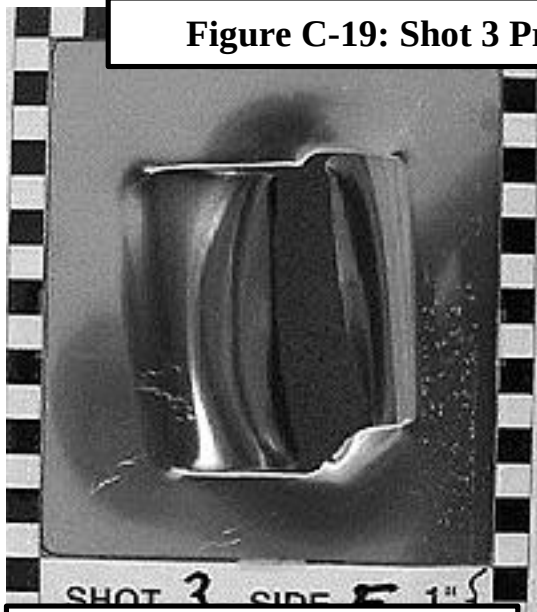

Figure C-20: Target Damage Frontal View

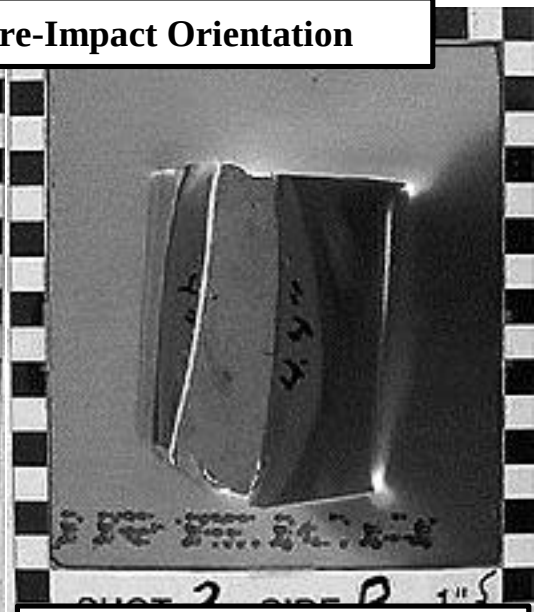

Figure C-21: Target Damage Rear View

Shot 5 (Series 3)

Target / Thickness
2024 T3 Aluminum / 0.05 (in.)

Fan Blade
Material / Weight
Titanium / 176.9 (grams)

Length / Width / Thickness
4.25 / 3.0 / 0.17 (in.)

Pitch / Yaw / Roll
-7 / -6 / 58 (degrees)

Presented Area
2.46 sq. in

Velocity Comparison
Impact / Residual / Predicted / Accuracy
150 fps / 0 fps / 64 fps /1.42

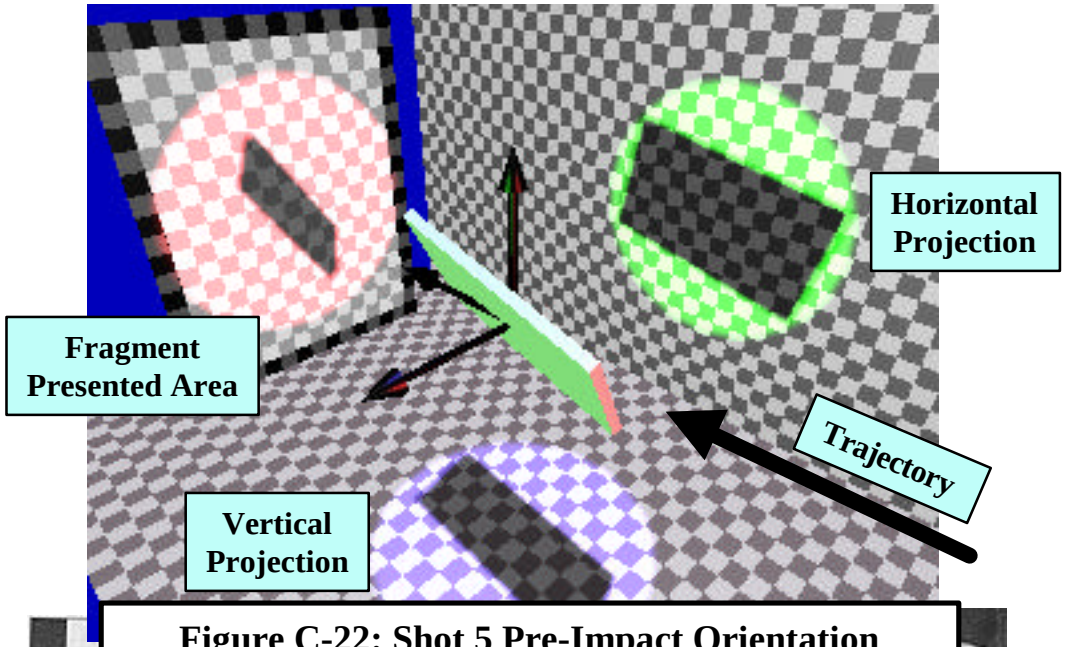

Figure C-22: Shot 5 Pre-Impact Orientation

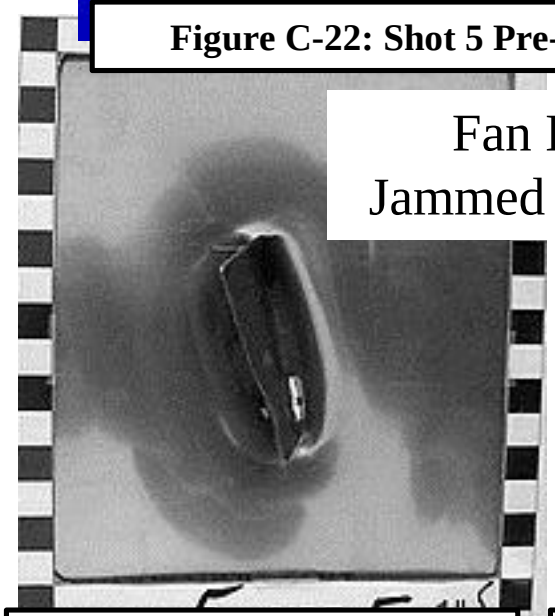

Figure C-23: Target Damage Frontal View

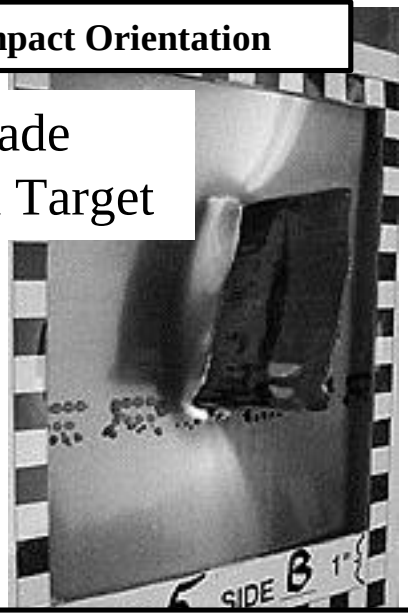

Figure C-24: Target Damage Rear View

Shot 6 (Series 3)

Target / Thickness
2024 T3 Aluminum / 0.05 (in.)

Fan Blade
Material / Weight
Titanium / 158.3 (grams)

Length / Width / Thickness
5.0 / 3.0 / 0.14 (in.)

Pitch / Yaw / Roll
-2 / -12 / -56 (degrees)

Presented Area
2.85 sq. in

Velocity Comparison
Impact / Residual / Predicted / Accuracy
225 fps / 150 fps / 141 fps / 0.96

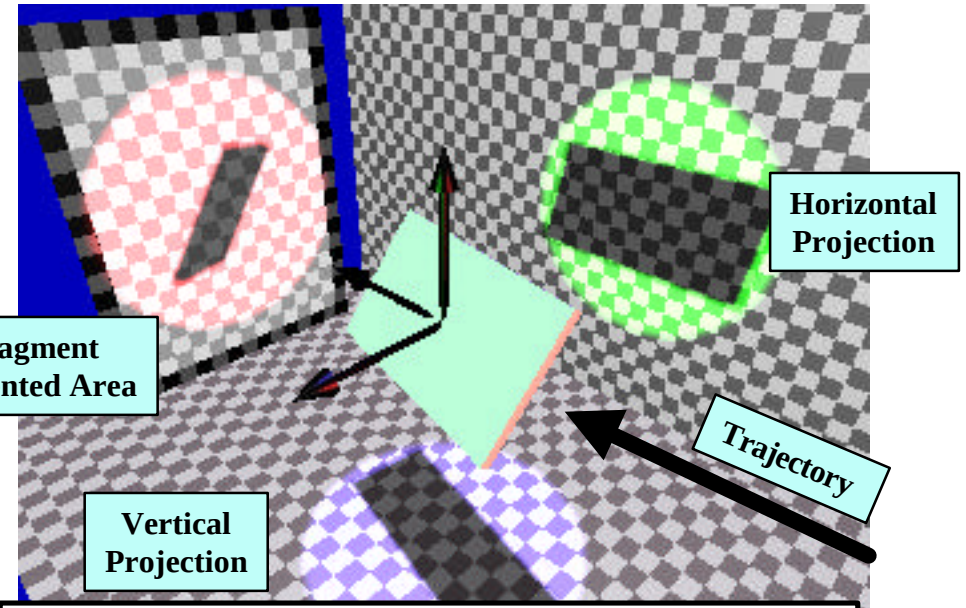

Figure C-25: Shot 6 Pre-Impact Orientation

Figure C-26: Target Damage Frontal View

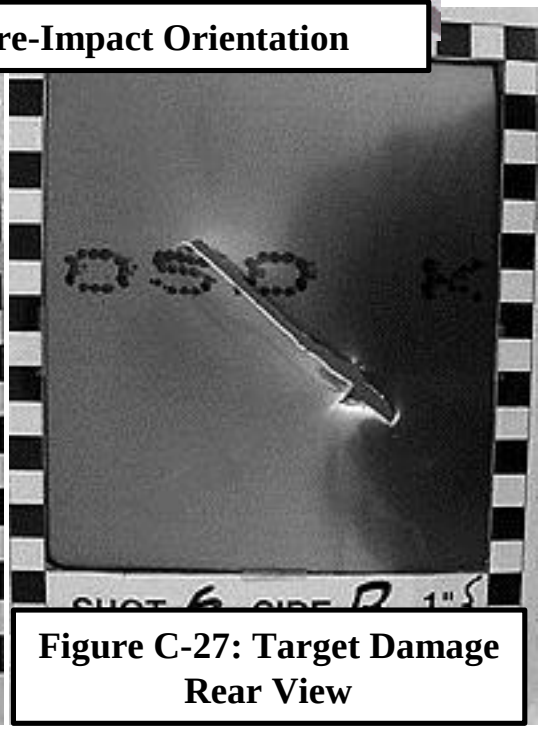

Figure C-27: Target Damage Rear View

Shot 7 (Series 3)

Target / Thickness
2024 T3 Aluminum / 0.05 (in.)

Fan Blade
Material / Weight
Titanium / 151.9 (grams)

Length / Width / Thickness
5.0 / 2.81 / 0.15 (in.)

Pitch / Yaw / Roll
41 / -72 / -20 (degrees)

Presented Area
12.57 sq. in

Velocity Comparison
Impact / Residual / Predicted / Accuracy
241 fps / 4 fps / 0 fps / 0.98

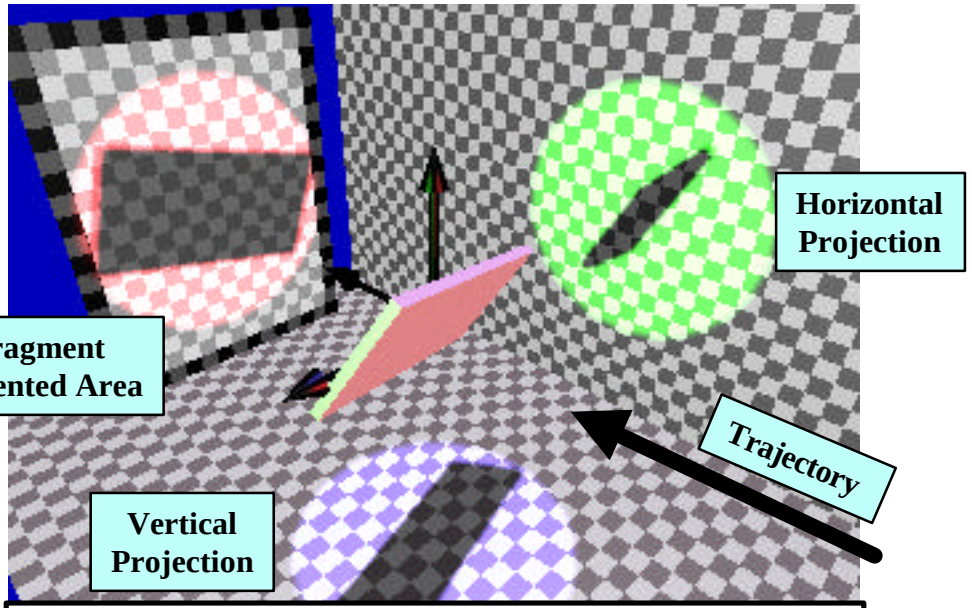

Figure C-28: Shot 7 Pre-Impact Orientation

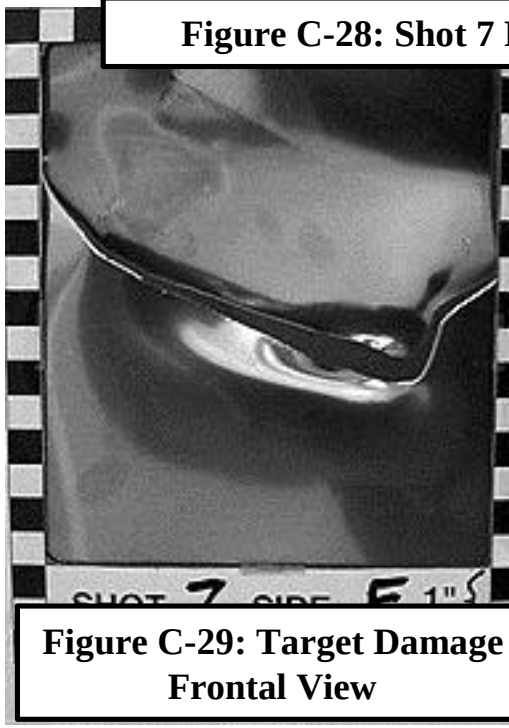

Figure C-29: Target Damage Frontal View

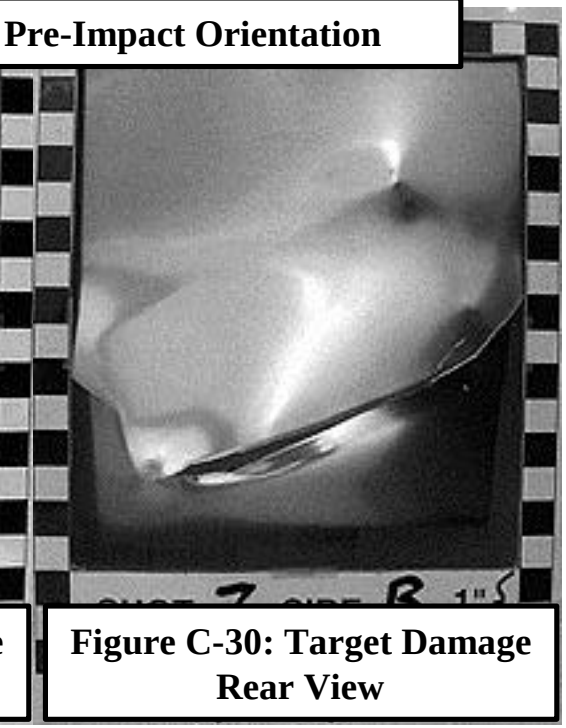

Figure C-30: Target Damage Rear View

Shot 8 (Series 3)

Target / Thickness
2024 T3 Aluminum / 0.05 (in.)

Fan Blade
Material / Weight
Titanium / 153.4 (grams)

Length / Width / Thickness
5.0 / 3.0 / 0.14 (in.)

Pitch / Yaw / Roll
8 / 6 / -46 (degrees)

Presented Area
0.94 sq. in

Velocity Comparison
Impact / Residual / Predicted / Accuracy
245 fps / 183 fps / 233 fps / 1.20

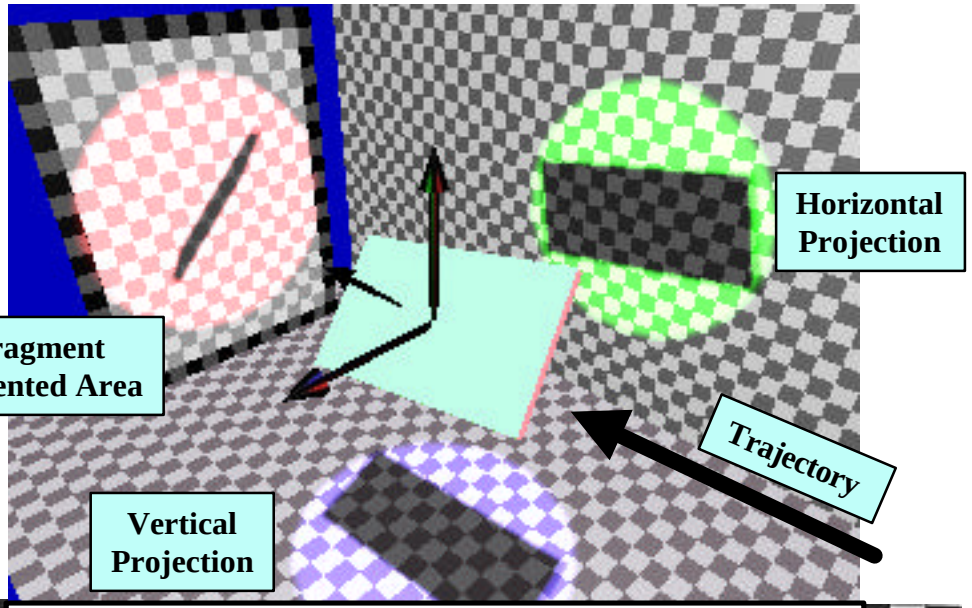

Figure C-31: Shot 8 Pre-Impact Orientation

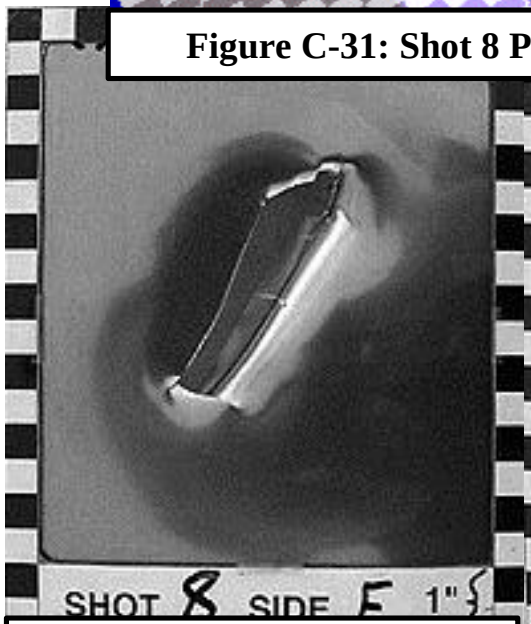

Figure C-32: Target Damage Frontal View

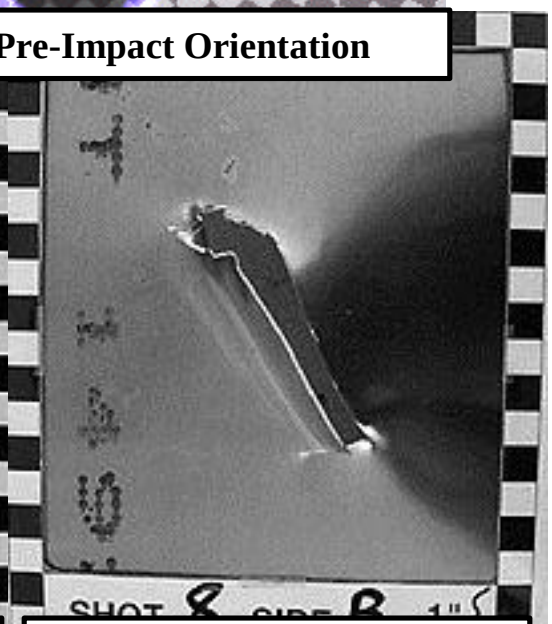

Figure C-33: Target Damage Rear View

Shot 9 (Series 3)

Target / Thickness
2024 T3 Aluminum / 0.05 (in.)

Fan Blade
Material / Weight
Titanium / 151.9 (grams)

Length / Width / Thickness
5.0 / 2.81 / 0.15 (in.)

Pitch / Yaw / Roll
-59 / 24 / -81 (degrees)

Presented Area
5.24 sq. in

Velocity Comparison
Impact / Residual / Predicted / Accuracy
290 fps / 188 fps / 0 fps / 0.35

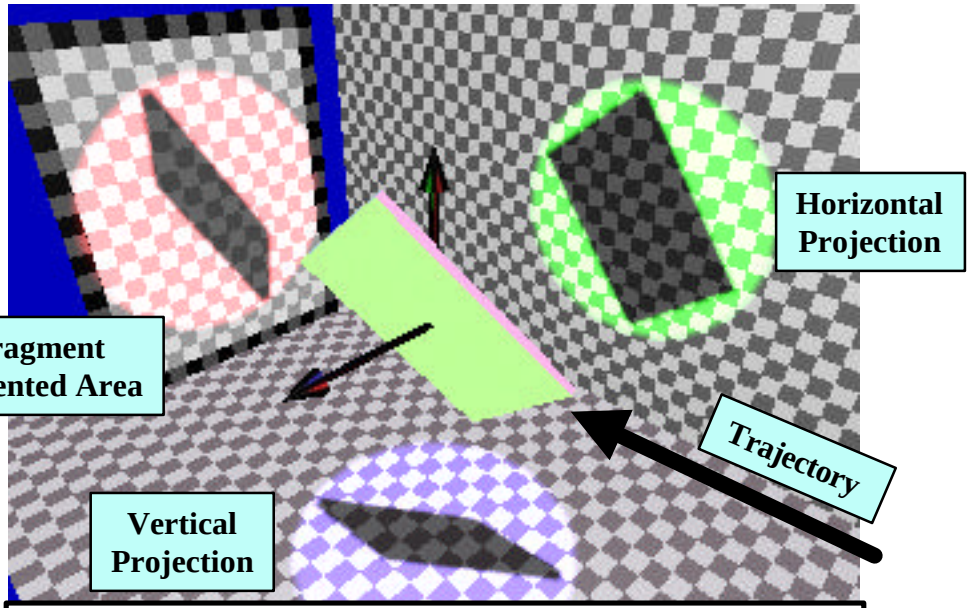

Figure C-34: Shot 9 Pre-Impact Orientation

Figure C-35: Target Damage Frontal View

Figure C-36: Target Damage Rear View

Shot 10 (Series 3)

Target / Thickness
2024 T3 Aluminum / 0.05 (in.)

Fan Blade
Material / Weight
Titanium / 159.7 (grams)

Length / Width / Thickness
5.0 / 3.0 / 0.15 (in.)

Pitch / Yaw / Roll
-47 / 11 / 63 (degrees)

Presented Area
4.00 sq. in

Velocity Comparison
Impact / Residual / Predicted / Accuracy
321 fps / 233 fps / 212 fps / 0.93

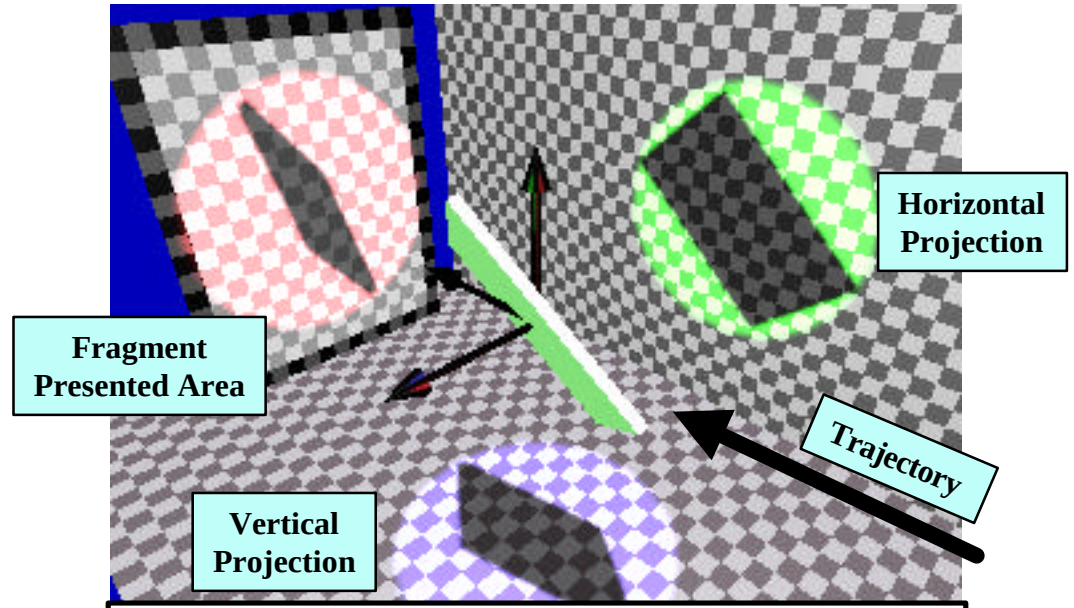

Figure C-37: Shot 10 Pre-Impact Orientation

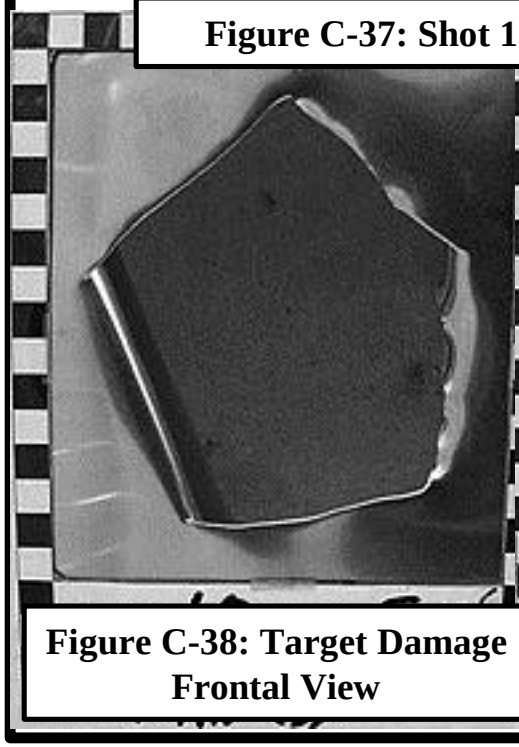

Figure C-38: Target Damage Frontal View

Figure C-39: Target Damage Rear View

Shot 17 (Series 3)

Target / Thickness
2024 T3 Aluminum / 0.05 (in.)

Fan Blade
Material / Weight
Titanium / 159.7 (grams)

Length / Width / Thickness
5.0 / 3.0 / 0.15 (in.)

Pitch / Yaw / Roll
71 / 17 / -48 (degrees)

Presented Area
8.35 sq. in

Velocity Comparison
Impact / Residual / Predicted / Accuracy
530 fps / 451 fps / 254 fps / 0.63

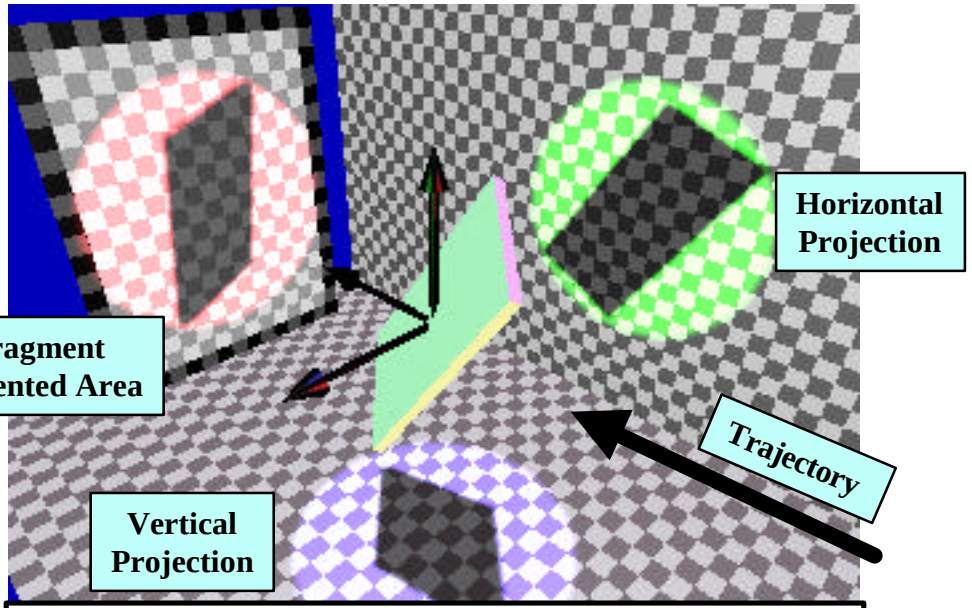

Figure C-40: Shot 17 Pre-Impact Orientation

Figure C-41: Target Damage Frontal View

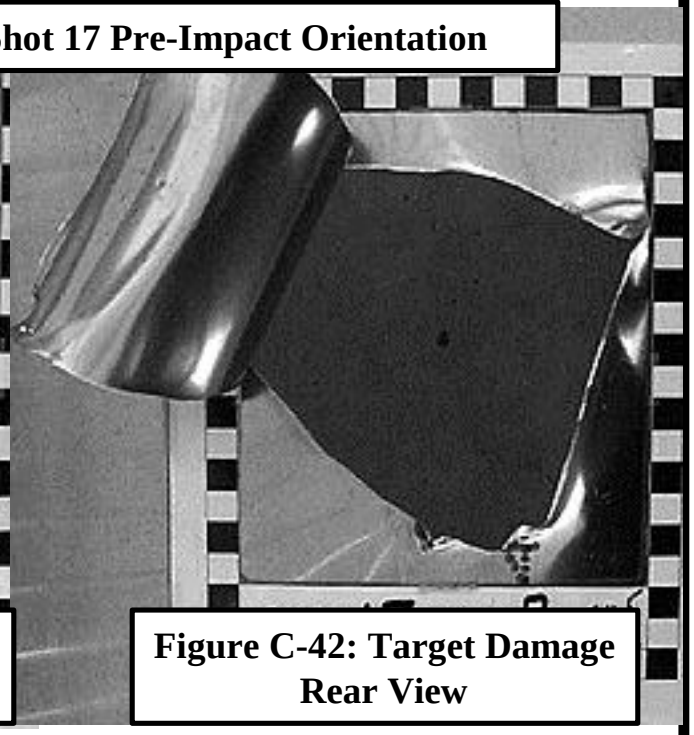

Figure C-42: Target Damage Rear View

Shot 18 (Series 3)

Target / Thickness
2024 T3 Aluminum / 0.05 (in.)

Fan Blade
Material / Weight
Titanium / 145.1 (grams)

Length / Width / Thickness
5.0 / 3.0 / 0.13 (in.)

Pitch / Yaw / Roll
44 / 25 / -84 (degrees)

Presented Area
4.35 sq. in

Velocity Comparison
Impact / Residual / Predicted / Accuracy
567 fps / 272 fps / 466 fps / 0.87

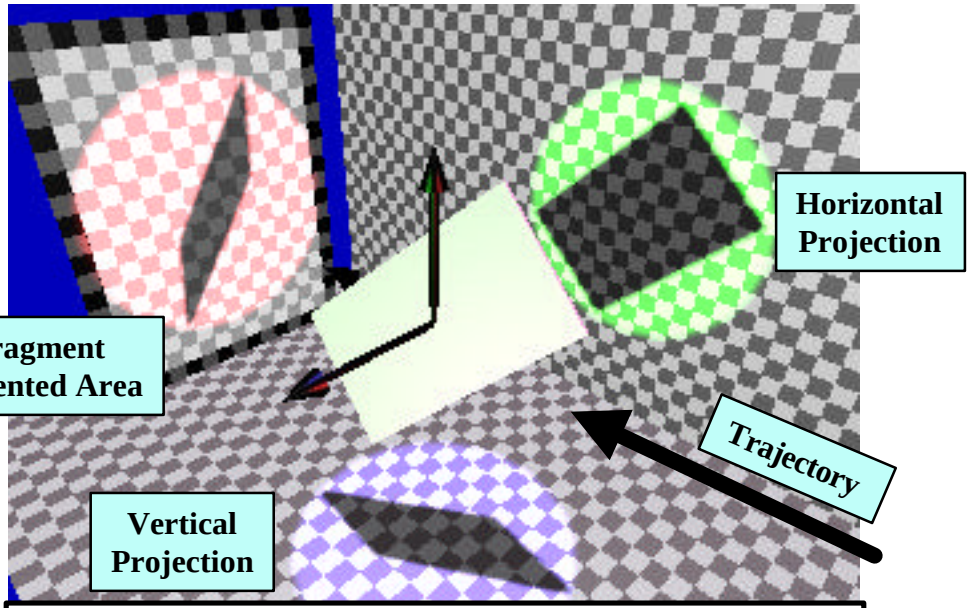

Figure C-43: Shot 18 Pre-Impact Orientation

Figure C-44: Target Damage Frontal View

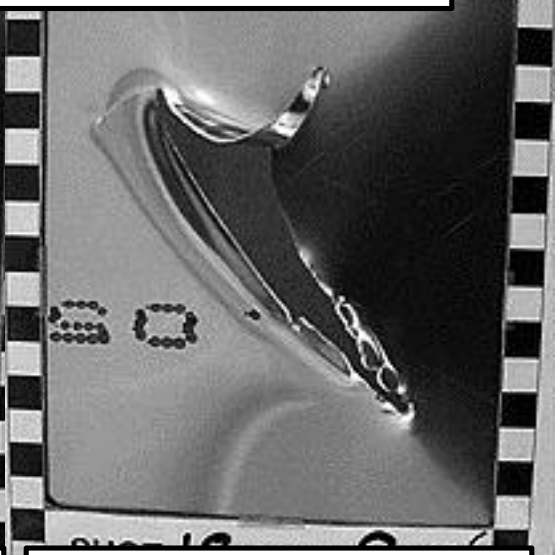

Figure C-45: Target Damage Rear View

Test Series 4

Fan Blade Fragment

Impacts on

0.071" 2024 T3

Aluminum

Shot 11 (Series 4)

Target / Thickness
2024 T3 Aluminum / 0.071 (in.)

Fan Blade
Material / Weight
Titanium / 158.3 (grams)

Length / Width / Thickness
5.0 / 3.0 / 0.15 (in.)

Pitch / Yaw / Roll
-61 / 0 / -18 (degrees)

Presented Area
12.82 sq. in

Velocity Comparison
Impact / Residual / Predicted / Accuracy
196 fps / 0 fps / 0 fps / 1.0

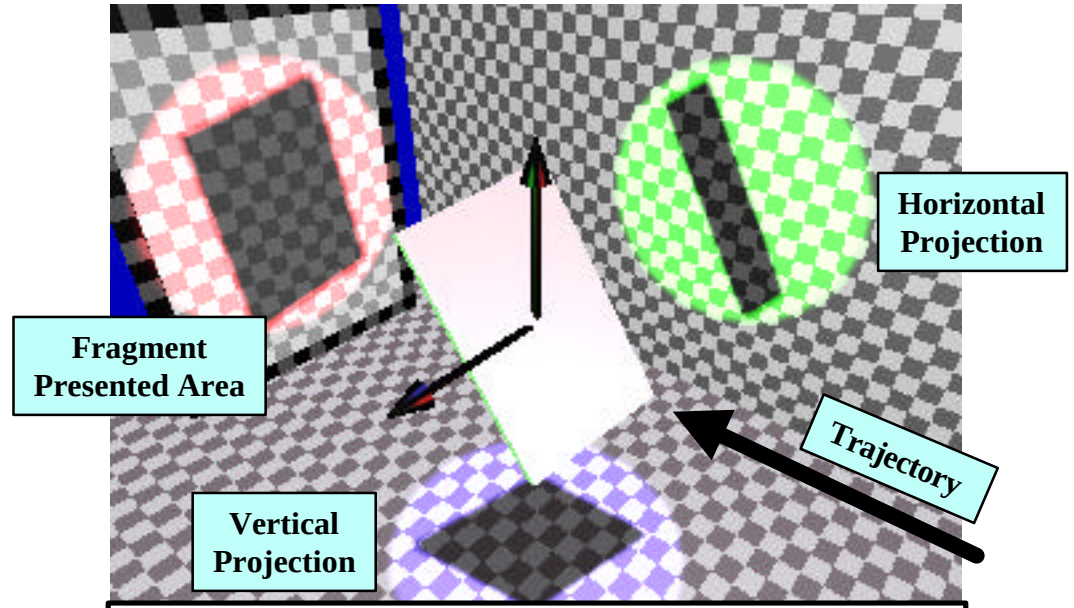

Figure C-46: Shot 11 Pre-Impact Orientation

Figure C-47: Target Damage Frontal View

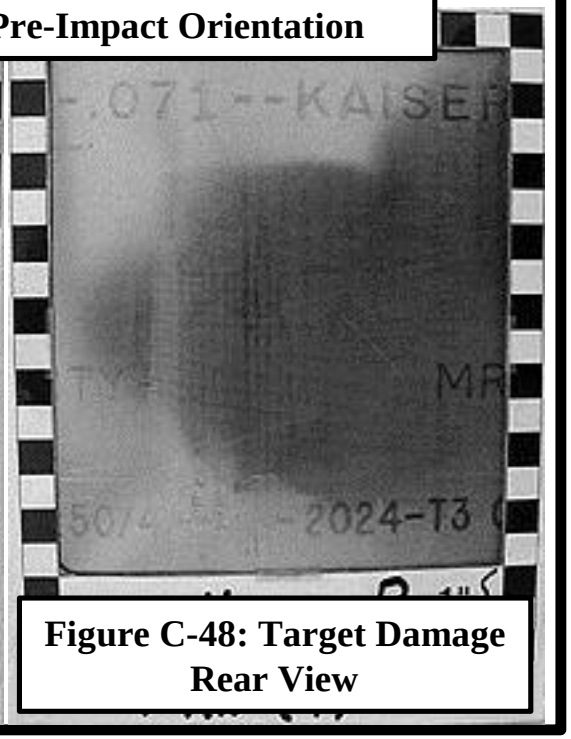

Figure C-48: Target Damage Rear View

Shot 12 (Series 4)

Target / Thickness
2024 T3 Aluminum / 0.071 (in.)

Fan Blade
Material / Weight
Titanium / 158.3 (grams)

Length / Width / Thickness
5.0 / 3.0 / 0.15 (in.)

Pitch / Yaw / Roll
-51 / 36 / 45 (degrees)

Presented Area
5.17 sq. in

Velocity Comparison
Impact / Residual / Predicted / Accuracy
411 fps / 275 fps / 79 fps / 0.52

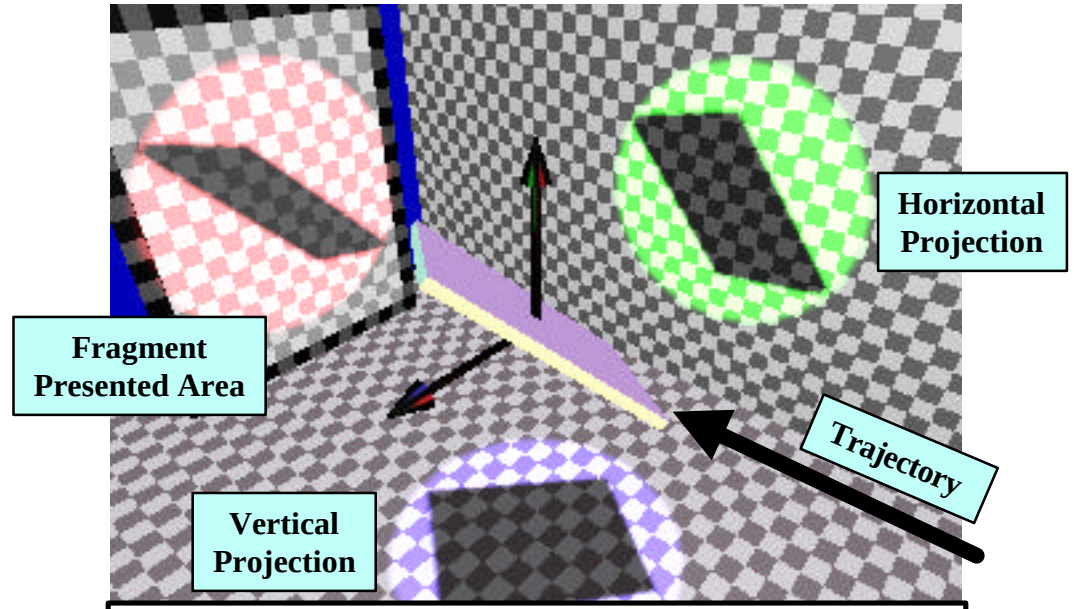

Figure C-49: Shot 12 Pre-Impact Orientation

Figure C-50: Target Damage Frontal View

Figure C-51: Target Damage Rear View

Shot 13 (Series 4)

Target / Thickness
2024 T3 Aluminum / 0.071 (in.)

Fan Blade
Material / Weight
Titanium / 151.9 (grams)

Length / Width / Thickness
5.0 / 2.8 / 0.15 (in.)

Pitch / Yaw / Roll
-33 / -26 / -75 (degrees)

Presented Area
3.92 sq. in

Velocity Comparison
Impact / Residual / Predicted / Accuracy
458 fps / 349 fps / 298 fps / 0.89

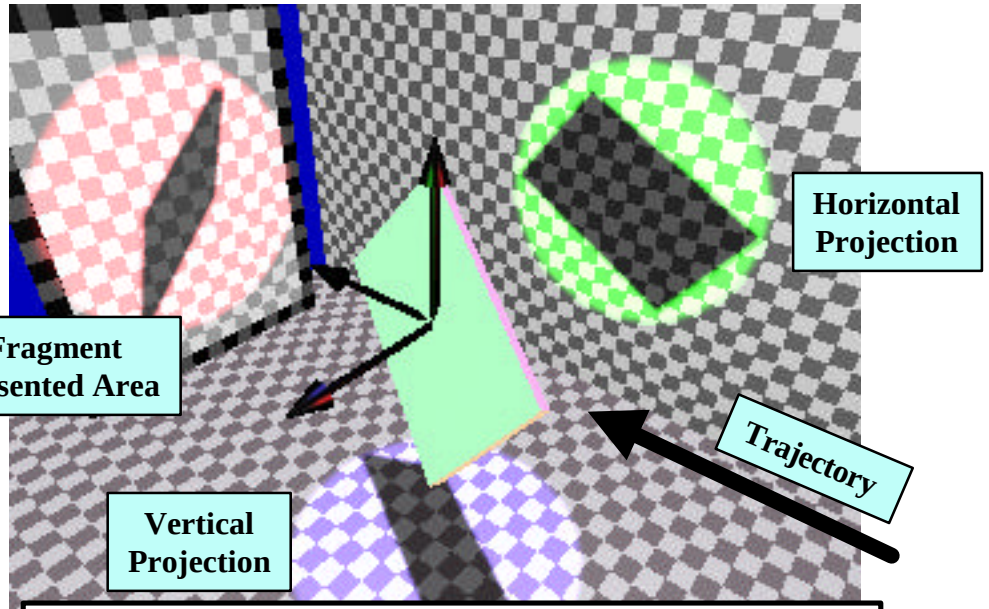

Figure C-52: Shot 13 Pre-Impact Orientation

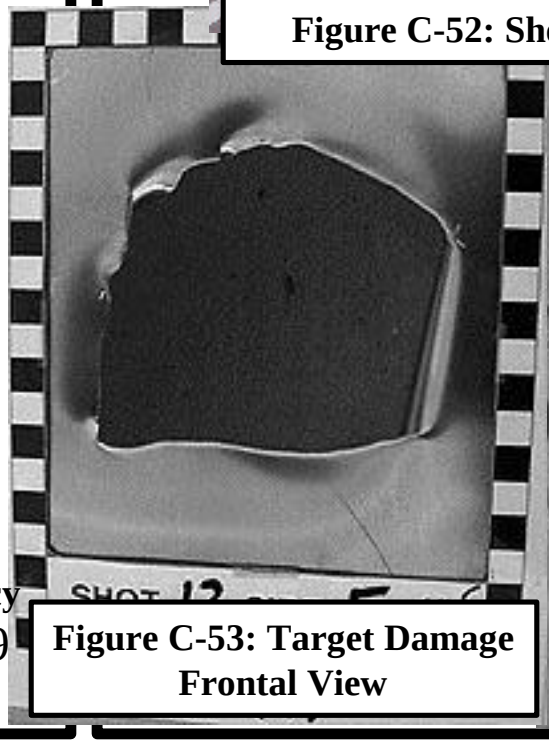

Figure C-53: Target Damage Frontal View

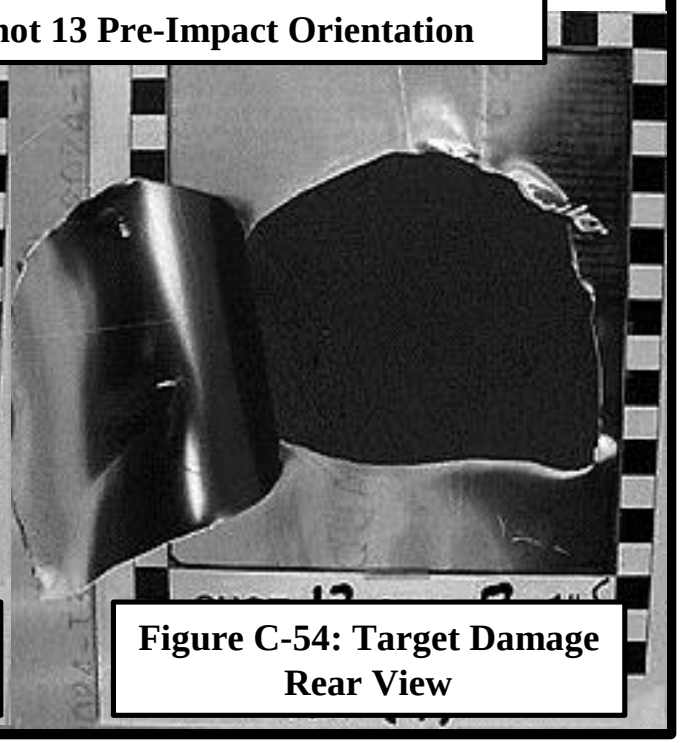

Figure C-54: Target Damage Rear View

Shot 19 (Series 4)

Target / Thickness
2024 T3 Aluminum / 0.071 (in.)

Fan Blade
Material / Weight
Titanium / 174.6 (grams)

Length / Width / Thickness
4.2 / 3.0 / 0.19 (in.)

Pitch / Yaw / Roll
33 / -8 / -32 (degrees)

Presented Area
7.17 sq. in

Velocity Comparison
Impact / Residual / Predicted / Accuracy
629 fps / 530 fps / 346 fps / 0.71

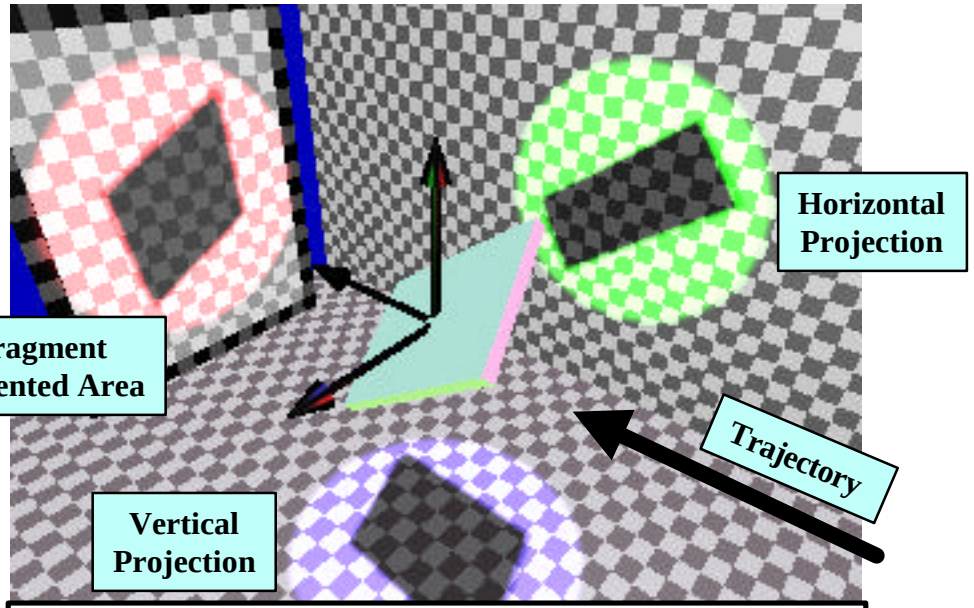

Figure C-55: Shot 19 Pre-Impact Orientation

Figure C-56: Target Damage Frontal View

Figure C-57: Target Damage Rear View

Shot 20 (Series 4)

Target / Thickness
2024 T3 Aluminum / 0.071 (in.)

Fan Blade
Material / Weight
Titanium / 183.7 (grams)

Length / Width / Thickness
4.4 / 3.0 / 0.19 (in.)

Pitch / Yaw / Roll
-40 / 46 / 40 (degrees)

Presented Area
2.69 sq. in

Velocity Comparison
Impact / Residual / Predicted / Accuracy
484 fps / 414 fps / 424 fps / 1.02

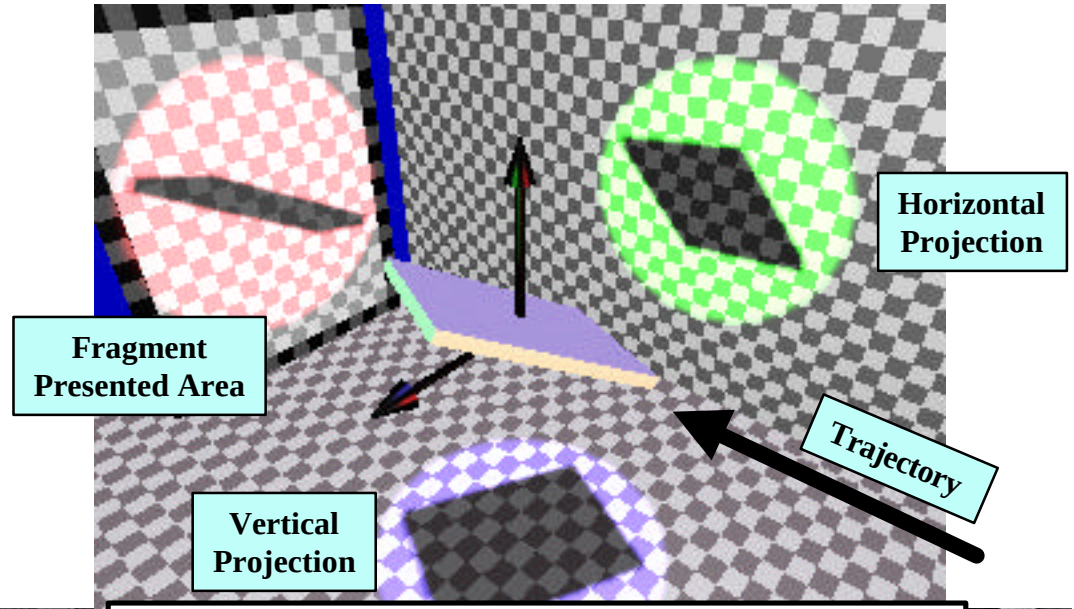

Figure C-58: Shot 20 Pre-Impact Orientation

Figure C-59: Target Damage Frontal View

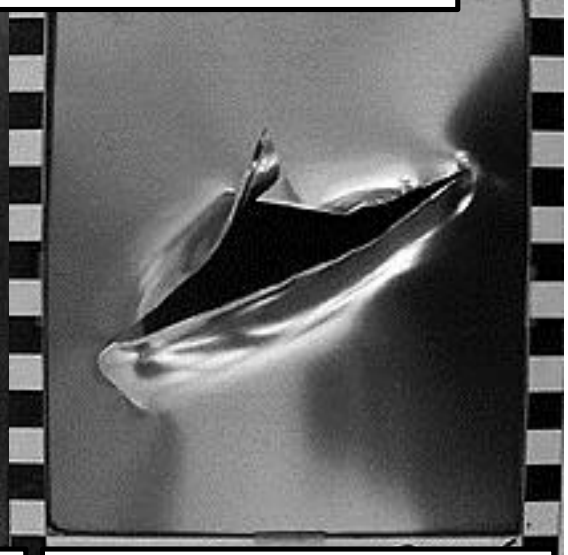

Figure C-60: Target Damage Rear View

Shot 21 (Series 4)

Target / Thickness
2024 T3 Aluminum / 0.071 (in.)

Fan Blade
Material / Weight
Titanium / 189.5 (grams)

Length / Width / Thickness
4.2 / 3.0 / 0.21 (in.)

Pitch / Yaw / Roll
-50 / -79 / -72 (degrees)

Presented Area
5.67 sq. in

Velocity Comparison
Impact / Residual / Predicted / Accuracy
396 fps / 323 fps / 132 fps / 0.52

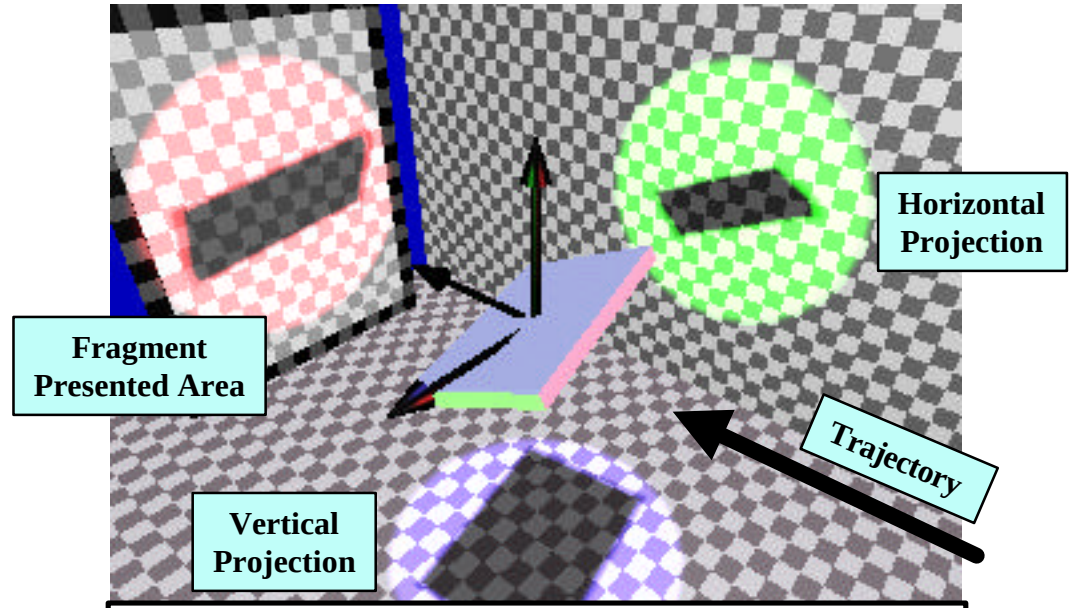

Figure C-61: Shot 21 Pre-Impact Orientation

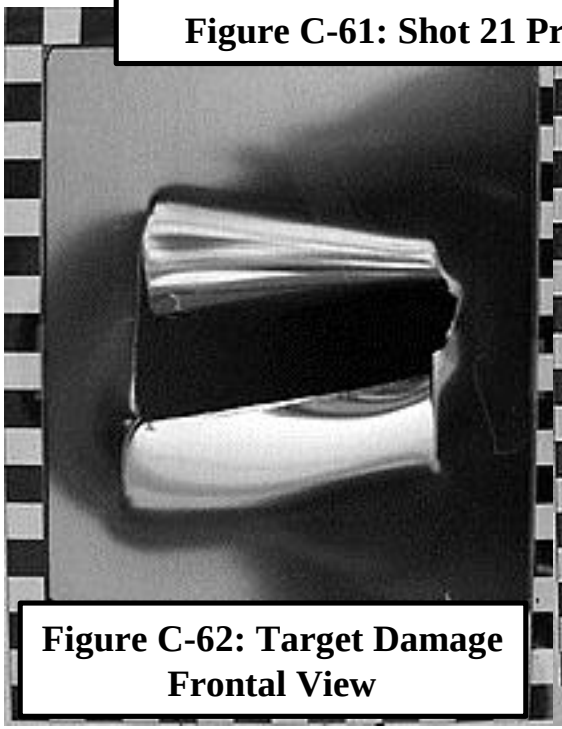

Figure C-62: Target Damage Frontal View

Figure C-63: Target Damage Rear View

Shot 22 (Series 4)

Target / Thickness
2024 T3 Aluminum / 0.071 (in.)

Fan Blade
Material / Weight
Titanium / 183.7 (grams)

Length / Width / Thickness
4.4 / 3.0 / 0.19 (in.)

Pitch / Yaw / Roll
62 / 30 / 1 (degrees)

Presented Area
12.09 sq. in

Velocity Comparison
Impact / Residual / Predicted / Accuracy
338 fps / 0 fps / 0 fps / 1.00

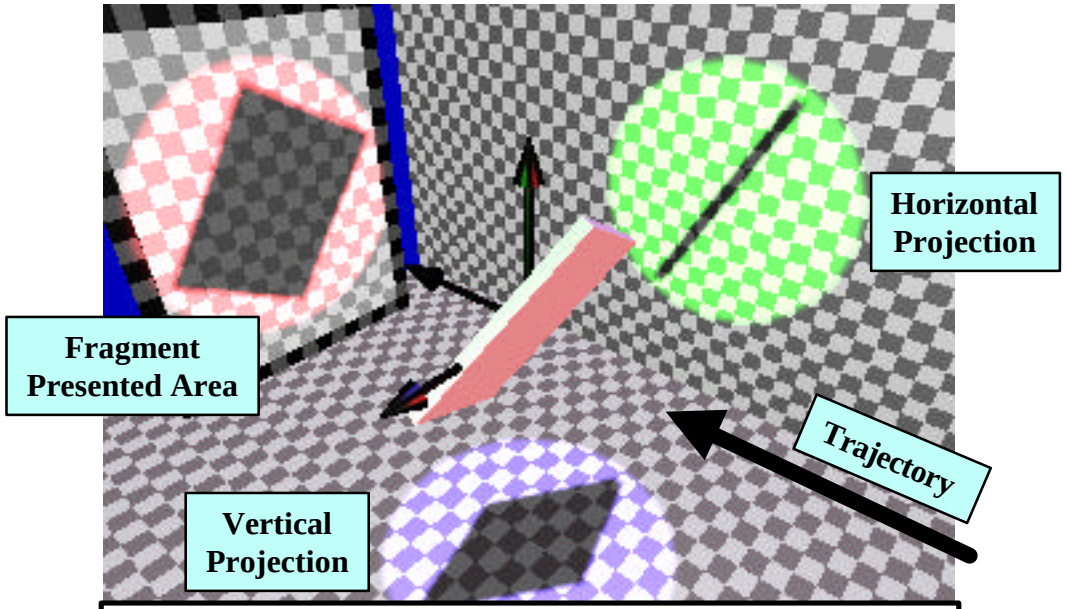

Figure C-64: Shot 22 Pre-Impact Orientation

Figure C-65: Target Damage Frontal View

Figure C-66: Target Damage Rear View

Shot 23 (Series 4)

Target / Thickness
2024 T3 Aluminum / 0.071 (in.)

Fan Blade Material / Weight
Titanium / 201.3 (grams)

Length / Width / Thickness
4.0 / 3.0 / 0.23 (in.)

Pitch / Yaw / Roll
-44 / 85 / 76 (degrees)

Presented Area
7.26 sq. in

Velocity Comparison
Impact / Residual / Predicted / Accuracy
210 fps / 0 fps / 0 fps / 1.00

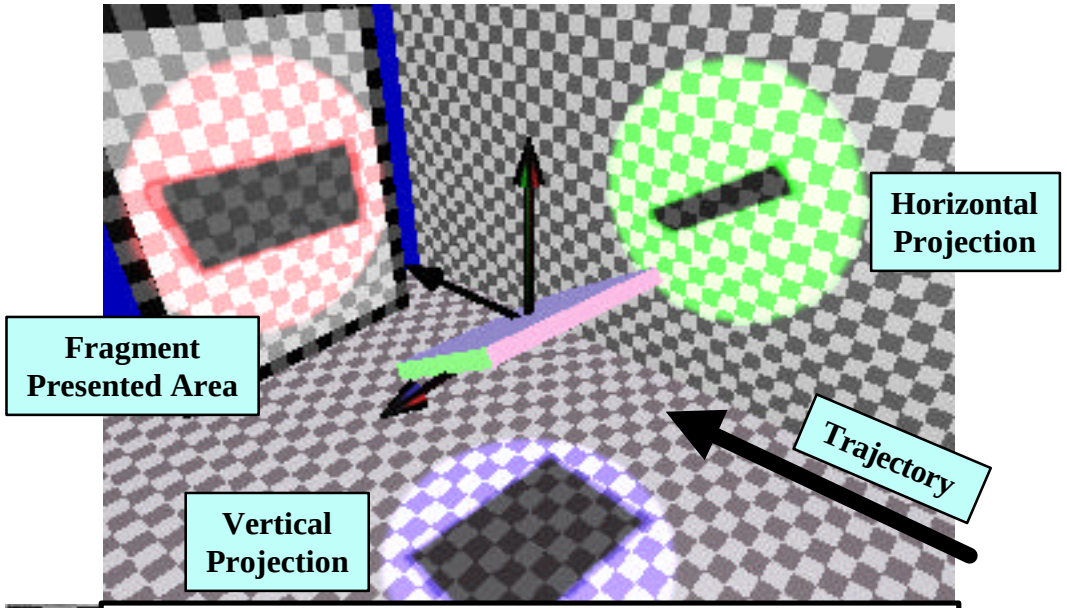

Figure C-67: Shot 23 Pre-Impact Orientation

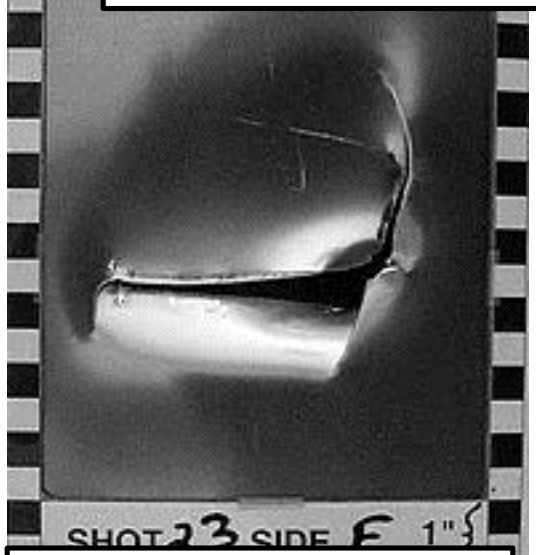

Figure C-68: Target Damage Frontal View

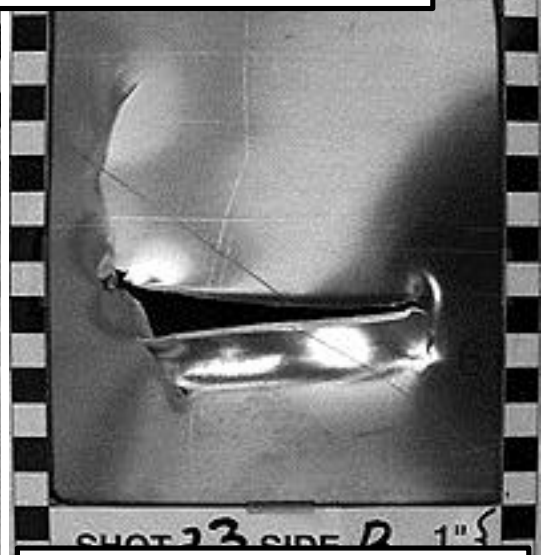

Figure C-69: Target Damage Rear View

Shot 26 (Series 4)

Target / Thickness
2024 T3 Aluminum / 0.071 (in.)

Fan Blade
Material / Weight
Titanium / 183.7 (grams)

Length / Width / Thickness
4.4 / 3.0 / 0.19 (in.)

Pitch / Yaw / Roll
25 / -46 / 18 (degrees)

Presented Area
3.53 sq. in

Velocity Comparison
Impact / Residual / Predicted / Accuracy
328 fps / 242 fps / 203 fps / 0.88

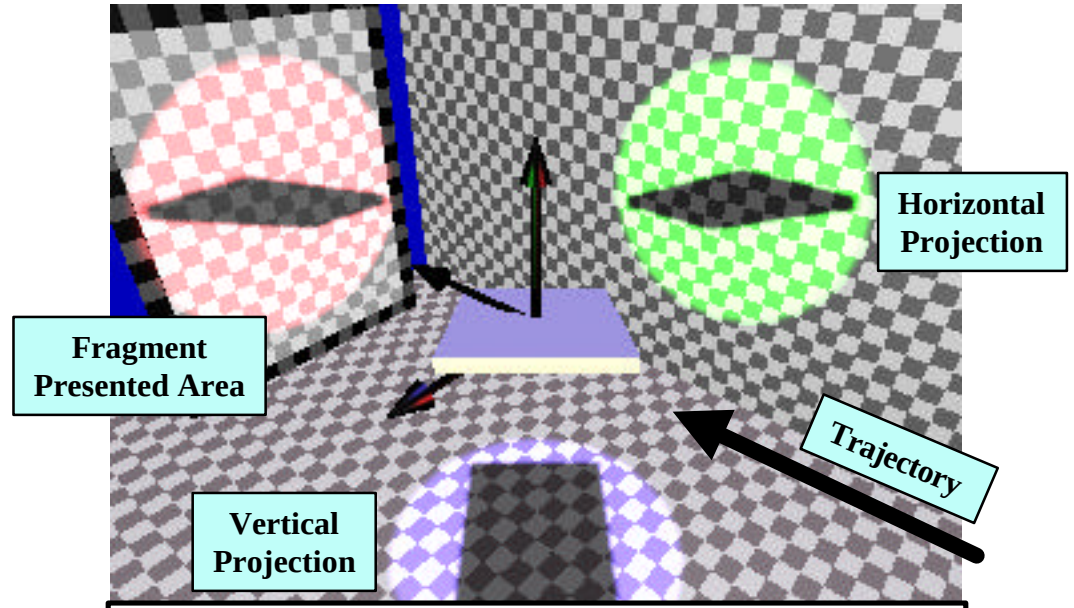

Figure C-70: Shot 26 Pre-Impact Orientation

Figure C-71: Target Damage Frontal View

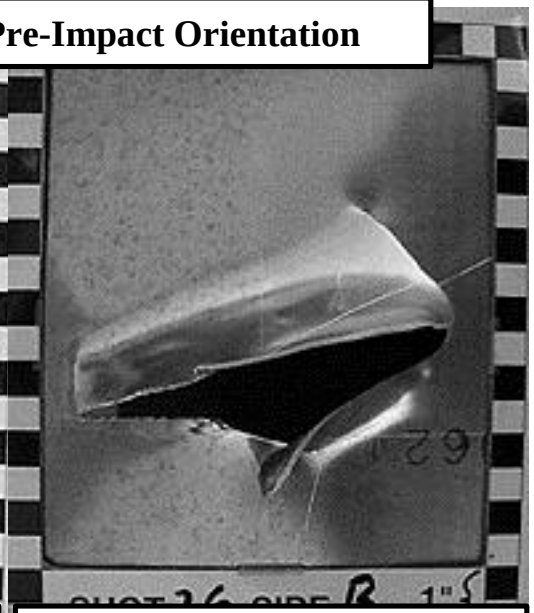

Figure C-72: Target Damage Rear View

Shot 27 (Series 4)

Target / Thickness
2024 T3 Aluminum / 0.071 (in.)

Fan Blade
Material / Weight
Titanium / 201.3 (grams)

Length / Width / Thickness
4.0 / 3.0 / 0.23 (in.)

Pitch / Yaw / Roll
-13 / 22 / -38 (degrees)

Presented Area
5.56 sq. in

Velocity Comparison
Impact / Residual / Predicted / Accuracy
281 fps / 176 fps / 0 fps / 0.37

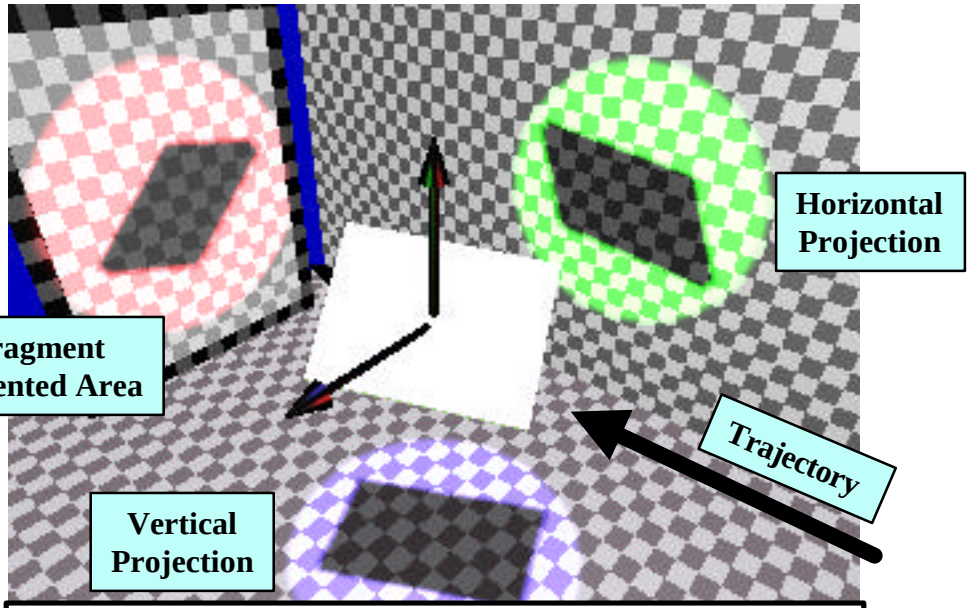

Figure C-73: Shot 27 Pre-Impact Orientation

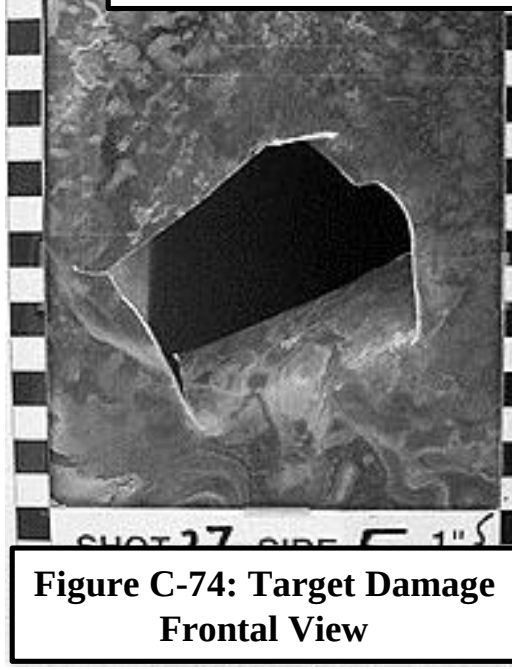

Figure C-74: Target Damage Frontal View

Figure C-75: Target Damage Rear View

Shot 28 (Series 4)

Target / Thickness
2024 T3 Aluminum / 0.071 (in.)

Fan Blade
Material / Weight
Titanium / 189.5 (grams)

Length / Width / Thickness
4.2 / 3.0 / 0.21 (in.)

Pitch / Yaw / Roll
-25 / -2 / -49 (degrees)

Presented Area
4.02 sq. in

Velocity Comparison
Impact / Residual / Predicted / Accuracy
265 fps / 137 fps / 0 fps / 0.48

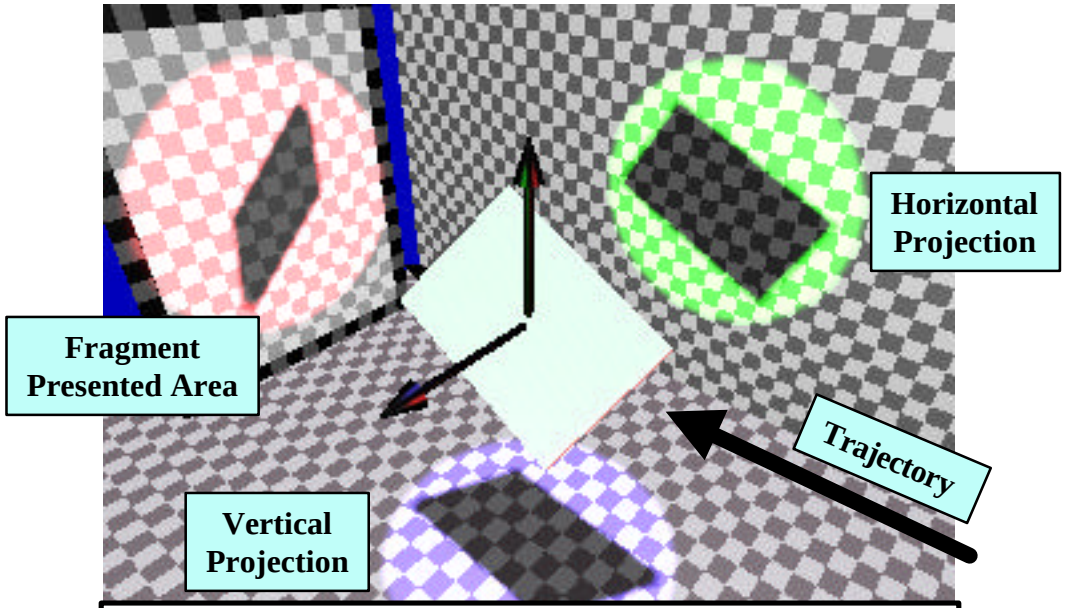

Figure C-76: Shot 28 Pre-Impact Orientation

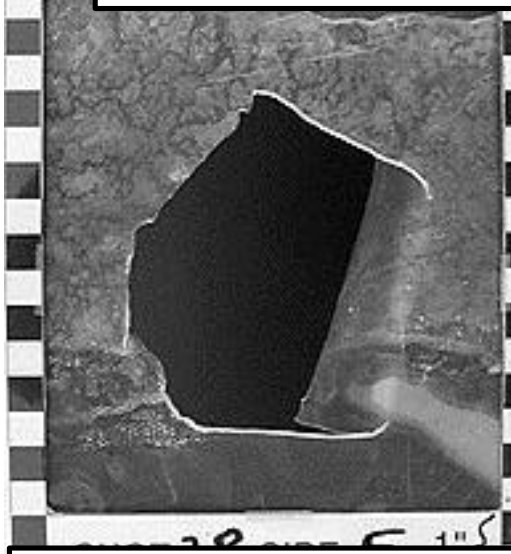

Figure C-77: Target Damage Frontal View

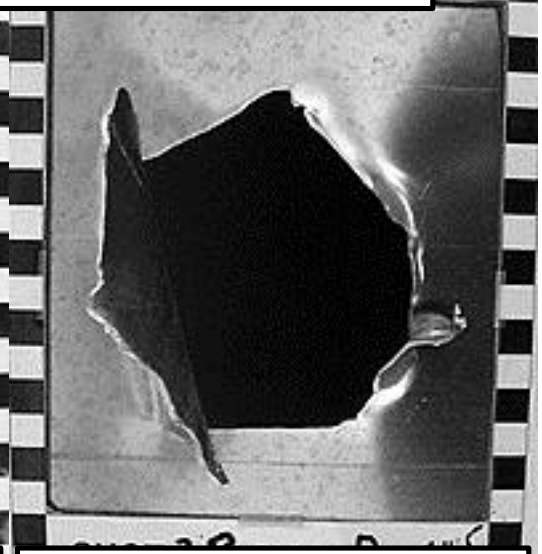

Figure C-78: Target Damage Rear View

Shot 78 (Series 4)

Target / Thickness
2024 T3 Aluminum / 0.071 (in.)

Fan Blade
Material / Weight
Titanium / 158.3 (grams)

Length / Width / Thickness
5.0 / 3.0 / 0.15 (in.)

Pitch / Yaw / Roll
-40 / -50 / -44 (degrees)

Presented Area
1.68 sq. in

Velocity Comparison
Impact / Residual / Predicted / Accuracy
309 fps / 183 fps / 264 fps / 1.26

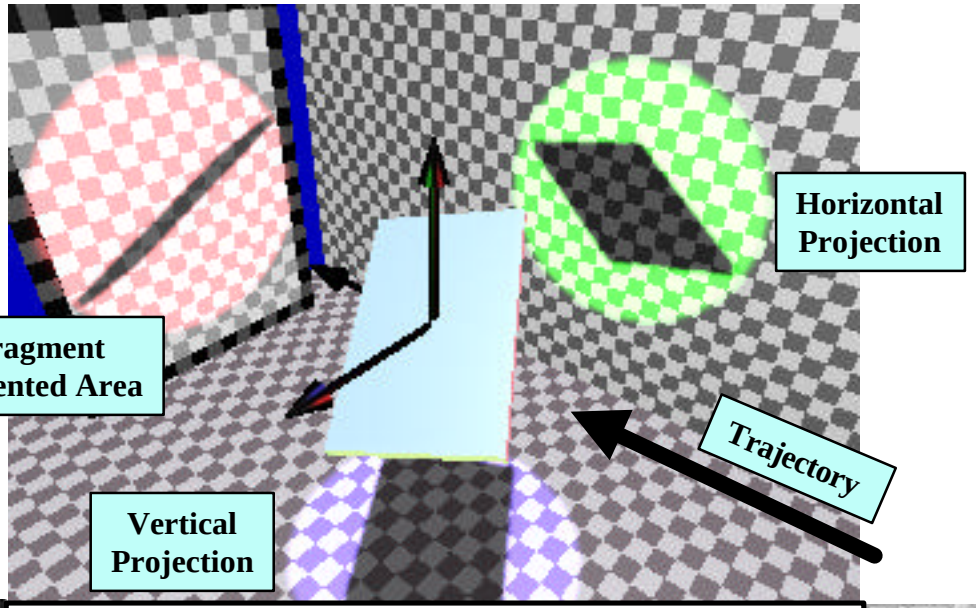

Figure C-79: Shot 78 Pre-Impact Orientation

Figure C-80: Target Damage Frontal View

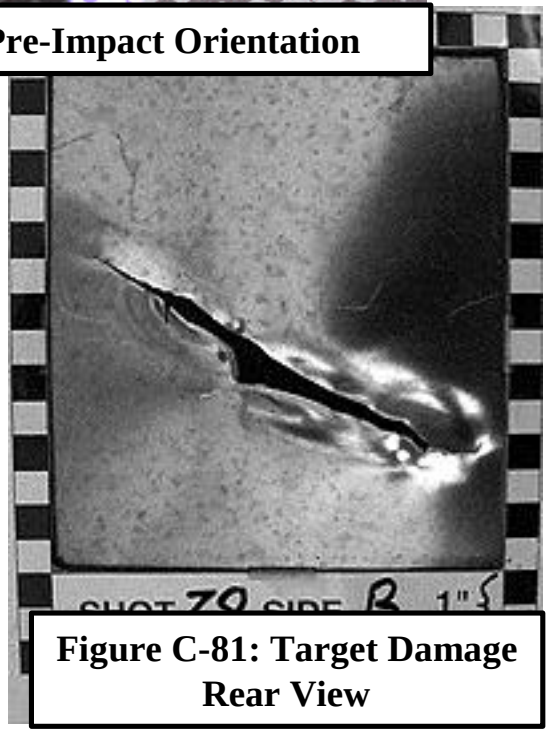

Figure C-81: Target Damage Rear View

FAA ENGINE DEBRIS PENETRATION TEST
REVISION 6

PREPARED BY:

_____
Joseph A. Manchor
Project Engineer
Code 418300D

CONCURRED BY:

_____
Jay Kovar
Head, Weapons Survivability Lab
Code 418300D

REVIEWED BY:

_____
Charles Frankenberger
Project Engineer
Code 418300D

CONCURRED BY:

_____
A. J. Wearner, Head, Systems
Engineering Branch
Code 418300D

CONCURRED BY:

_____
Albert Bermudez
WSL Firing Officer
Code 418300D

APPROVED BY:

_____
Richard (Tim) Horton
Head, Survivability Division
Code 418000

BACKGROUND **1**

OBJECTIVE **3**

APPROACH **3**

TEST OVERVIEW 3
TEST SEQUENCE 7

PRETEST PREDICTIONS **10**

PRE-TEST PREPARATION AND TEST SET-UP **12**

FABRICATION REQUIREMENTS 12
Target Plates and Support Stand *12*
Residual Velocity Break Paper Stands *13*
Projectile Fragments *13*
Sabots and Styrofoam Supports *17*
Sabot Catcher and Blast Exhauster *17*
Ordnance Requirements *17*
Target Setup *18*

DATA REQUIREMENTS **19**

INSTRUMENTATION 20

TEST CONSTRAINTS **20**

ENVIRONMENTAL 20
SAFETY AND SECURITY 21
LOGISTICAL 21

TEST PROCEDURE **21**

SCHEDULE AND DOCUMENTATION **24**

Background

As part of the ongoing Uncontained Engine Debris Mitigation Program, NAWCWPNS has developed a model to calculate uncontained engine debris exit velocities and residual energy levels. The Uncontained Debris Model (UDM) is based on the Joint Technical Coordinating Group for Munitions Effectiveness (JTCG/ME) penetration equations which have been derived from 50 caliber projectile testing. Engine debris characteristics are significantly different from the 50 cal. projectile in that the velocity range is lower, debris fragment size is larger, and the mass is heavier.

The UDM focuses on blade fragment debris as this type of debris is most likely to result from an uncontained engine event. According to extensive investigation, this is the most likely particle which would result in damage to aircraft. The debris model identifies the debris types by component (fan blade, turbine blade, ...) and defines the most likely size, mass and velocity for each debris fragment.

Debris fragment penetration orientation is defined for each impact. The fragment's impact orientation angle is defined as the angle between the fragment's surface area and the perpendicular of the fragment's direction of travel. Obliquity angle is defined as the angle between the fragment's direction of travel and the perpendicular of the impact target surface area. An illustration defining impact orientation and obliquity is given in figure 1. For further clarification, examples of various orientation and obliquity angle impacts are shown in figure 2.

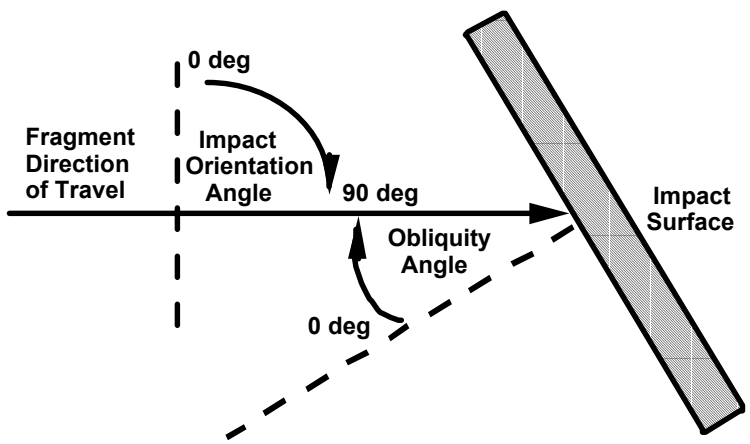

Figure 1: Impact Orientation and Obliquity Angles

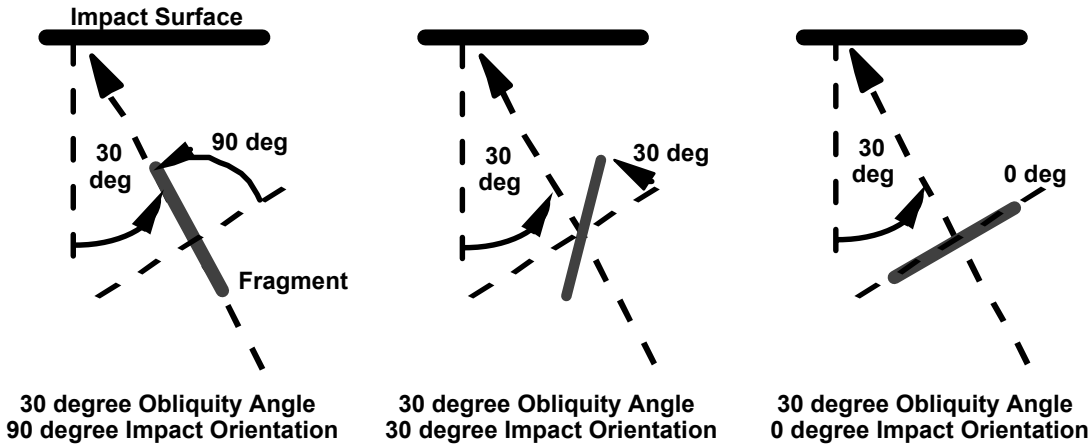

Figure 2: Examples of Obliquity and Impact Orientation

For initial impacts it is assumed (based on investigative data) that as the debris is penetrating case structure or inner cowl barrel walls, the impact angle is large (a 90 degree angle defines an end on penetration). Penetrations through additional structures are assumed to take place at a 45 degree impact orientation (this replicates the average impact orientation of a tumbling fragment).

The JTCG penetration equations utilized by the model are listed as follows:

1. $$V_r = \frac{\sqrt{V^2 - V_{50}^2}}{1.0 + \frac{\rho A_p t}{W \cos\theta}}$$

2. $$V_{50} = C_{bf}\left(\frac{\rho_f t A_p}{W}\right)^{b_f} \sec^h \theta \left(\frac{\rho_f t A_p}{W_o}\right)^f$$

Variables:

V = debris initial velocity

V_{50} = debris ballistic limit velocity. Penetration occurs 50% of the time.

V_r = debris residual velocity

ρ_f = debris specific weight (debris weight/volume)

ρ = plate specific weight (plate weight/volume)

t = plate thickness

A_p = debris presented area along direction of travel

θ = debris obliquity angle at impact

W = debris weight

W_o = 100 grains

Empirical Constants: C_{bf}, b_f, h, f

Of particular concern (and the reason for this test series) are the empirical constants utilized within equation 2. Published values for these constants may not be appropriate for use in the model. The projectiles which were utilized in the development of these constants may have characteristics which are dissimilar from engine blade fragments. As such, prediction inaccuracies may result from their use. This test series will verify the accuracy and appropriateness of these constants, and if necessary determine new values for these constants.

Objective

The test objective is to collect fragment penetration data to validate and/or refine the penetration equations used to develop the Uncontained Debris Model. Testing will be conducted using a fragment simulator and engine debris fragments against various thickness' of aluminum plates and possibly aircraft skin structures.

Approach

Test Overview

Fragment penetration data will be collected utilizing the setup displayed in figure 3. An airgun will be utilized to propel a sabot and fragment to the desired velocity. A sabot stopper will be affixed to the end of the gun barrel to strip the sabots away from the accelerated fragment. Blast deflectors will be placed in front of the gun muzzle, and beside the high speed cameras to reduce the potential of blast damage to the target and cameras.

Impact projectile velocity will be computed based on input from a breakwire affixed to the gun muzzle, and breakpaper affixed to the target impact point. Residual projectile velocity will be computed based on input from two breakpaper stands located at the rear of the target. Gridboards will be placed near the fragment-target impact point to allow additional velocity calculations to be made from high speed camera footage. A mirror will be placed above the target to assist determination of fragment orientation at impact.

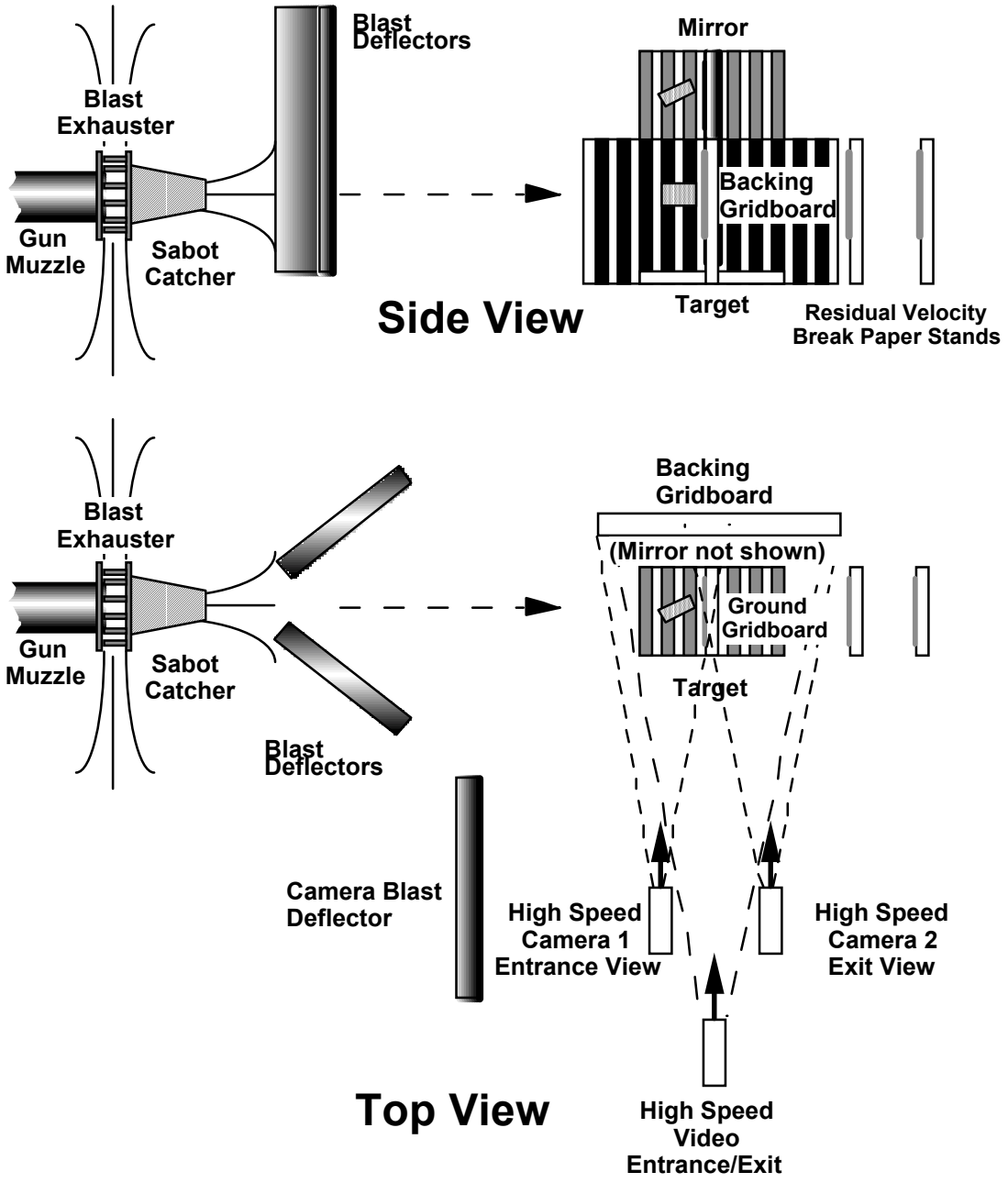

Figure 3: Test Setup

The airgun will propel the fragments utilizing a sabot as displayed in figure 4. The desired fragment orientation angle will be controlled through a combination of fragment tilt angles within the sabot (see figure 5), and the overall distance from the gun muzzle to the target.

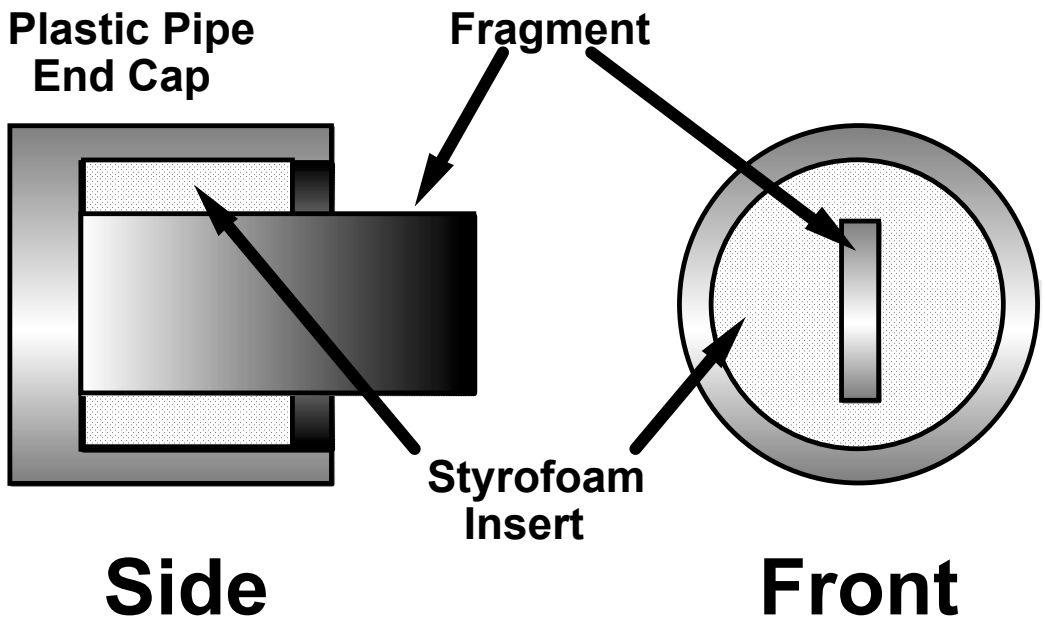

Figure 4: Saboted Fragment (90 deg. impact orientation)

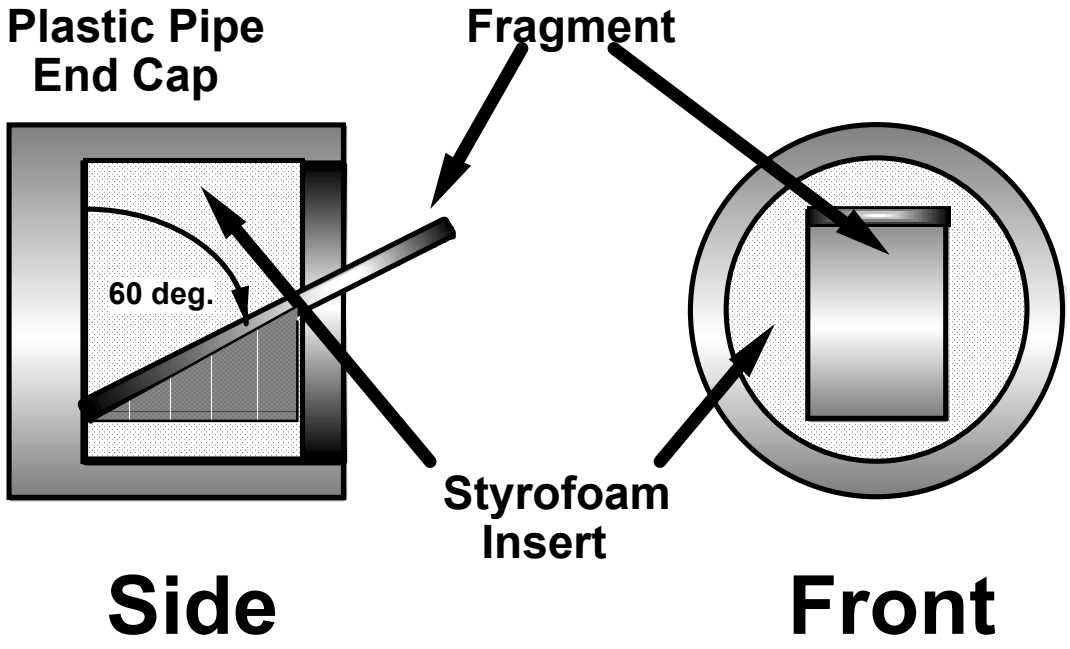

Figure 5: Sabot Impact Orientation Angle Control, (60 degrees shown)

The fragment will be released from the sabot through the use of a sabot catcher, as displayed in figure 6. The tapered reduction in internal diameter of the catcher enables minimized impulsive forces to be seen by the sabot. The intent is to reduce the possibility of breakup, and travel of sabot fragments to the target. However, the sabots are not reusable due to severe scoring damage from the catcher.

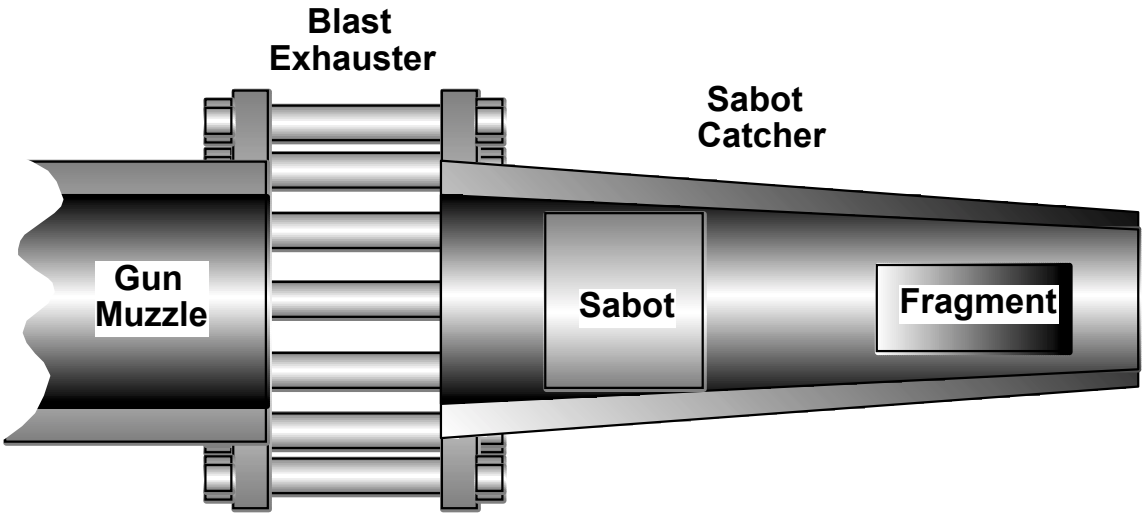

Figure 6: Sabot Catcher

The sabot catcher will be affixed a distance from the air gun muzzle by means of a blast exhauster. The lodging of the sabot within the catcher will reduce blast exhaust through the catcher exit (and thus blast seen by the target). The resulting pressure build up behind the sabot will be released through the exhauster. The exhauster will allow much of the blast to dissipate perpendicular to the muzzle, thus minimizing blast at the target.

Test Sequence

The test will be composed of eight separate test series as outlined in Table 1. A more detailed test matrix is outlined in the Test Procedure section of this test plan as Table 4.

Table 1: Test Sequence

Test Series	Fragment (Impact Orientation)	Approximate Fragment Weight	Target	Number of Tests
1	Sabot Checkout	0.25 lb.	0.05" Al	3
2	Simulated Frag. (90)	0.055 lb.	0.05" Al	8
3	Fan Blade (90)	0.4 lb.	0.05" Al	8
4	Fan Blade (90)	0.4 lb.	0.07" Al	8
5	Compressor Blade (45)	0.25 lb.	0.05" Al	8
6	Turbine Blade (60)	0.25 lb.	0.05" Al	8
7	Turbine Blade (30)	0.25 lb.	0.05" Al	8
8	Fan Blade (90)	0.4 lb.	Engine Cowl	6

Test series #1 will verify the effectiveness of the sabots in achieving both end on and tumbled impacts at the target. Proper operation of all test systems will also be verified during these tests. Additionally, the accuracy of fragment velocity calculations will be compared based upon break wire-break paper computation and high speed camera visual calculations.

Test Series #2 will fire simulated blade fragments similar to those utilized during the SRI International Advanced Armor Technology impact experiments. These experiments were conducted in the summer of 1997 at the SRI International gas gun facility. The SRI experiments evaluated the impact resistance of current fuselage wall materials (including 2024-T3 Aluminum), along with several advanced candidate wall materials. Test Series #2 will provide baseline impact resistance data for 2024-T3 Aluminum. This baseline data (along with the Uncontained Debris Model predictions) will be compared with the accumulated data from the SRI experiments.

Test series # 3 through 7 will examine actual engine blade fragment impacts at various impact orientation and obliquity angles. Characteristics of these fragments (dimensions, material, weight, and impact velocity/orientation) will be those which are most likely to be experienced during an engine burst.

Test series # 8 is currently planned as the final test series, and will examine the reaction of engine blade impacts against an actual engine cowling. Comparison will be made with the data accumulated from the previously conducted test series. The intent is to determine consistency of the data between the use of new sheet metal targets, and actual engine cowling material. Depending on cost, range and material availability, an

additional test series may be included which will examine fragment impacts against Kevlar target plates. Details on the Kevlar plate test series will be supplied by SRI International.

Fragment impact velocities utilized in each test series will be based on the predicted fragment V_{50} values for the test conditions. Due to the uncertainty of the actual V_{50} value for each test condition, impact velocities near the predicted V_{50} value may result in non-penetration of the target (and thus loss of desired residual velocity data). As such, the initial test velocity utilized in each series will be the fragment's predicted V_{50} velocity plus 500 ft/sec. Follow on test impact velocities will incrementally decrease from this initial value by V_{50} plus 300, 100, 75, 50, 25, and 15 ft/sec. The final test series impact velocity will be the predicted value of V_{50}.

It should be noted that there are not enough shots available in each test series to determine a precise value of V_{50} for each test condition. Should non-penetration of the target occur prior to reaching the predicted value of V_{50}, that impact velocity which resulted in non-penetration will be assumed as an approximate value for V_{50}. Those remaining shots in the test series will be incremented from this approximate value.

Test series # 2, 3, and 4 will examine a 90 ^{o} (edge on) fragment impact orientation. The predicted V_{50} value for this type of condition can be quite low (< 200 ft/sec) due to the small fragment presented area (assuming each fragment is roughly a flat plate). Very low impact velocities (< 200 ft/sec) may prove difficult to accurately regulate with the airgun. These velocities will be attempted, but the actual impact velocity may vary from those utilized in the pre-test predictions.

Many of the tests will utilize fragments cut from actual engine blades. As shown in figure 7, these fragments may have a slight aerodynamic twist in their dimensions. As compared to a flat plate, a twist will result in an increased actual edge-on presented area, and thus increased V_{50} values for edge-on impacts. The fragment's actual edge-on presented area will be determined after fragment fabrication (and prior to testing) to allow refinement of the pre-test predictions.

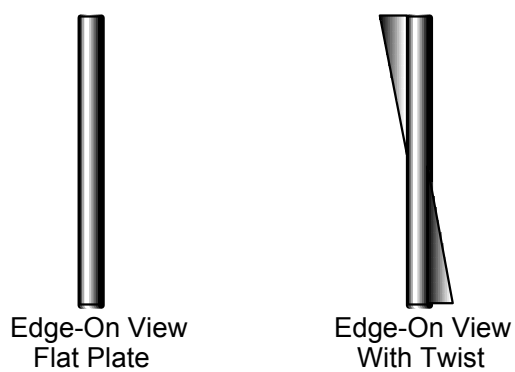

Figure 7: Example of Fragment Edge-On Views

For impact velocities which result in penetration of the target, the fragment's residual velocity will be measured. Data will be collected by computing the fragment's impact velocity via a breakwire in the gun barrel and break paper on the target. High speed film will be used to verify the impact velocity and calculate the residual velocity. High speed film will also be used to determine the fragment's impact orientation. A sample chart illustrating the type of data to be expected from this test series is illustrated in figure 8.

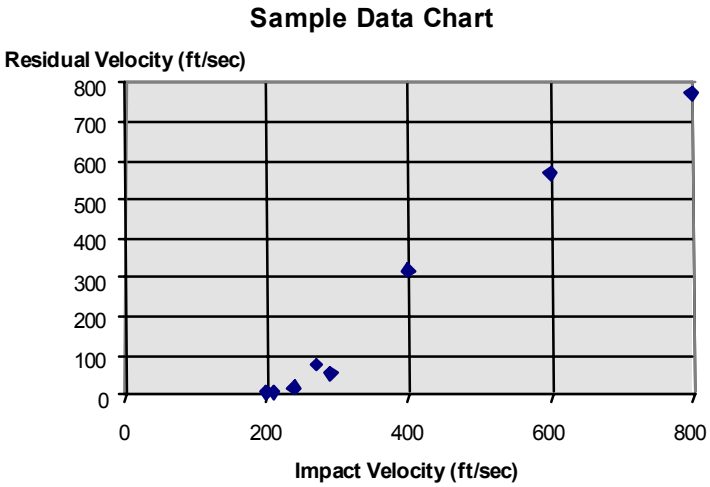

Figure 8: Sample Velocity Data Chart

Pretest Predictions

The JTCG/ME penetration equations prediction model was utilized to calculate predicted residual velocities for each test series. V_{50} values were predicted based on each test series parameters. Predicted residual velocities were then tabulated based on impact velocity increments of V_{50} + 15, 25, 50, 75, 100, 300, and 500 ft/sec. A prediction plot of each test series residual velocities is illustrated in figure 9.

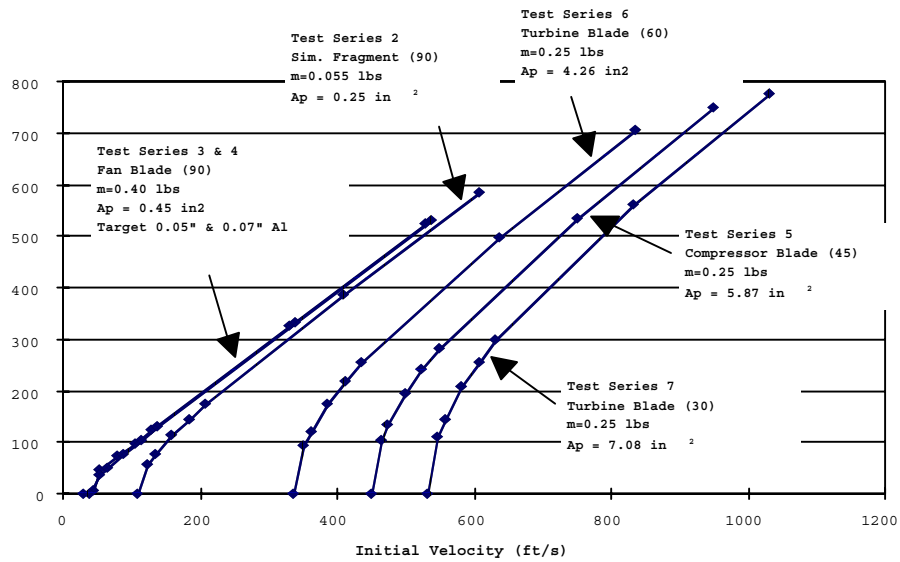

Figure 9: Pre-Test Predictions, Initial Impact vs. Residual Velocity

The fragment's mass was then utilized in conjunction with impact and residual velocities to calculate impact Kinetic Energy versus Residual Kinetic Energy. Figure 10 displays this comparison.

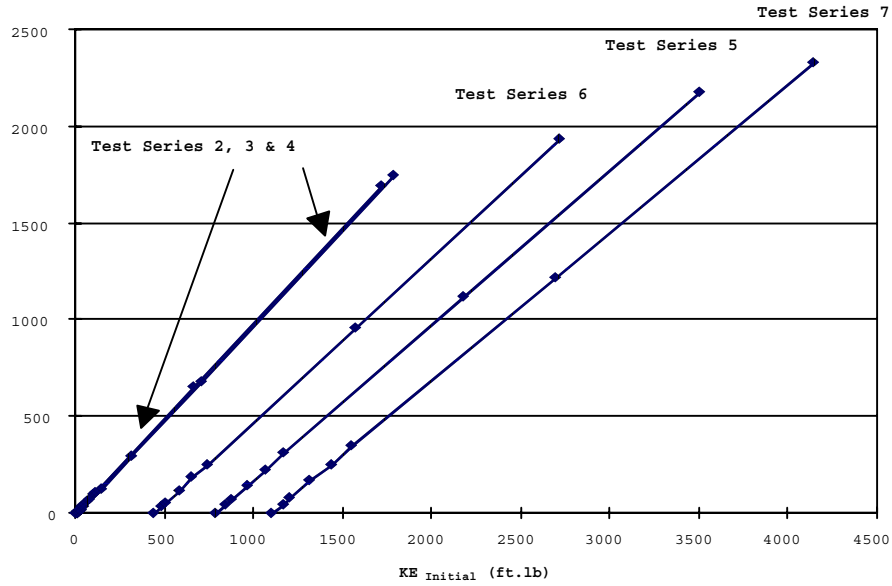

Figure 10: Pre-Test Prediction, Initial vs. Residual Kinetic Energy

An alternative comparison was made of the ratio of the fragment's predicted residual kinetic energy to impact kinetic energy. This comparison was plotted against impact velocity, and is displayed in figure 11.

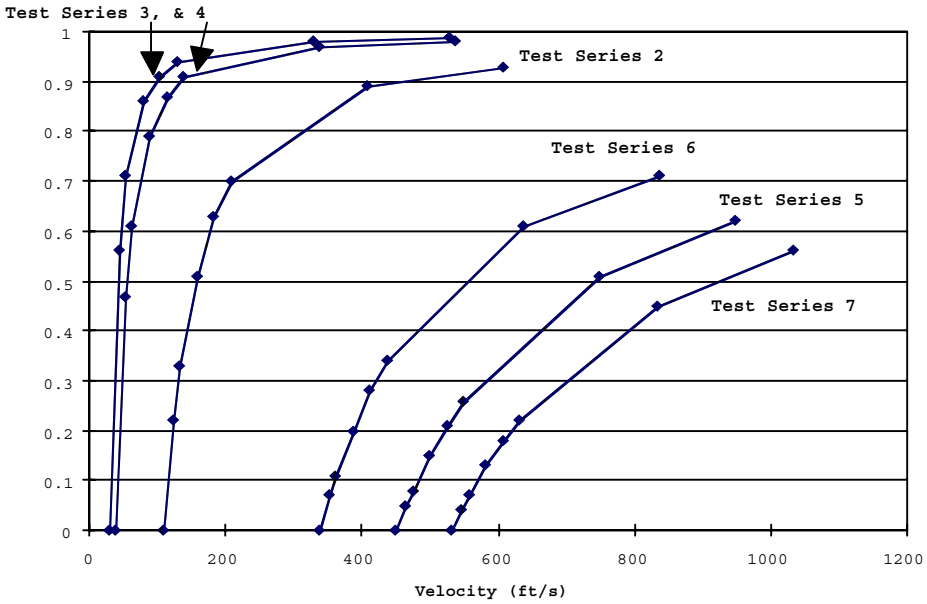

Figure 11: Pre-Test Prediction, Impact Velocity vs. Kinetic Energy Ratio

Pre-Test Preparation and Test Set-Up

Fabrication Requirements

Target Plates and Support Stand

Approximately forty three 0.05”, and eight 0.07” thick aluminum (2024-T3) target plates will be required for the test series. The plates should be cut as 2 foot square panels, and should include drilled holes for connection to the test stand (see figure 12).

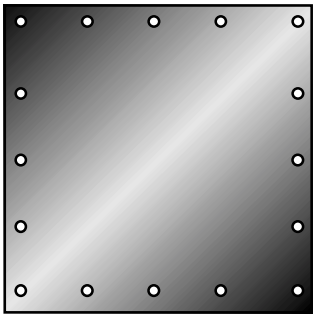

Figure 12: 2 × 2 ft. Target Plate

For test series # 8, the required eight target plates will be constructed of actual engine cowling material from WSL aircraft. An additional test series (# 9) may be added which would require the preparation of Kevlar targets utilizing Kevlar material provided by the WSL. Test preparation details of the Kevlar targets will be supplied by SRI.

A target support test stand will be constructed of angle iron as displayed in figure 13. The stand will include drilled holes for bolting the target plate to the stand. Four steel support strips with matching drilled holes will also be fabricated to provide rigid attachment of the plates to the test stand.

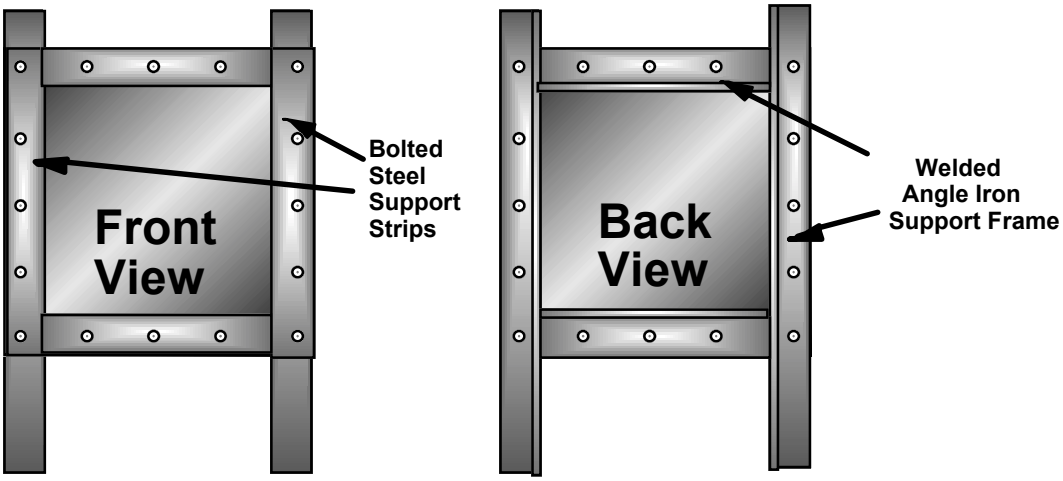

Figure 13: Plate Support Stand

Residual Velocity Break Paper Stands

Two residual velocity break paper support stands will be required for the test series. Fabrication will be similar to that displayed in figure 14.

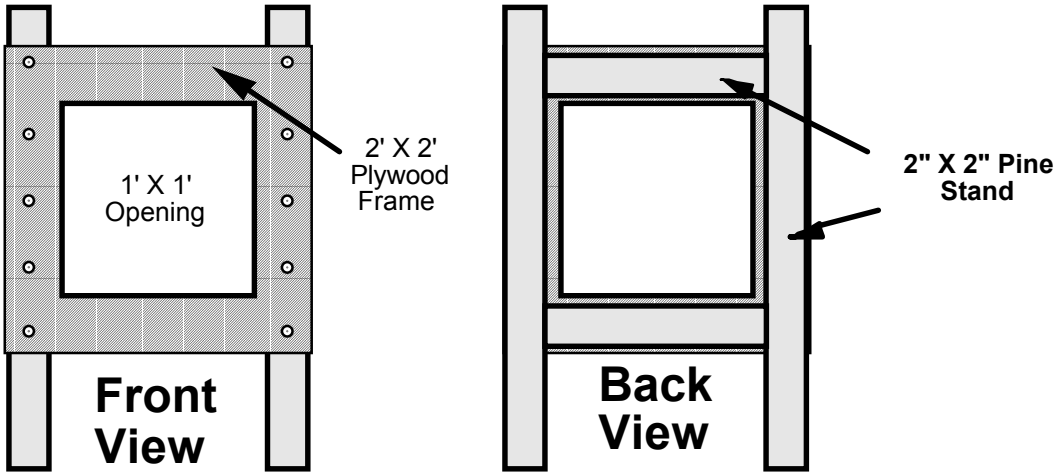

Figure 14: Residual Velocity Break Paper Stands

Projectile Fragments

Test series #2 will require the fabrication of 8 simulated fan blade projectiles. They will be fabricated from titanium plate. Fragment dimensions will be 1 3/8" x 1" x 1/4". Each fragment will weigh approximately 0.055 lbs.

Test series # 3, 4, and 8 will utilize actual engine fan blade fragments. They will be cut to dimensions of 5 1/2" length and 3" width. Each fragment will weigh approximately 0.4 lbs. A total of 22 fan blade fragments will be required.

Test series # 5 will require the cutting and preparation of eight compressor blade fragments. Desired length and width of the fragments are 4" x 2". Each fragment will weigh approximately 0.25 lbs.

Test series 6 & 7 will require preparation of 16 turbine blade fragments, cut to dimensions of 4" x 2". Each fragment will weigh approximately 0.25 lbs.

A summary of the required fragment projectiles is listed in Table 2. Figure 15 illustrates how the fragments will be cut from available engine fan, compressor, and turbine blades. Drawings of the represented fragments are displayed in Figures 16, 17, and 18.

Table 2: Projectile Requirements

Material	Dimensions L x W x thickness	Weight	# Fragments Required
Titanium	1.4” x 1” x 0.25”	0.055 lb.	8
Fan Blades	3” x 5.5” x blade thickness	0.4 lb.	22
Compressor Blades	4” x 2” x blade thickness	0.25 lb.	8
Turbine Blades	4” x 2” x blade thickness	0.25 lb.	16

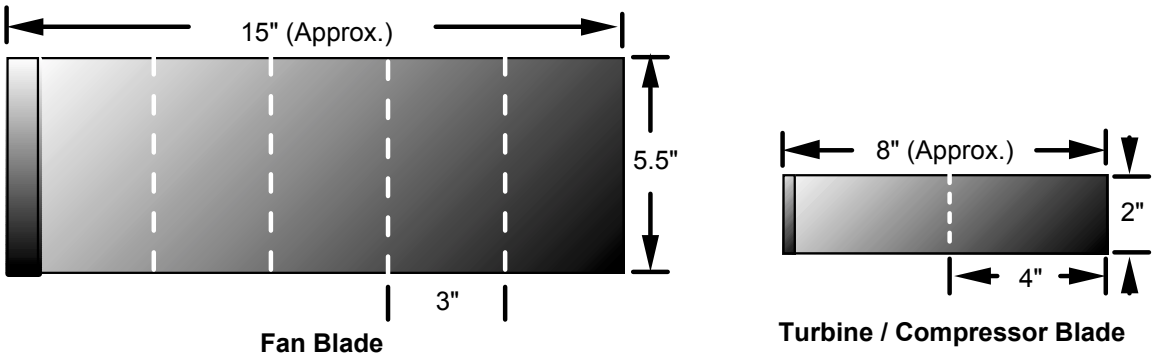

Figure 15: Fragment Preparation

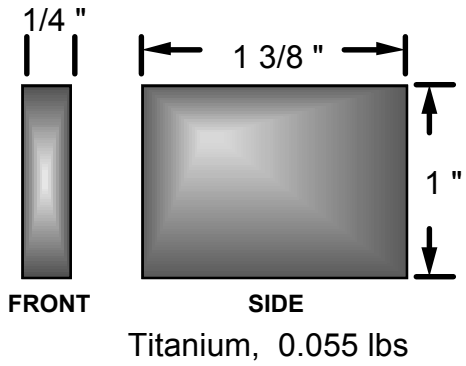

Figure 16: Test Series 2, Simulated Fragment

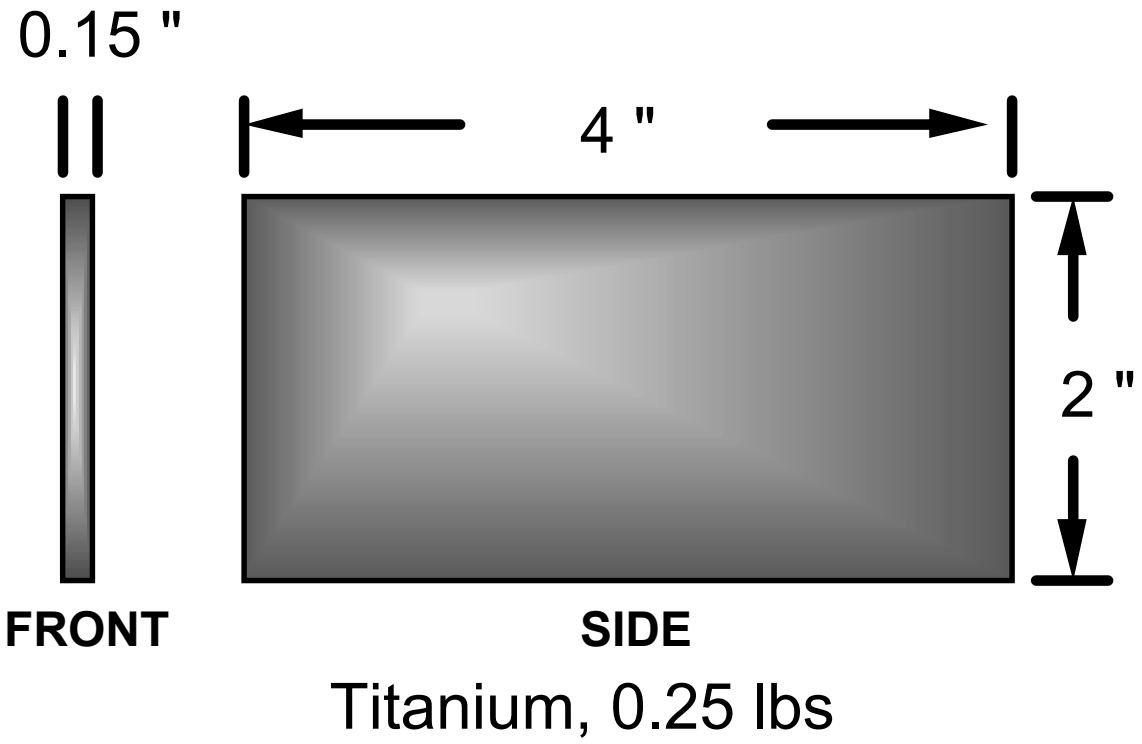

Figure 17: Test Series 5, 6, & 7, Compressor / Turbine Blade Fragment

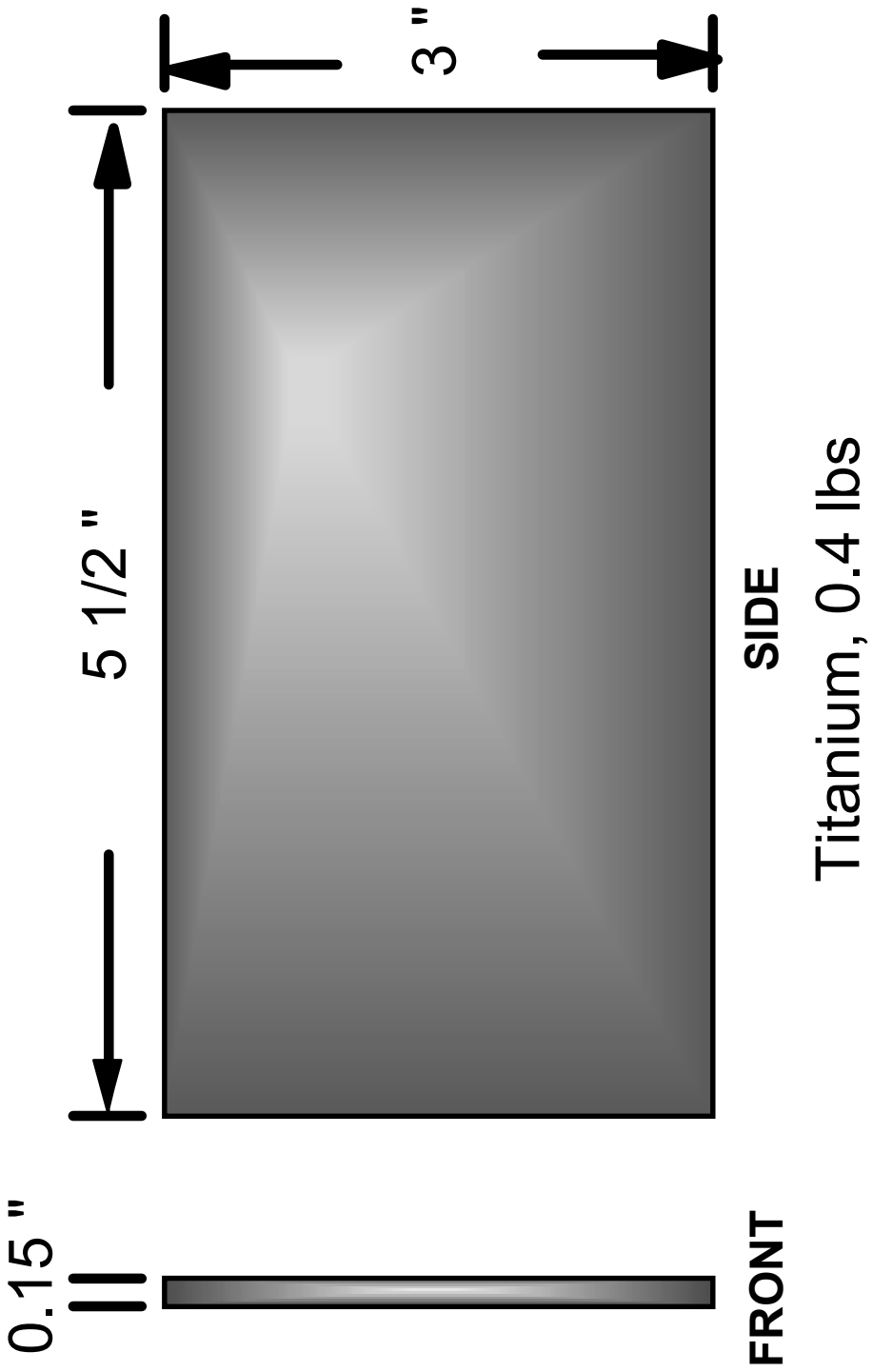

Figure 18: Test Series 3, 4, & 8, Fan Blade Fragment

Sabots and Styrofoam Supports

Each of the test series will require sabots to propel the fragment projectiles. Their diameter and length should be sufficient to provide a snug fit within the airgun barrel, while providing support to the projectile fragment. The sabots will be fabricated from plastic tubing endcaps. A total of seventy sabot's will be required for this testing.

Styrofoam insert supports will be fabricated and installed within each sabot as previously shown in figures 4 and 5. Requirements for these supports are listed in Table 3.

Table 3: Sabot Styrofoam Support Requirements

Test Series	Fragment Width x Length	Support Angle	# Supports Required
1	2" x 4"	45 ^{o}	3
2	1 " x 1 3/8 "	90 ^{o} (end on)	8
3	3 " x 5 1/2 "	90 ^{o} (end on)	8
4	3 " x 5 1/2 "	90 ^{o} (end on)	8
5	2 " x 4 "	45 ^{o}	8
6	2 " x 4 "	60 ^{o}	8
7	2 " x 4 "	30 ^{o}	8
8	2 " x 4 "	90 ^{o} (end on)	8

Sabot Catcher and Blast Exhauster

A sabot catcher / blast exhauster (see figure 6) will be fabricated and installed to the airgun. The catcher should enable easy removal of the sabot for reuse. Design and materials utilized in this fabrication will be at the discretion of the WSL Engineer.

Ordnance Requirements

Due to the relatively large projectile size, testing will require utilization of the Missile Impact Kinetic Energy Simulator (MIKES) air gun. A high pressure nitrogen gas source will also be required capable of propelling one pound blade fragments through the MIKES at velocities up to 1000 fps.

Placement of the gun in front of the target will be such that range from the gun muzzle to the target should be within 10 feet. The gun's shotline will be perpendicular to the target plate's face to achieve an obliquity angle of zero degrees.

Target Setup

Details of the target Setup are displayed in figure 19. Striped gridboards will be placed in the background, and below the target. This will allow calculation of the fragment's pre and post impact velocities through examination of high speed camera footage. As additional sources of velocity data, a break wire will be installed at the gun muzzle, along with break papers affixed at the desired impact point and at two stations rear of the target plate. A mirror will be placed at a 45 degree angle above the target to enable determination of the fragment's orientation at impact.

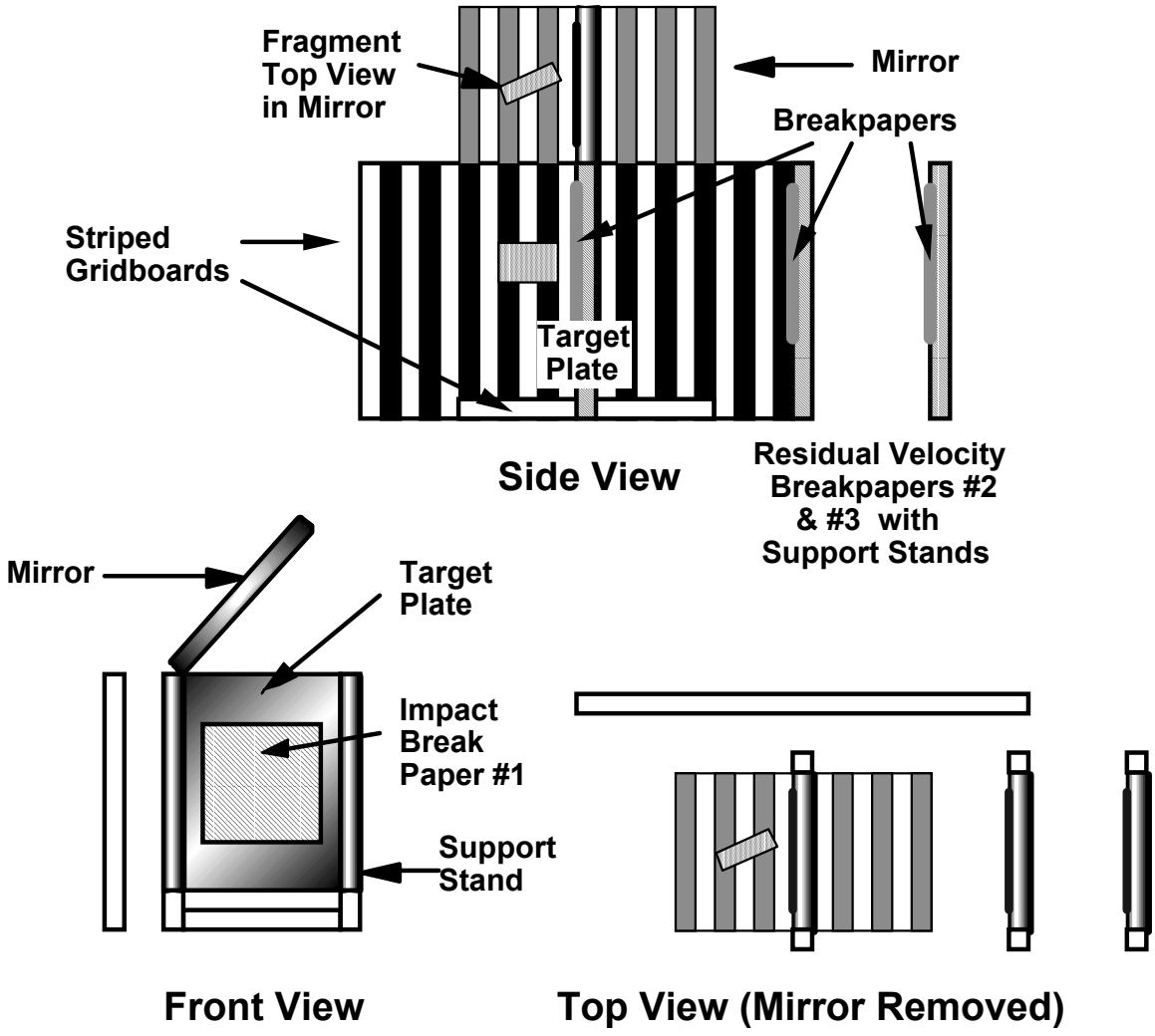

Figure 19: Target Setup

Data Requirements

Primary data required for these tests are the fragment's target impact and residual velocities, along with fragment orientation at impact. The velocity data will be computed through the use of breakwires and breakpaper. As secondary backup, these velocities will also be calculated based on fragment position/time data from the high speed camera footage. The impact orientation of the fragment will be determined by high speed photographic record of the impact in two planes (mirrored top view and direct side view).

As a cost saving effort, initial tests will utilize one high speed film and one high speed video camera. The desired field of view for both cameras (film and video) is shown in figure 20 (a). If the photographic resolution proves unsatisfactory, a second high-speed film camera will be utilized with field of views as shown in figure 20 (b). Desired high-speed camera frame rates will be 2,000 frames/sec for all tests. The intent is to minimize any confusion or error which may be incurred by changing frame rates between the seventy-five planned shots. This setting should also provide the desired minimum of 4 frames of fragment travel at the highest fragment velocities.

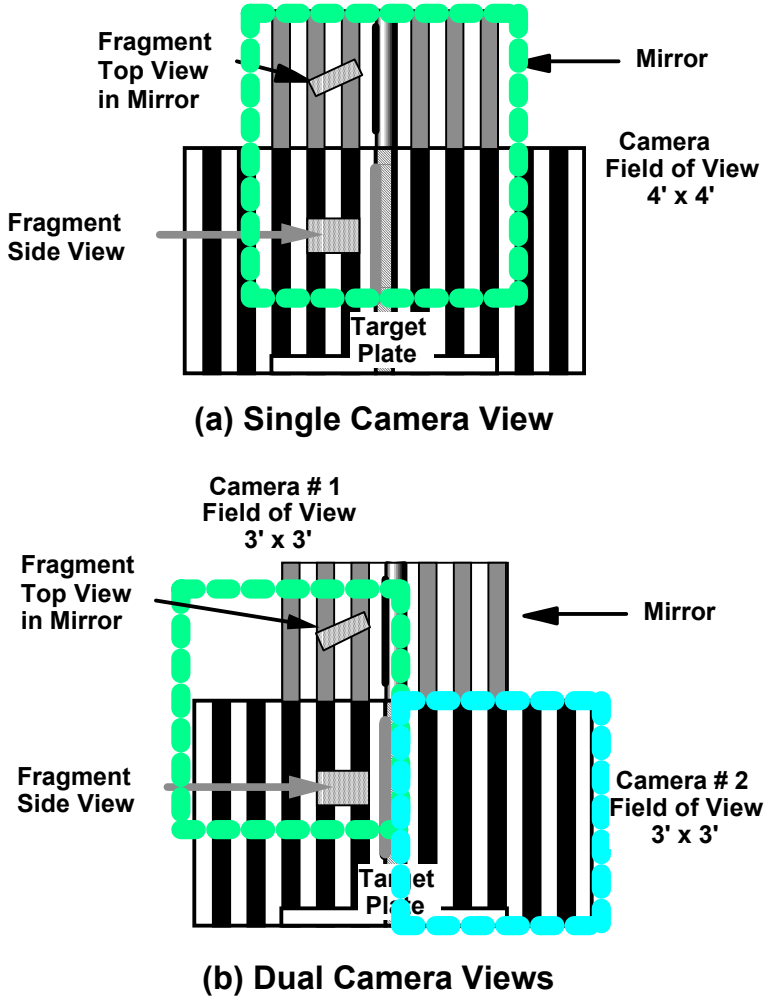

Figure 20: Desired High-Speed Camera Views

Instrumentation

Instrumentation requirements are described as follows:

- Breakwire at gun muzzle
- Breakpaper at target plate surface
- Breakpaper at residual velocity support stand #1
- Breakpaper at residual velocity support stand #2
- High speed camera #1
- High speed camera #2 (if required)
- High speed video
- Range safety video
- Air gun controlling and monitor

Test Constraints

Environmental

All testing will be accomplished when adequate light is present for the high speed cameras. The testing will be stopped if:

- There is wind over 25 knots.
- There is rain or snow in the test area.

Safety and Security

Safety equipment must be operational during the test: This includes data recorders and range safety video cameras. Personnel should wear coveralls on the test pad.

Tests will be conducted following standard operating procedures prepared by the WSL and approved by the NAWC Safety Office. At no time during the tests will project requirements overrule the safety of personnel or present hazards to the facility. Any situation which the firing officer or project engineer feels threatens the safety of personnel, facility, or test items will be cause for a delay in testing. The Weapons Survivability Laboratory (WSL), Naval Air Warfare Center (NAWCWPNS), will consolidate the technical requirements of the test plan into a NAWCWPNS-approved operating procedure. This procedure will be used for all test runs in the test program.

Logistical

Failure of critical test or safety equipment will stop the test until repair is done.

Test Procedure

The detailed test matrix is listed in Table 4. The test logic sequence is illustrated in figure 21. The following is a sequential outline of the test procedures:

1. Install/repair the target plate.
2. Install new break papers and break wires.
3. Realign/sight air gun muzzle to hit target while achieving desired impact orientation.
4. Sight high speed cameras and video. Verify sufficient lighting for coverage.
5. Load air gun barrel with sabot and projectile.
6. Prepare air gun for firing.
7. Commence data recording
8. Fire the projectile.
9. Stop data recording

Table 4: Test Series Matrix

	Series 1	Series 2	Series 3	Series 4	Series 5	Series 6	Series 7	Series 8	Series 9
Target	0.05" Alum.	0.05" Alum.	0.05" Alum.	0.07" Alum.	0.05" Alum.	0.05" Alum.	0.05" Alum.	Cowling	Kevlar
Fragment	2"x 4" Comp.	1"x 1.4" Sim.	3"x 5.5" Fan	3"x 5.5" Fan	2"x 4" Comp.	2"x 4" Turb.	2"x 4" Comp.	TBD	TBD
Mass	0.25 lb.	0.055 lb.	0.40 lb.	0.40 lb.	0.25 lb.	0.25 lb.	0.25 lb.	TBD	TBD
Obliquity	0 ^{o}	0 ^{o}	0 ^{o}	0 ^{o}	0 ^{o}	0 ^{o}	0 ^{o}	0 ^{o}	0 ^{o}
Impact Orient	45 ^{o}	90 ^{o}	90 ^{o}	90 ^{o}	45 ^{o}	60 ^{o}	30 ^{o}	TBD	TBD
Shot 1 V_{50} +500 (ft/s)	949	608	529	538	949	836	1032	TBD	TBD
Shot 2 V_{50} +300 (ft/s)	549	408	329	338	749	636	832	TBD	TBD
Shot 3 V_{50} +100 (ft/s)	29	208	129*	138*	549	436	632	TBD	TBD
Shot 4 V_{50} + 75 (ft/s)	----	183*	104*	113*	524	411	607	TBD	TBD
Shot 5 V_{50} + 50 (ft/s)	----	158*	79*	88*	499	386	582	TBD	TBD
Shot 6 V_{50} + 25 (ft/s)		133*	54*	63*	474	361	557	TBD	TBD
Shot 7 V_{50} + 15 (ft/s)		123*	44*	53*	464	351	547	TBD	TBD
Shot 8 V_{50} (ft/s)		108*	29*	38*	449	336	532	TBD	TBD

* Very low velocities (< 200 ft/sec) may prove difficult to regulate with the MIKES gun. These velocities will be attempted, but the actual impact velocity may vary from those noted in this chart.

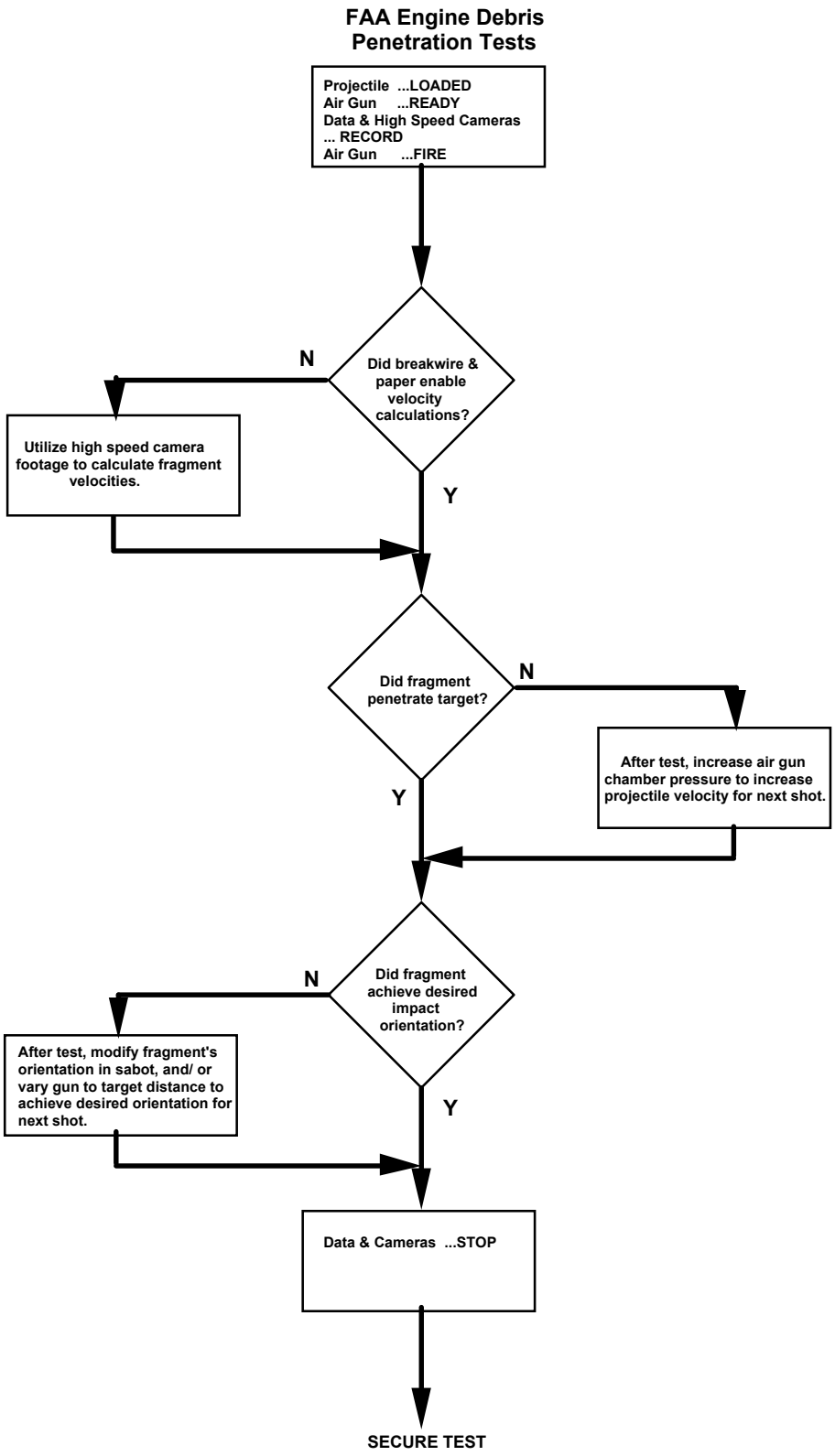

Figure 21: Test Logic Sequence

Schedule and Documentation

The test is scheduled for January 1998 at the Weapons Survivability Laboratory. A test report will be prepared which will include the test objectives, approach, test set-up, and results. The report will be submitted for review within two months after test completion.